Die approbierte Originalversion dieser Dissertation ist in der Hauptbibliothek der Technischen Universität Wien aufgestellt und zugänglich.
http://www.ub.tuwien.ac.at

The approved original version of this thesis is available at the main library of the Vienna University of Technology.
http://www.ub.tuwien.ac.at/eng

DISSERTATION

Metastable Iron-Nickel Thin Films

Ausgeführt zum Zwecke der Erlangung des akademischen Grades eines Doktors der technischen Wissenschaften unter der Leitung von

Ao.Univ.Prof. Dr.techn. Michael Schmid
Institut für Angewandte Physik E134

und

Ao.Univ.Prof. Dr.techn. Peter Varga
(† 27.10.2018)

eingereicht an der Technischen Universität Wien

Fakultät für Physik

von

Ing. Jonas Gloss
e1229106
Schenkenstraße 2
1010 Wien

Wien, April 2019

Abstract

Magnetic nanostructures are used both in applications for patterned media and sensors as well as for fundamental research in, for example, magnonics. Fabrication of magnetic nanostructures by a focused ion beam (FIB) presents an alternative to the commonly used lithography. Metastable films are a promising system for FIB-induced patterning in the micrometer and sub-micrometer scale for the use in, e.g., magnon crystals and waveguides.

An example of the metastable films are the iron-nickel thin films because they can grow epitaxially in the face-centered-cubic (fcc) structure and are paramagnetic (PM). The metastable films undergo a structural (fcc → body-centered-cubic) and magnetic (PM → ferromagnetic) transformation upon ion-beam irradiation. The growth of the metastable $Fe_{78}Ni_{22}$ films has already been shown on Cu(100) single crystals. We show in this work that the ion-beam-induced transformation makes it possible to tune not only the magnetic saturation, but also the anisotropy of the $Fe_{78}Ni_{22}$/Cu(100) with the focused ion beam (FIB).

The applications call for a cheaper substrate and fundamental research would benefit from growing the metastable films on an insulating or a transparent substrate. There are multiple alternative substrates that have suitable properties to support the epitaxial growth of the metastable films, of which we chose three: Si(100), C(100), and $SrTiO_3$(100).

Si(100) is a material commonly used in the electronics industry, and therefore its preparation is well known. To avoid a significant lattice mismatch between Si(100) and $Fe_{78}Ni_{22}$, it is possible to grow a Cu(100) epitaxial buffer layer on a hydrogen-terminated Si(100) [H-Si(100)] surface. H-Si(100) can be prepared not only by the conventional HF etching but also in Ultrahigh vacuum (UHV) by flashing (brief heating to 1200 °C) and a consequent hydrogen termination. For this purpose a source for atomic hydrogen and a heating stage for the Si-flashing were built, which facilitated the UHV method of H-Si preparation. The growth and transformation of metastable thin films of $Fe_{78}Ni_{22}$/Cu/Si(100) are presented.

C(100) is non-conductive, transparent and it has a similar lattice mismatch to $Fe_{78}Ni_{22}$ as Cu(100), and the growth of epitaxial fcc Fe films with an average thickness of 4 monolayers has already been shown on it. We show that it is possible to clean

the C(100) in UHV after deposition of the metastable films by sputtering and etching in atomic hydrogen and that it is possible to grow and transform the metastable films on C(100). These films are not continuous, however, but consist of separate islands.

Auger electron spectroscopy and low-energy electron diffraction characterized the composition and structure of the substrates and of the as-deposited $Fe_{78}Ni_{22}$ films on Cu(100), Cu/Si(100) and C(100). The $Fe_{78}Ni_{22}$ films on C(100) were also investigated by scanning tunnelling microscopy. We investigated the properties of the $Fe_{78}Ni_{22}$ films by magneto-optical Kerr effect both prior and after the ion-beam irradiation and we show the dependence of the magnetization on the ion dose.

Similarly to H-Si, the growth of a continuous Cu(100) buffer layer by pulsed laser deposition has already been reported on the $SrTiO_3$(100), which is a prototype perovskite oxide with a cubic lattice at room temperature. It was not possible, however, to obtain a Cu(100) buffer layer on which the metastable $Fe_{78}Ni_{22}$ films would grow.

The possibility to use a standard substrate such as the Si(100) is an essential step towards applications in rapid prototyping of magnetic metamaterials (by using FIB) and in suitability for mass production (e.g., by ion irradiation through a mask). The growth of the metastable films on diamond enables the use of new techniques (e.g. magnetic transmission x-ray microscopy) for the characterization of the magnetic nanostructures.

Kurzfassung

Magnetische Nanostrukturen werden sowohl in Anwendungen für strukturierte Speichermedien und Sensoren als auch für die Grundlagenforschung eingesetzt, beispielsweise in der Magnonik. Die Herstellung magnetischer Nanostrukturen durch einen fokussierten Ionenstrahl (FIB) stellt eine Alternative zur üblicherweise verwendeten Lithographie dar. Metastabile Schichten sind ein vielversprechendes System für die FIB-induzierte Strukturierung im Mikrometer- und Submikrometerbereich zur Verwendung in, e.g., Magnonenkristallen und Wellenleitern.

Ein Beispiel für die metastabilen Schichten sind dünne Filme aus Eisen und Nickel, da sie in der kubisch-flächenzentrierten Struktur (fcc) epitaktisch wachsen können und paramagnetisch (PM) sind. Die metastabilen Filme durchlaufen bei Ionenbestrahlung eine strukturelle (fcc → kubisch-raumzentriert) und magnetische (PM → ferromagnetisch) Transformation. Das Wachstum der metastabilen $Fe_{78}Ni_{22}$-Filme wurde bereits auf Cu(100)-Einkristallen gezeigt. In dieser Arbeit wird gezeigt, dass es möglich ist, mithilfe eines fokussierten Ionenstrahls nicht nur die magnetische Sättigung sondern auch die Anisotropie der $Fe_{78}Ni_{22}$/Cu(100) Schichten zu bestimmen.

Die industrielle Anwendung erfordert ein kostengünstigeres Substrat im Vergleich zu den Cu(100)-Einkristallen und die Grundlagenforschung würde von metastabilen Schichten auf einem isolierenden oder einem transparenten Substrat profitieren. Es gibt mehrere alternative Substrate mit geeigneten Eigenschaften, die das epitaktische Wachstum der metastabilen Filme unterstützen. Wir haben folgende drei Substrate ausgewählt: Si(100), C(100) und $SrTiO_3$(100).

Si(100) wird üblicherweise in der Elektronikindustrie verwendet, und daher ist die Präparation dieser Oberfläche gut bekannt. Um die Gitterfehlanpassung zwischen Si(100) und $Fe_{78}Ni_{22}$ zu vermeiden, ist es möglich, eine Cu(100)-Epitaxieschicht auf einer Wasserstoff-terminierten Si(100) [H-Si(100)] Oberfläche aufzuwachsen. H-Si(100) kann nicht nur durch konventionelles HF-Ätzen hergestellt werden, sondern auch in Ultrahochvakuum (UHV) durch kurzes Heizen auf 1200 °C und darauf folgende Bedeckung mit Wasserstoff. Zu diesem Zweck wurden eine Quelle für atomaren Wasserstoff und eine Heizstation für Si gebaut. Dadurch wurde die Präparation der H-Si Oberfläche in UHV ermöglicht. Das Wachstum und die Umwandlung von metastabi-

len dünnen Filmen aus $Fe_{78}Ni_{22}$/Cu/Si(100) werden beschrieben.

C(100) ist nicht leitend, es ist transparent und hat nahezu die selbe Gitterkonstante wie fcc $Fe_{78}Ni_{22}$(100). Das Wachstum von epitaktischen fcc-Fe-Filmen mit einer durchschnittlichen Dicke von 4 Monolagen auf C(100) wurde bereits beschrieben. Diese Arbeit beschriebt das Wachstum dicker fcc $Fe_{78}Ni_{22}$(100)-Schichten auf C(100) und ihre Umwandlung zu ferromagnetischen bcc-Strukturen durch Ionenbeschuss. Diese Filme sind jedoch nicht kontinuierlich, sondern bestehen aus separaten Inseln. Wir zeigen auch, dass es möglich ist, die C(100) Oberfläche in UHV nach Abtragen der $Fe_{78}Ni_{22}$ Filme durch Zerstäuben und Ätzen in atomarem Wasserstoff zu reinigen.

Auger-Elektronenspektroskopie und Niedrigenergie-Elektronenbeugung charakterisierten die Zusammensetzung und Struktur der Substrate und der abgeschiedenen $Fe_{78}Ni_{22}$-Filme auf Cu(100), Cu/Si(100) und C(100). Die $Fe_{78}Ni_{22}$-Filme auf C(100) wurden auch durch Rastertunnelmikroskopie untersucht. Wir haben die Eigenschaften der $Fe_{78}Ni_{22}$-Filme durch den magnetooptischen Kerr-Effekt sowohl vor als auch nach der Ionenstrahlbestrahlung untersucht und zeigen die Abhängigkeit der Magnetisierung von der Ionendosis.

Ähnlich wie bei H-Si wurde das Wachstum einer kontinuierlichen Cu(100)-Pufferschicht durch gepulste Laserabscheidung auf $SrTiO_3$(100) in der Literatur beschrieben. $SrTiO_3$ ist ein Prototyp eines Perowskitoxids mit einem kubischen Gitter bei Raum Temperatur. Es war jedoch nicht möglich, eine geordnete Cu(100)-Pufferschicht zu erhalten.

Die Möglichkeit, ein Standardsubstrat wie Si(100) zu verwenden, ist ein wesentlicher Schritt für Anwendungen beim Rapid-Prototyping von magnetischen Metamaterialien (unter Verwendung von FIB) und für die Massenproduktion (z. B. durch Ionenbestrahlung durch eine Maske). Das Wachstum der metastabilen Filme auf C(100) ermöglicht die Verwendung neuer Techniken (z. B. magnetische Transmissionsröntgenmikroskopie) zur Charakterisierung der magnetischen Nanostrukturen.

Contents

Abstract **iii**

Kurzfassung **v**

1 Introduction **1**

1.1 Applications of magnetic thin films 3

1.2 Metastable iron films on Cu(100) 5

1.3 Metastable iron-nickel films on Cu(100) 8

1.4 Substitution of the Cu(100) 10

2 Experimental Methods **13**

2.1 Auger Electron Spectroscopy 13

2.2 Low-Energy Electron Diffraction 15

2.3 Surface Magneto-Optical Kerr Effect 17

2.4 Scanning Tunneling Microsopy 19

2.5 Molecular Beam Epitaxy 19

2.6 Pulsed Laser Deposition 21

2.7 Reflection High-Energy Electron Diffraction 23

2.8 Ion-beam treatment 24

2.8.1 Focused Ion Beam 25

2.9 Scanning Electron Microscope 26

3 Vacuum systems **27**

3.1 The PINUP system 27

3.1.1 Source of Atomic Hydrogen 30
3.2 The RT-STM system 35
3.3 The SPECS system 36
3.4 Focused Ion Beam and Scanning Electron Microscope 38

4 Metastable Films on Copper **39**
4.1 Introduction 39
4.2 Preparation of the Cu(100) surface 40
4.3 Growth of the metastable films 41
4.3.1 Results 41
4.3.2 Discussion 42
4.4 Ion-beam induced transformation 45
4.4.1 Nanopatterning and anisotropy modification 45
4.4.2 Comparison of ion type and energy 48
4.5 Conclusion 52

5 Metastable Films on Silicon **55**
5.1 Introduction 55
5.2 Preparation of the H-terminated Si(100) surface 57
5.2.1 Results 58
5.2.2 Discussion 59
5.3 Growth of the Cu(100) buffer layer 61
5.3.1 Results 61
5.3.2 Discussion 64
5.4 Growth of the metastable films 66
5.4.1 Results 66
5.4.2 Discussion 67
5.5 Ion-beam induced transformation 68
5.5.1 Results 68
5.5.2 Discussion 70

5.6 Conclusion 72

6 Metastable Films on Diamond 73

6.1 Introduction 73

6.2 Preparation of the C(100) surface 75

6.2.1 Results 76

6.2.2 Discussion 76

6.3 Growth of the metastable films 78

6.3.1 Results 78

6.3.2 Discussion 82

6.4 Ion-beam-induced transformation 84

6.4.1 Results 84

6.4.2 Discussion 85

6.5 Conclusion 88

7 Metastable Films on $SrTiO_3$(100) 91

7.1 Introduction 91

7.2 Preparation of the $SrTiO_3$(100) surface 92

7.3 Deposition of the Cu(100) buffer layer 94

7.3.1 Results 95

7.3.2 Discussion 99

7.4 Conclusion 102

8 Summary and Outlook 103

References 107

Appendix 121

A Lists of samples 121

A.1 Cu(100) 121

A.2 $SrTiO_3$(100) 122
A.3 C(100) 123
A.4 Si(100) 124

B The hydrogen cracker **127**
B.1 Technical description 127
B.2 Technical drawings 129

C Si heating stage **149**

D Si sample plate for direct current heating **155**

List of Figures **159**

List of Tables **163**

Acknowledgement **165**

Chapter 1

Introduction

The technological advances in the 20th century allowed the study of processes at the surfaces on the atomic scale in ultra high vacuum (UHV) and thus gave rise to surface science. Thin films are a technologically significant area of surface science because of their importance in the fabrication of magnetic recording media (e.g. hard-disc drives) and semiconductor devices (e.g. light emitting diodes). The decrease in the dimensions from bulk-like materials to thin films gives rise to new phenomena in the properties of the materials. For example, the shift in volume/surface ratio changes the energy, which in turn varies the chemical reactivity, thermodynamic and structural properties [1, 2]. In the 20th century, the understanding and improvements in the growth of thin films in UHV enabled defect-free growth by, e.g., molecular beam epitaxy (MBE). The purpose of MBE is to deposit epitaxial thin films by the transfer of atoms from a heated evaporation material to the substrate. Epitaxy (introduced by L. Royer in 1928) is a connection of two Greek words epi (resting upon) and taxis (arrangement), and it describes thin films in which the lattice of the grown film is crystalline and has a similar lattice parameter like the underlying crystalline substrate [1]. The substrate plays this role because its proximity imposes an energetic barrier to the relaxation of the thin film. UHV also allows employing measurement techniques which use electrons for structural and chemical analysis because of their large mean free path in the UHV, for example, low-energy electron diffraction (LEED)

and Auger electron spectroscopy (AES). The development of scanning probe microscopies (SPM) revolutionized nanoscale investigations and allowed for measurements of the surfaces with atomic resolution. A model case for MBE thin film growth and SPM characterization is Fe on Cu(100), where the SPM allowed the measurement of details with an atomic resolution which led to the realization that needle-shaped bcc crystallites are responsible for the ferromagnetism (FM) of thin films [3–5]. It was thought previously that fcc Fe might be FM [6, 7]. The thin films of Fe/Cu(100) are the starting point for our investigations.

Magnetic properties of materials fascinated humanity since the discovery of first permanent magnets [8]. Magnetic materials can be divided into hard and soft magnets. The memory storage in nanodomains used in the hard-disc drives (HDDs) requires high magnetic saturation and coercive field to avoid loss of information and thus requires alloys described as hard magnets. The soft-magnetic materials have a small coercive field and enable the operation of flux guides and magnetic logic elements, which require fast switching rates at a low energy cost. Both categories require improvement of existing and invention of new materials with the downscaling of the magnetic elements and fabrication of magnetic nanopatterns.

As the scientific understanding of magnetism evolved, many interesting effects were discovered. In 1831, Michael Faraday for the first time experimentally verified the interaction of the photons with magnetic material [9]. He showed that polarization plane of light rotates when light is transmitted through a glass rod in a magnetic field. A similar effect has been discovered in reflection of the light from a polished piece of magnetic material by John Kerr [10]. In the 20th century, it was possible to describe, predict and experimentally verify magnetism of thin films mainly thanks to the Faraday and Kerr effects as they proved to be very versatile tool to study magnetism in thin films.

1.1 Applications of magnetic thin films

The control of the thin-film growth combined with a local change of the magnetic properties enabled improvements in the microelectronics industry, of which the most important are the HDDs and sensors. There also many approaches to magnetic nanopatterning, such as ion-induced intermixing, ion-milling or the most commonly used lithography. Ion-beam nanofabrication can either lead to the removal of FM material on a paramagnetic (PM) substrate, a FM→PM or PM→FM transition, or to a change of the coercive field or magnetic saturation [11].

An example of the applications of soft-magnetic nanopatterns in thin films is the fabrication of in-plane nanomagnetic logic (i-NML) [12]. The i-NML consists of nanomagnets and the change of the magnetization state of the nanomagnets represents the binary information. Nanomagnetic logic in the i-NML requires a local tuning of magnetic anisotropy of the thin films, which is currently supplied by shape-dependent in-plane anisotropy in Permalloy. Another option for the control of anisotropy is the use of the magneto-crystalline anisotropy through the modification of the atomic lattice in the thin films. Soft-magnetic nanostructures with tunable magneto-crystalline anisotropy fabricated via ion beam irradiation are a good candidate for the use in i-NML. The reason is that such nanostructures can reduce the switching power while their fabrication is technologically less demanding in contrast to, e.g. lithography.

A second example of the applications of soft-magnetic nanostructures with tunable magneto-crystalline anisotropy fabricated via ion beam is the utilization of the wave-like excitations of an array of electron spins. The spin wave (SW) was (indirectly) described already in 1929 by Bloch [13], and the quantum of SW oscillation has been named magnon [14]. In other words, the SW is a propagating re-ordering of both orbital and spin moments of atoms and is also defined as transport of magnons or a spin current. Magnonics is an area of science describing transport and processing of information by utilizing the wave-like properties (both amplitude and phase) of the magnons [12, 15]. SWs have similar behavior as electromagnetic or acoustic waves, and the magnon carries the information in spin angular momentum. The

wave nature of SWs moreover allows more efficient data processing than the conventional electronics because it allows for operations with clusters of information rather than with single bits [16]. Magnonic crystals consist of volumes with periodically alternating magnetic properties, where either magnetic saturation or anisotropy are locally modified to form a metamaterial. The periodic arrangement then allows only specific frequency ranges of the SWs to pass through and thus forms a band gap. The requirements for nanopatterns forming a magnonic crystal are high saturation magnetization, high Curie temperature (T_C) and low magnetic damping. For actual applications it is required that the magnonic circuits should be easy to prepare at large scales. The major drawback for magnonics with today's magnetic materials are usually the high energy losses prohibiting magnon transport over large distances. The major energy loss channels are usually magnon-magnon and magnon-phonon scattering and eddy currents.

Magnonic circuits proved to be a viable candidate for processing of information with a great extrinsic tunability of the logical elements [15]. Possible advantages of all-magnon logic are that firstly, the magnons have a low power consumption because their propagation does not involve the movement of real particles as is the case in electronics, where the electron transport leads to Joule losses. Secondly, the magnon frequency can reach the range from THz to MHz with corresponding wavelength range from nm to μm, and they transport information over macroscopic distances. However, as mentioned previously, there is a demand for new materials because the materials employed in magnon circuitry nowadays have rather high losses which limit the spin-wave propagation down to a few micrometres. This leads to the development of new materials with lower magnetic damping and improving the precision and speed of patterning, which are readily available by the films investigated in this thesis. The most commonly used materials in magnonics at the moment are Yttrium Iron Garnet (YIG), Permalloy (Py) and Co-Fe alloys. YIG has low damping, small magnetization and an insulating character [17]. Py is a soft magnetic alloy of Ni and Fe optimized for low magneto-elastic coefficients, with approx. twice the

damping of YIG [18]. The Co-Fe alloys have a similar SW damping to Py [19].

The characterization of materials allowing the study of spin waves also places a huge demand on the experimental techniques; an overview of the experimental techniques can be found in [16]. A technique commonly used for SW measurement is Brillouin light scattering microscopy, which uses the Stokes/anti-Stokes transitions in the ferromagnetic material to measure the SWs [20]. Another example is ferromagnetic resonance (FMR), which is a robust method which measures the magnetodynamic properties of bulk-like ferromagnetic materials [21]. Magneto-optical Kerr effect (MOKE) spectrometry uses the Kerr effect to measure the change in the magnetization of a sample. In the scope of this thesis, we are going to measure the magnetic properties of our thin films mainly by MOKE, because it has been implemented in our UHV setup and therefore allows for *in-situ* measurements of our thin films [22].

1.2 Metastable iron films on Cu(100)

Epitaxial thin films of Fe on Cu(100) proved to be an exciting system to study the influence of film thickness on structure and magnetism. The T_C of bulk Fe is around 770 °C, and above this temperature, Fe is paramagnetic (PM). At 911 °C, Fe undergoes a martensitic phase transition and forms a γ-Fe, which is fcc and PM [23]. It is possible, however, to stabilize γ-Fe at room temperature (RT) by depositing Fe on Cu(100), because Cu has a very low lattice mismatch to the γ-Fe and therefore promotes its epitaxial growth up to a critical thickness of $\approx$ 10 monolayers (ML) [24]. The thin films (thickness $\leq$10 ML) of Fe/Cu(100) have a plethora of magnetic and structural properties depending from the film's thickness, which were investigated since the very discovery of the epitaxial growth. The connection between the magnetism and structure was finally resolved by Biedermann et al. in 2001 by STM analysis of intermediate states of Fe thin films [3, 4].

The growth of fcc Fe leads to three main Fe phases (portrayed in Figure 1.1), which change with the thickness of the thin films. The first 2 ML intermix with Cu because

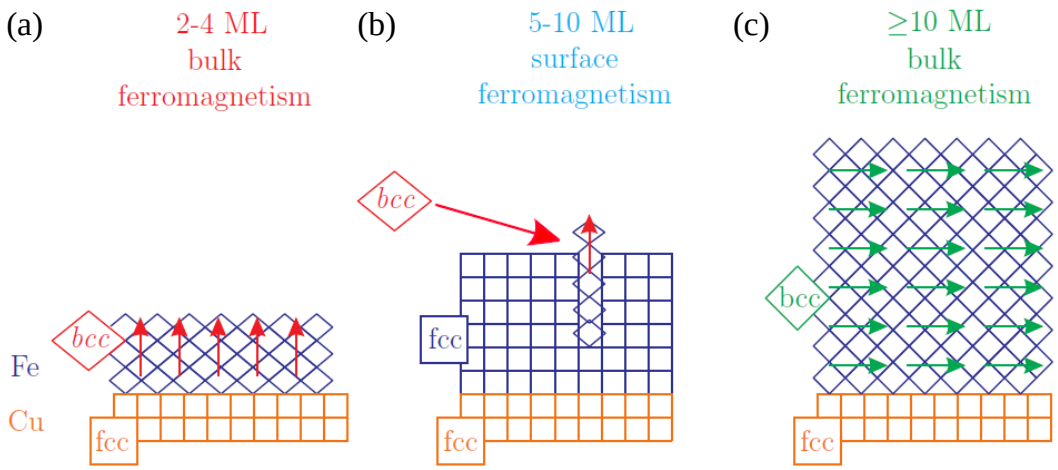

Figure 1.1 | Fe growth regimes on Cu(100) exhibit three main structural and magnetic properties. (a) below 4 ML, Fe has a bcc-like nanomartensitic structure, with out-of-plane magnetization. (b) above 4 ML and below the critical thickness of 10 ML, the films are epitaxial, fcc metastable and paramagnetic. (c) above 10 ML, the films spontaneously transform into relaxed bcc stable ferromagnetic alpha-Fe phase. Adapted from [22].

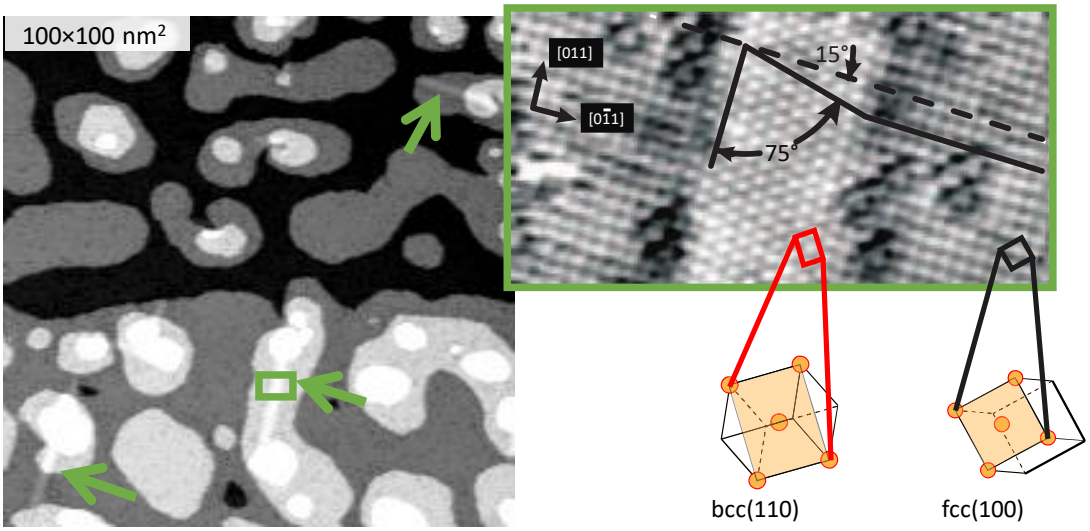

Figure 1.2 | Scanning tunneling microscopy of an epitaxial 7-ML (1.3 nm) Fe/Cu(100) film. The overview image shows Fe with 3-ML high islands of random shapes. Green arrows point to elongated protrusions in the as-deposited epitaxial film. The detail with atomic resolution portrays one of the elongated protrusions and confirms that the elongated protrusion is a strained bcc(110) needle embedded in the epitaxial fcc(100) Fe. The rows of atoms of the bcc (110) are rotated by 15 ° with respect to the rows of atoms of the fcc (100). Adapted from [3].

of the lower surface energy of Cu. Between 2 and 4 ML, the Fe is ferromagnetic (FM) with out-of-plane magnetization; it has a nanomartensitic structure [25].

The Fe films with the thickness between 5 and 10 ML are fcc Fe, which is PM. Above 4 ML, these films are metastable because the epitaxial growth forms a local energy minimum in the energetic landscape of the Fe-Fe distance [24]. Such films exhibit surface ferromagnetism with a bcc-like reconstruction [5]. At 9.5 ML, cooling leads to a transformation into the more stable bcc phase [22].

Figure 1.2 portrays a 7-ML-thick fcc Fe film on Cu(100) measured by STM, with three spontaneously created bcc "needles". An image with atomic resolution on one of these "needles" shows that the Fe organizes into a bcc(110) structure, which has the rows of atoms rotated by 15° with respect to the fcc (100). There are four different crystallographic directions, in which the bcc unit cell can orient.

The 5-10 ML thick Fe/Cu(100) are metastable and it is therefore possible to induce their transformation into the more stable bcc state by the ion beam irradiation. The ion-beam irradiation has been successfully employed to the patterning of the thin films and showed experimentally for 8-ML-thick Fe/Cu(100) [22, 26]. The fabrication of the ferromagnetic nanostructures in the metastable films does not lead to a significant change in the topography or doping of the films; also, it involves only one step in comparison to the multi-step lithography.

In the ion-beam-induced fcc-to-bcc transformation, the incoming ions create a molten volume upon collision with the atoms of the thin film, which can recrystallize into the more stable bcc structure [26]. According to the STM investigation of Shah Zaman, the creation of a bcc nuclei is a rare process, with 2×10^{-6} bcc nuclei per impinging ion [27]. Once the bcc nuclei has formed, it is a defect in the fcc lattice of the metastable film. The bcc areas then serve as nuclei for the fcc-to-bcc structural and magnetic transformation during the next thermal spike in their proximity. Thus, an ion beam can change the structural properties of the thin film (fcc to bcc), and, hence its magnetic properties (PM to FM). Employing a focused ion beam (FIB) allows ion-beam-induced magnetic nanopatterning, for example, for the fabrication of i-NML or

magnonic crystals.

Finally, the films with thickness above the critical thickness (10 ML) spontaneously transform into the more stable bcc phase, because the energetical barrier imposed by the substrate is overcome by the energetically more favourable bcc Fe phase.

It has been shown that the γ-Fe can be stabilized up to 22 ML by depositing in carbon monoxide (CO) atmosphere [27, 28]. CO dissociates at the surface of Fe and carbon is buried in the growing γ-Fe film, and oxygen floats at the surface and serves as a surfactant, promoting the layer-by-layer growth [28]. The interstitial carbon stabilizes the γ-Fe phase; this effect is in metallurgy called a "γ-loop opener" [29]. The critical thickness for the growth in CO atmosphere is 22 ML because, at this thickness, the surface gets saturated by oxygen, and the CO dissociation cannot take place anymore [27, 30]. Ion-beam-induced nanopatterning has also been shown for these CO-stabilized Fe/Cu(100) films [30, 31].

1.3 Metastable iron-nickel films on Cu(100)

The metastable films of Fe/Cu(100) are not useful for applications, because they have a small magnetic field and surface oxidation of the less-than-10-ML-thick films leads to a change in their magnetic properties (e.g. spin-wave damping). The minimum thickness useful for applications in magnonics is from our experience approx. 10 nm (50 ML). We showed that it is possible to remove the thickness limit by alloying Fe with 22% Ni [30, 32, 33] and confirmed the epitaxial growth of $Fe_{78}Ni_{22}$ up to the thickness of 130 ML.

Ni is one of the γ-loop opener metals; it is fcc and has similar atomic size and lattice parameter as Fe and thus supports the formation of γ-Fe. Figure 1.3(a) describes the evolution of the T_C and the magnetic moment for different concentrations of Ni in the Fe_xNi_{1-x} alloy [34]. The figure shows a rapid decrease of T_C for Ni concentrations below 50%, while the alloy remains fcc. T_C is above the data range shown (1040 K) for the bcc α-Fe_xNi_{1-x}. The magnetic moment rapidly decreases in the region of the

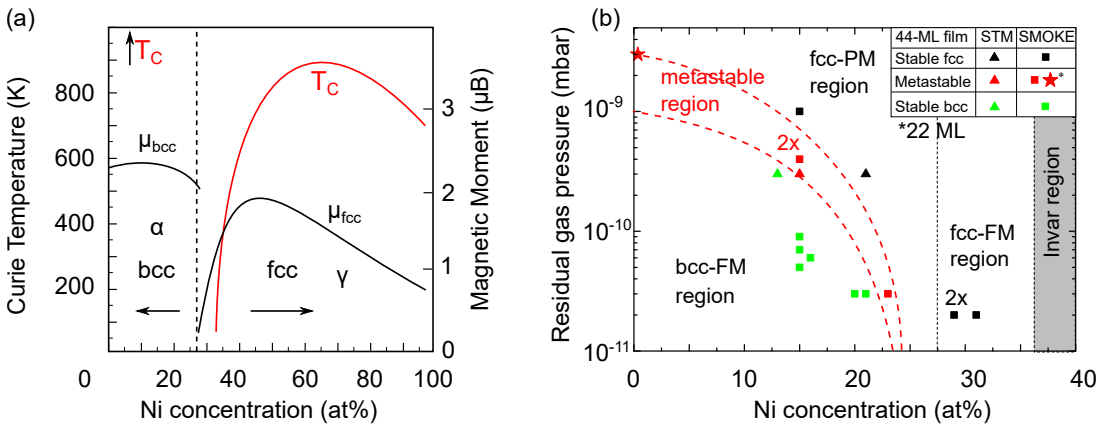

Figure 1.3 | (a) Curie temperature and magnetic moment as a function of the Ni concentration in an Fe-Ni alloy. The bcc Fe is ferromagnetic with a high magnetic moment (μ) and T_C of 1040 K. The magnetic moment and T_C decreases when moving from the fcc side to the transition region (around 25% Ni). Adapted from [34]. (b) Experimentally determined phase diagram showing the dependence of the structural and magnetic properties of a Fe-Ni alloy on the residual gas pressure and the Ni concentration. The Fe-Ni alloy was grown by MBE on Cu(100). Adapted from [32].

fcc-to-bcc transition.

Figure 1.3(b) summarizes the experimental results from depositions of Fe_xNi_{1-x} with a low Ni concentration at different chamber backpressures in a phase diagram. There are four regions in the phase diagram. For Ni concentration above 27%, the Fe-Ni alloy has the fcc structure and is FM, irrespective of the residual gas pressure (backpressure during deposition). At low Ni concentration and low backpressure, the Fe-Ni alloy does not have enough stabilizing agents for the fcc phase and it therefore grows as stable bcc α-Fe, which is FM. If, on the other hand, both the backpressure and the Ni concentration are higher, the Fe-Ni alloy grows as stable fcc, which is PM and it is not possible to induce the fcc-to-bcc transformation by the ion beam. In between these two regions is the metastable region (dashed red line). We define as metastable thin Fe-Ni films, which can be transformed via ion beam from fcc to bcc, i.e. from PM to FM. The backpressure during deposition of these thin films mainly consisted of CO, which is produced in the evaporator, which was also confirmed by quadrupole mass spectrometer. We can see that the metastable region is somewhat delicate to achieve. At the same time, it does not define the metastable region completely because further

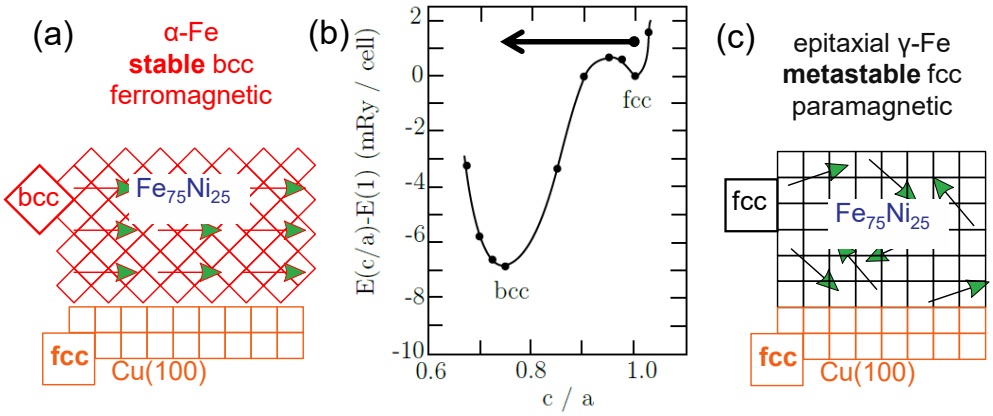

Figure 1.4 | Ion-beam-induced transformation of the metastable fcc films. Results of total-energy calculations for $Fe_{75}Ni_{25}$ show that the fcc structure is a metastable state separated by an activation barrier with the bcc structure. The scheme on the right portrays the epitaxially-grown fcc $Fe_{75}Ni_{25}$ film which transforms into bcc (left) after sufficient energy is supplied by the ion beam. The energy difference between the two structures is of the order of 1.5 (mRy)/atom. Note that the volume of the bcc structure is larger than the fcc structure. The arrow symbolizes the ion-beam-induced transition.

investigations revealed that the effect of CO decreases with increasing Ni content [33].

Figure 1.4(b) shows a calculation of the dependence of the energy in a Fe_3Ni alloy on c/a, which corresponds to the Bain path [34]. According to this calculation, the fcc structure is at a local minimum and the bcc structure is the global minimum. In case that the Fe_3Ni grows in the local minimum [fcc - Figure 1.4(c)], it is possible to induce a transformation from the local minimum to the global minimum [bcc - Figure 1.4(a)] by supplying the energy necessary to overcome the activation barrier. Ion beam can supply the energy to overcome the potential barrier, as was already discussed in section 1.2. As a result, the film is transformed from the metastable fcc to the stable bcc.

1.4 Substitution of the Cu(100)

After shifting the thickness limit for metastable films to higher values (as required by many applications), the next limiting factor for the applications is the Cu(100) single-crystalline substrate. In this thesis we study the growth of the metastable films

on new substrates, which are relevant for research and industrial applications. These are $SrTiO_3$(100), Si(100) and C(100).

It has been shown that it is possible to grow an epitaxial Cu(100) film on both $SrTiO_3$ [35] and Si(100) [36–38], which could then potentially serve as substrates for the epitaxial growth of the metastable films. $SrTiO_3$ is a prototype perovskite oxide, which is (in contrast to many other perovskites) cubic at RT and single crystals can be purchased at moderate cost. The crystallographic orientation might enable the growth of an epitaxial Cu(100) buffer layer. Si(100) is a commonly used substrate in the microelectronics industry, and growth of the metastable films on this substrate would be a significant step towards applications.

Diamond as a substrate for the growth of the metastable films is interesting for electronics because of its high thermal conductivity, the lack of electrical conductivity and chemical inertness for use in sensors. Fe creates chemical bonds to C and can, therefore, serve as a buffer layer for electrical contacts of Cu on diamond. Also, diamond is a transparent substrate for visible light, thus enabling the study of the metastable films by light transmission, if desired. C(100) can be prepared as thin free-standing nanomembranes, which can be used for the analysis of magnetic metamaterials by magnetic transmission X-ray microscopy measurements [39].

The thesis is going to start with the description of the experimental methods and follow with the description of the experimental setups used in the investigations of the growth of the metastable films on different substrates. The preparation of Si(100) for the growth of the metastable films required us to design and manufacture new apparatuses. We made a direct-current-heating stage with a sample plate and a hydrogen cracker. The hydrogen cracker was used for the dissociation of H_2 into a collimated stream of atomic H. We used the atomic H for hydrogen termination of Si(100) and for the cleaning of C(100). The direct-current-heating stage was used for cleaning of Si(100). The sample plate had to be adapted to fit the needs for direct-current heating. For more details, please refer to Appendix C. The calibration of the H-

cracker is included in the experimental section; a more detailed technical description of the equipment, along with technical drawings is in Appendix B.

The fourth chapter describes the growth of the metastable films on the Cu(100) surface. We show and discuss the ideal parameters for the growth of the metastable films and we then elaborate on their magnetic and structural properties after deposition and after ion-beam induced transformation. This chapter concludes the works we previously published [32, 33]. In this chapter, we also describe the tuning of the structure and magnetic anisotropy of the metastable films by the focused ion beam, which was published in [40].

The fifth chapter covers the research done on the growth of the metastable films on Si(100) with an epitaxial Cu buffer layer, which was published in [41]. We start with the comparison of two approaches to the preparation of the hydrogen-terminated Si(100) for the growth of the Cu buffer layer. Firstly, it is done by etching in hydrofluoric acid (HF) and secondly by a direct-current heating in the UHV, with a consequent H-termination. We then describe the properties of the Cu buffer layer grown on both, chemically and UHV-treated substrates. The metastable films grown on Si(100) with a Cu buffer layer have properties similar to metastable films on a Cu single crystal. We confirmed the applicability of the metastable films on Si(100) by large-area ion-beam-induced transformation and by fabrication of magnetic nanopatterns by FIB.

We describe the growth of the metastable films on diamond in the sixth chapter. We show that it is possible to clean the diamond with atomic hydrogen and thus remove any graphitic contamination, which was not previously possible by chemical etching. The clean diamond substrate then serves as a substrate for growing metastable films at an increased temperature. Similar to the previous chapter, we confirm that it is possible to transform these films with an ion beam.

In the seventh chapter, we briefly describe an attempt to grow the metastable films on $SrTiO_3$(100) with a copper buffer layer. We show, that we were not able to prepare an epitaxial buffer layer and discuss the reasons for it.

Chapter 2

Experimental Methods

In this chapter, we briefly discuss relevant experimental techniques and their theoretical concepts.

2.1 Auger Electron Spectroscopy

We measured the chemical composition (stoichiometry and impurity levels) of our samples by Auger electron spectroscopy (AES). In AES, the samples are bombarded by electrons with an energy between 2 and 10 keV. We used 3 keV for Cu(100), STO(100) and Si(100); in case of diamond, the electron energy was decreased to 2 keV to reduce charging effects. Figure 2.1 shows the schematic view of how the Auger electrons are emitted. Collision of the incoming electrons with the surface atoms results in excitations which decay by emitting secondary electrons and Auger electrons. The energy of the Auger electrons is characteristic for each element and it is independent of the energy of the incident electrons and can be expressed as:

$$E_{Auger} = E_1 - E_2 - E_3 - \Phi \tag{2.1}$$

where

- E_{Auger} is the kinetic energy of an Auger electron,

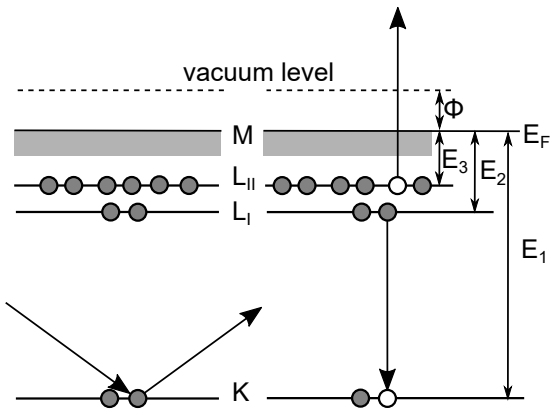

Figure 2.1 | Schematic view of energy levels inside an atom, the creation of a core hole by an incoming electron and of the Auger electron's emission process.

- E_1 is the binding energy of an electron that is emitted from the core of the atom,
- E_2 is the binding energy of the filling electron, which substitutes the electron emitted from the core,
- E_3 is the binding energy of the Auger electron,
- Φ is the work function of the material.

Figure 2.1 shows that the process begins with the incident electron, which removes a core electron. The atom is therefore given a well-specified energy E_1, which is then consumed by the consequent electron transition (E_1-E_2) and Auger electron emission (E_{Auger}).

The AES spectra were measured by a cylindrical mirror analyser with a concentric electron gun. The source of primary electrons was a tungsten cathode focused to a beam of approx. 0.5 mm diameter. The beam had a perpendicular incidence to the surface.

Because Auger electrons are emitted essentially from the first few ML (up to 10 ML for high energies) [42], AES is a surface sensitive method. In this thesis, AES was used to check the cleanliness of the substrates and the composition of the films. AES can be used for a rough quantitative analysis (the error can be up to the factor of 2) of the elements present on the surface of the sample, when we assume a homogeneous

distribution of all atoms over the surface. The AES spectra shown in the scope of this thesis have been normalized to the average peak-to-peak height (APPH) of the dominant peak. Concentration values of the surface of Cu, C, Si or $Fe_{78}Ni_{22}$ thin films were obtained using relative elemental sensitivity factors [43], because the probability of the emission of the Auger electrons varies with elements. The concentration was then estimated from the Equation 2.2, where x stands for an element, whose concentration we aim to calculate and i encompasses all of the elements that have some signal in a measured Auger spectrum. I is the measured APPH and S is the sensitivity factor of an element.

$$C_x = \frac{\frac{I_x}{S_x}}{\sum \frac{I_i}{S_i}} \tag{2.2}$$

2.2 Low-Energy Electron Diffraction

Low-energy electron diffraction (LEED) is a technique for the measurement of surface structure in a reciprocal space. The structure of the surfaces in this thesis was determined mainly by LEED. The LEED images presented here were post-processed with a dark-field subtraction, flat-field normalization and inverted [44].

Davisson and Germer observed in the 1920s diffraction effects of electrons backscattered from a single crystal of Ni [45], which developed to a typical surface science method [2]. The electrons in LEED have energies in the range 50–500 eV, which correspond to de-Broglie wavelengths of 0.5–2.7 Å. These wavelengths are comparable to atomic distances, hence the diffraction condition must be satisfied in crystal lattices. The mean free path of electrons with these energies is only a few ML, which makes LEED a highly surface-sensitive technique. We use the reciprocal space to describe the behavior of diffracted electrons and the creation of a diffraction pattern. The energy of the incident electron beam is:

$$E = \frac{\hbar^2 k_0^2}{2m} \tag{2.3}$$

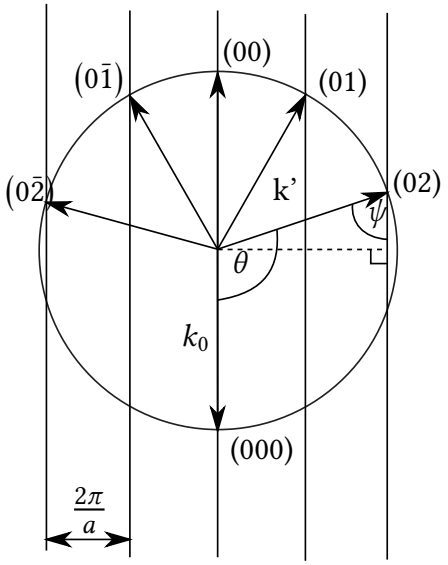

Figure 2.2 | Schematic view in reciprocal space for an electron beam incident normal to the surface - Ewald sphere construction. Here $\vec{k}_0$ is the incident wave vector, $\vec{k}'$ is the scattered wave vector, θ is the diffraction angle and ψ is the exit angle to the surface normal. Adapted from [33].

where $|\vec{k}_0| = 2\pi/\lambda$ is the wavenumber of the incoming electron beam and λ corresponds to its wavelength. The condition for constructive interference in the reciprocal space can be determined by applying the law of conservation of momentum:

$$\left(\vec{k}_0 - \vec{k}'\right)_{||} = \mid \vec{G} \mid \tag{2.4}$$

where $\vec{k}'$ is the scattered wave vector and $\vec{G}$ is a vector of the reciprocal lattice. As scattering is elastic, $|\vec{k}_0| = |\vec{k}'|$.

The Ewald sphere construction shown in Figure 2.2 expresses the conservation of momentum from Equation 2.4 in geometrical terms. Vector $\vec{k}_0$ with its tip pointing towards the origin of the reciprocal space, (000), represents the wavevector of the incident electron beam. A circle with radius $|\vec{k}_0|$, centred at the origin of the vector is a projection of the Ewald sphere. Its significance is that it maps the magnitude of $\vec{k}_0$ onto the reciprocal lattice. No diffraction events can occur outside this sphere. If any of the reciprocal lattice "rods" are intersected by the Ewald sphere, then the elastic scattering condition from Equation 2.4 is satisfied, thus giving rise to the scattered

beam with a wavevector $\vec{k}'$. This means that there is a change in momentum of the incident beam, but not its energy. The points of intersection in the reciprocal space will then show as bright spots on the fluorescent screen of the LEED.

2.3 Surface Magneto-Optical Kerr Effect

Magneto-optics describe the effect of a magnetic material on an electro-magnetic wave [46]. The reason for the effect of the magnetization on the incident light is spin-orbit coupling. Because of spin-orbit coupling, a change of the electron spin due to an external magnetic field leads to a change in the dielectric tensor. As a consequence, the magnetic material has different refraction indices for left and right polarized light. A linearly-polarized light is a superposition of two circularly polarized light-waves (with an opposite direction). Linearly-polarized light therefore changes into elliptically-polarized upon reflection from or transmission through a magnetic material due to a phase shift and different absorption rate of the two circularly polarized light-waves. This change can be expressed in the terms of the Kerr rotation and ellipticity (see Figure 2.3).

In case of transmission of the incident light, the magneto-optical effects are called Faraday (or Voigt) effect and in case of reflection, the Kerr effect. Both effects can be described by the complex angle Φ_K or Φ_F, which is proportional to the magnetization $\vec{M}$ of the sample. This angle consists of two parts; the real θ, which expresses the direction and magnitude of rotation and imaginary ϵ, which describes the ellipticity. Both variables are shown in Figure 2.3.

The SMOKE setup in PINUP (see Section 3.1) measures either in the in-plane (longitudinal) or out-of-plane (polar) mode. The magnetic field is induced by electromagnets consisting of ex-situ coils and of yokes reaching into the vacuum chamber. The maximum magnetic field in a 3-cm-wide gap is approx. 100 mT. The measurement of the change of the Kerr ellipticity is performed by a photodiode on a photoelastically-modulated He-Ne-laser light, which has laser spot diameter of approx. 1 mm. The

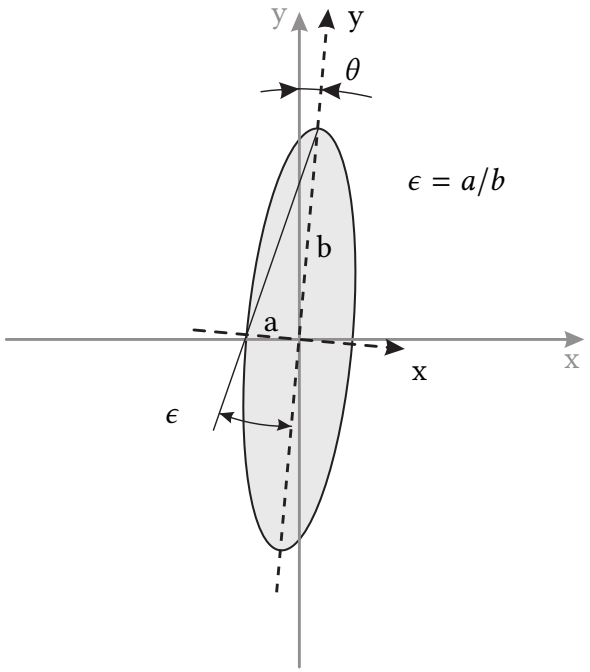

Figure 2.3 | Schematic view of the angle of rotation θ and the ellipticity ϵ, which define the complex number Φ of the Kerr effect. Adapted from [22].

longitudinal and polar geometry have the angle of incidence 60° or 30°, respectively. For more experimental details, please refer to [22]. In the case of Si(100), C(100) and $SrTiO_3$, the plane of incidence and the direction of the magnetic field were parallel to the (010) plane.

In the ex-situ experiments for the measurement of magnetic microstructures, we used a home-built micro-Kerr magnetometer MIRANDA [47] and a wide-field Kerr microscope (Evico magnetics). The Kerr magnetometer/microscope MIRANDA is capable of quantitative measurement of all three orthogonal components of the Voigt vector (which is proportional to magnetization, i.e. Kerr effect). The measurement of the Voigt vector is allowed by tilting the microscope objective from the apparatus symmetry axis, which allows to select the k-vector of the illuminating laser beam. The setup allows to measure Kerr angles with a precision of $\leq 5 \times 10^{-7}$ radians and with the spatial resolution of 600 nm. The wide-field Kerr microscope from Evico magnetics was used for simultaneous measurement of the magneto-optical effect of an array of microstructures.

2.4 Scanning Tunneling Microsopy

Scanning tunneling microsopy (STM) [48] is an important tool for a real-space analysis at the atomic level. In STM, the tunneling probability T between two conductors separated by an insulating layer is proportional to the intensity of the wave function:

$$T \propto \mid \psi(z) \mid^2$$

where the wave function is a solution of the time-separated 1D Schrödinger equation. The electron wave function exponentially decreases with the thickness of the insulating layer

$$\psi(z) \propto \exp\left(-z\sqrt{\frac{2m\phi}{\hbar^2}}\right)$$

Here, ϕ describes the potential in the rectangular barrier $\phi = V - E$, where V is the potential barrier height and E is the electron energy. We consider only electrons close to the Fermi level; the potential in the rectangular barrier ϕ is, therefore, the work function.

As a consequence, the tunnelling current I (directly proportional to the transmission probability T) depends exponentially on the sample-tip distance. The exponential decrease of the tunnelling current leads to a very sensitive response to a change of the sample-tip distance (z). For example, a change of $z = 1\,\text{Å}$ for work function $\phi = 3\ldots5\,\text{eV}$ leads to a change in the tunnelling current I by a factor 5 to 10. The STM signal (tunnelling current) arises from the convolution of the signal obtained from the tip and from the sample. In this way, sharp transitions on the surface (e.g. step bunches) are going to ”image” the shape of the tip.

2.5 Molecular Beam Epitaxy

Molecular beam epitaxy (MBE) is a growth process of an evaporated material whose structure is determined by a substrate [1, 2, 49].

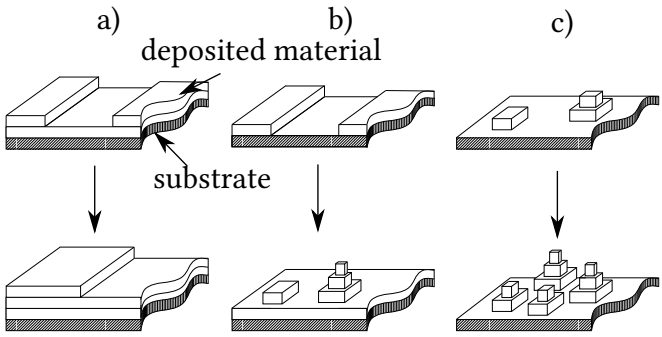

Figure 2.4 | The main growth modes during MBE. (a) shows the layer-by-layer growth, (b) the layer-and-island growth and (c) the island growth. Adapted from [30].

The growth during MBE can be described by the surface energy of the substrate (γ_S), film (γ_F) and interface energy between the substrate and film (γ_{SF}). The surface energy is defined as the free energy (per unit area) necessary to create an additional surface area. Alternatively, γ is also force per unit length and thus the following equation must be satisfied during the MBE growth in the UHV (with an exception[i]), where ϕ is the contact angle between the tangent to the surface and the film [1, 2, 49]:

$$\gamma_S = \gamma_{SF} + \gamma_F \cos\phi \tag{2.5}$$

Under near-equilibrium conditions, we distinguish three main growth modes of films thicker than one monolayer (ML), which can be described by the formula 2.5 [1, 2, 49]:

Firstly, the layer-by-layer growth is characterized by growth of consecutive full layers. The reason for this is that there is a stronger interaction between the substrate and the atoms of the layer than between the atoms in a layer. This growth is also known as the Frank-van der Merwe growth and it is shown in Figure 2.4(a). It takes place, when $\gamma_S \geq \gamma_{SF} + \gamma_F$ and $\phi = 0$. One of the systems described in this thesis, $Fe_{78}Ni_{22}$/Cu(100), is known to grow in this way.

Secondly, layer-and-island growth [see Figure 2.4(b)] is defined by growth of islands

[i] In case that the $\gamma_S > \gamma_F$ and $\gamma_{SF} \approx 0$, the equation 2.5 cannot be fulfilled, because $\cos\phi$ would have to be > 1. In this case, the system follows the Frank-van der Merwe growth.

on one or a few completed layers of the film material. This mode is observed either when the lattice parameter of the film is different from that of the substrate, or when the symmetry (orientation) of the film is not energetically favorable with respect to the crystal lattice of the substrate. For the first layer(s), the same equation as for Frank-van der Merwe (layer-by-layer) growth must be valid. Only for thicker films with the bulk structure of the film material, γ_{SF} becomes unfavorable. In other words, after deposition of several layers the strain in the film becomes too large, the layer-by-layer growth is then destroyed and small islands are formed. This mode is also called the Stranski-Krastanov mode [50]. It takes place, when $\gamma_S < \gamma_{SF} + \gamma_F$ and $\phi \geq 0$, and there is a strain build-up during the growth, which later leads to breaking of the film.

Finally, there is the island growth mode, in which the evaporated material grows in islands with no initial full layers formed, because the interaction between the deposited atoms is stronger than between the atoms and the substrate. It is also known as the Volmer-Weber growth mode and is shown in Figure 2.4(c). It takes place, when $\gamma_S < \gamma_{SF} + \gamma_F$, which leads to $\phi > 0$. $Fe_{78}Ni_{22}$ grows in this way on C(100) and also Cu on Si(100) and Cu on $SrTiO_3$(100).

In MBE, the deposited material is heated to a temperature where it starts to sublime from the solid phase or evaporate from the liquid phase. The heating can be performed via e-beam bombardment, or indirectly via heating of a crucible (Knudsen effusion cell).

2.6 Pulsed Laser Deposition

Pulsed Laser Deposition (PLD) is one of the techniques allowing a well-defined growth of thin-films. Figure 2.5 shows a schematic of the PLD process. In this method, a pulsed UV-laser is focused onto the target material inside a vacuum chamber. When the laser light supplies sufficient energy, the target material evaporates and forms a plume, which condenses on the substrate surface [51, 52]. The energy of the ab-

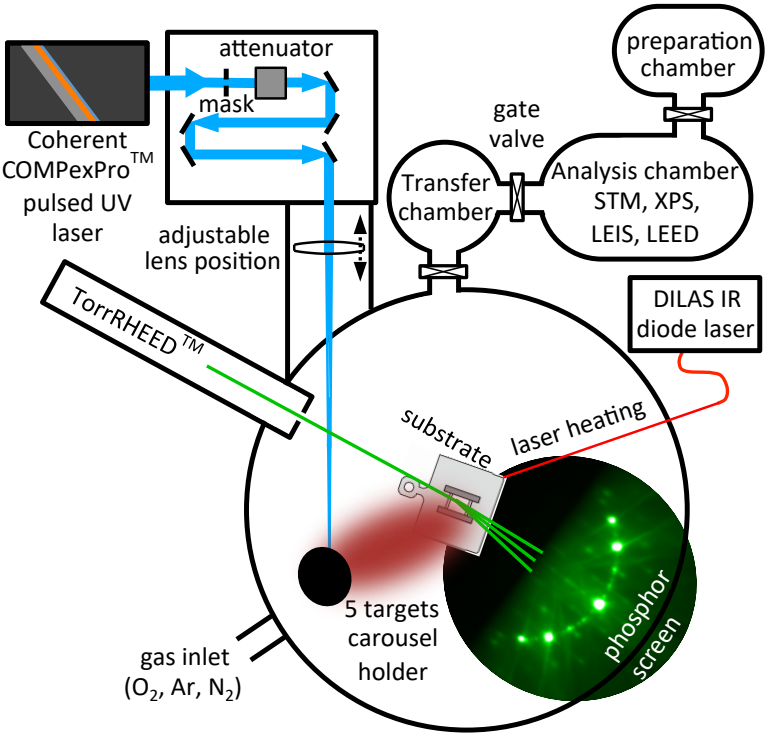

Figure 2.5 | Schematic view of the PLD setup with *in-situ* RHEED analysis and the connected UHV chambers. Pulsed ultra-violet laser, continuous infra-red laser, RHEED beam, and plasma plume are highlighted in pale blue, red, green, and brown, respectively. Adapted from [51].

lated atoms is of the order of 10 to 100 eV per particle (much larger than 0.1 eV in thermal deposition) and can be moderated by interaction with an ambient gas in the system. Thus, the pressure of the ambient gas is an extra variable in the growth of the thin films by PLD [53]. PLD provides extremely high instantaneous flux while keeping comparable time-averaged growth rates as MBE [52]. A typical duration of PLD flux pulses is 50 μs with a deposition flux of 0.05 ML/pulse (20 pulses/ML). The typical instantaneous flux in PLD therefore is 1000 ML/s, whereas a typical MBE deposition speed is 1 ML/min = 0.017 ML/s. The growth regime is dominated by this high instantaneous flux, which favours the layer-by-layer growth. In the case of homoepitaxial growth, the landing atoms will have to travel shorter paths to reach island edges where they can descend, see Chapter 8 in [52]. In the case studied in this thesis (growth of a metal on an oxide), however, the Frank-van der Merwe growth is thermodynamically favored. As a result, the higher density of island nuclei should

make the coalescence of island nuclei more likely [54].

2.7 Reflection High-Energy Electron Diffraction

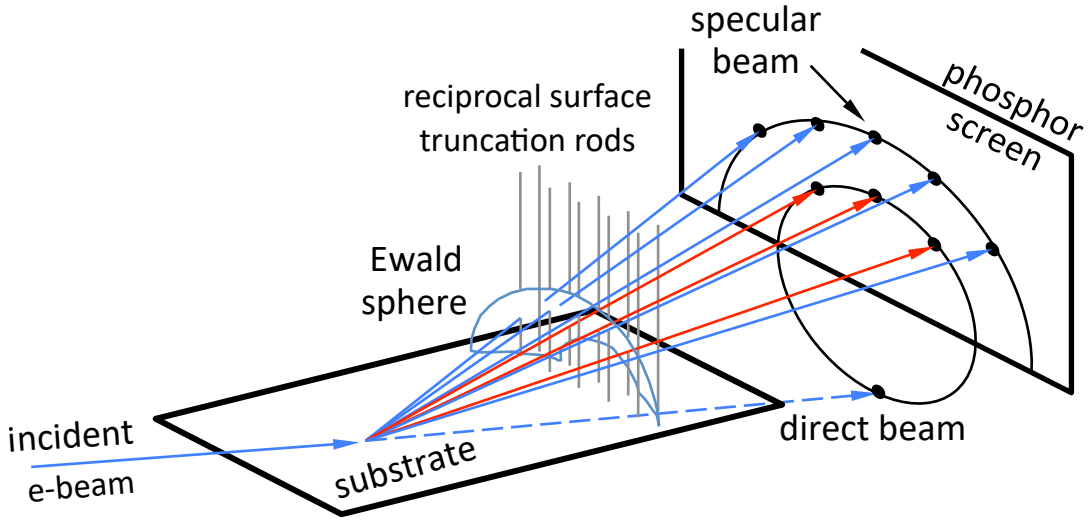

Figure 2.6 | Schematic description of RHEED, adapted from [55].

Reflection high-energy electron diffraction (RHEED) is UHV method for the measurement of the structure of a surface in the reciprocal space. Figure 2.6 shows the setup of RHEED in which the incident beam approaches the substrate at grazing incidence. The grazing incidence enables simultaneous RHEED analysis of the growing thin film. The typical electron energies in RHEED are in the of range 10–50 keV. The diffraction pattern appears on the phosphor screen when electrons scatter elastically from a crystal. The scattered waves lie on the Ewald sphere described in Section 2.2. The intersection of this sphere with the surface truncation rods of the sample surface determines where the Bragg condition is fulfilled and the projection of these intersections shows as diffraction spots on the RHEED screen.

The intensity of specular spot on the phosphor screen is maximized when the electrons elastically scattered from neighbouring terraces on the substrate interfere constructively. In this setup, the highest intensity of the specular spot can be expected for an perfectly flat surface. At the same time, during deposition, a decrease in the

intensity of the specular spot would mean that the material deposited on the surface leads to scattering of the electrons. In case of layer-by-layer growth, however, the intensity of the specular spot would return to its previous intensity after a completion of each monolayer. Kikuchi lines running through the bulk-derived spots in the RHEED pattern indicate a flat surface with a high order of crystallinity, i.e. they correspond to a flat, well-defined crystalline surface [52].

2.8 Ion-beam treatment

We used the raster ion sputter gun and the focused ion beam for the irradiation of the metastable films. When the ions hit the surface of a film, they penetrate into a depth depending on their mass, energy and on the material. The particular case of the metastable films irradiated by Ar^+ and Ga^+ is going to be discussed in Section 4.4. On their way through the film, the ions lose their energy due to elastic and inelastic collisions with the target atoms and electronic energy loss interactions [56]. Elastic collisions cause energy loss of the ions because the energy is transferred to target atoms (nuclear energy loss interactions). The electronic energy losses are due to interaction with the electrons of the target atoms. The ions and the energetic target atoms form collision cascades in the target material. The collision cascade consists of atoms/ions with a large energy (of the order of tens of eV to keV, dependent upon the energy of the incident ion). The high energy of the atoms after the collision cascade has happened can be described on the base of a thermal spike model [57]. In the thermal spike model, the impact of a single ion deposits enough energy to a small volume in the target material so that it melts. The temperature then within picoseconds decreases because of the heat exchange with the surroundings and the melt therefore recrystallizes. The recrystallization should usually be pseudomorphic with the surroundings. However, there are multiple mechanisms, which give rise to crystallographic defects during the recrystallization [30].

Firstly, in case that the collision cascade deposits high energy more than one place,

the recrystallization front might not be spherical and the quenching of the molten volume might result in a sheared structure, which might be a nucleus of a bcc crystallite [26, 27]. A second example is when the thermal spike occurs at the surface of the target, where the fluid can flow out of the original melt. A rapid cooling on the surface does not allow the volume at the surface to move back to the original melt and to recrystallize in its original position. Thus, as the melt cools from outside to the centre, a vacancy defect forms in the centre of the previously molten volume [30]. Finally, when the thermal spike occurs at the interface of two different materials, it leads to their intermixing, thus creating a new phase in the system. The radius of the molten volume can then give an estimate to how large is the intermixed phase at the interface of the thin film and the substrate. The size of the molten volume V_{melt} can be estimated from:

$$V_{melt} = V_{atom} \times N_{melt} \tag{2.6}$$

with N_{melt} being the number of atoms in the V_{melt} [57]:

$$N_{melt} \approx \frac{E_{nucl}}{14 k_B T_{melt}} \tag{2.7}$$

where V_{melt} is the molten volume, V_{atom} is the atomic volume, k_B is the Boltzmann constant, T_{melt} is the melting temperature of the target atom and N_{melt} is the number of atoms in the molten volume. E_{nucl} is the energy transferred to the target atom in the nuclear collision, which we calculated using the computer code ”Stopping and Range of Ions in Matter” (SRIM) [58].

2.8.1 Focused Ion Beam

FIB is a tool for laterally well-specified irradiation of materials by the ions. Focused ion beams are used for preparation of samples for transmission electron microscopy, manufacturing the nano-sized elements, imaging of the surface via either the scattered ions, or the secondary electrons, etc. [11]. Direct writing by FIB can combine a series of techniques such as milling, implantation, ion-induced deposition,

ion-assisted etching and energy transfer associated with structural (phase) change. In the current work, the latter method was used; we varied the irradiation dose and scanning sequence between individual areas.

2.9 Scanning Electron Microscope

SEM uses electrons for imaging of the surface and it can be considered a substitute for optical microscopy at the nanoscale because of the lower wavelength of electrons compared to photons. The SEM signal results from interactions of the e-beam with the atoms of the thin film at various depths. The most commonly measured signals in SEM are the secondary electrons (SE) and the back scattered electrons (BSE). The SE are emitted from the topmost few nanometres of the thin film and their signal depends on the work function of the material. The work function is the energy necessary to remove an electron from a solid to vacuum. BSE are beam electrons reflected from the thin film by elastic scattering and can emerge from down to 10 nm deep in the thin film. An effect observable on single crystals is channelling and the formation of Kikuchi lines. Channelling occurs when electrons penetrate deeper under particular angles, which correspond to the low-order index directions of the crystal [59]. We could observe a contrast in the SE thanks to the channelling of the electrons on the system of the metastable films on Cu(100) [40].

Chapter 3

Vacuum systems

In this chapter, we describe four vacuum systems in which we performed the experiments.

3.1 The PINUP system

The ultra-high vacuum (UHV) system PINUP (Projekt Ionenneutralisation und Ultraviolett-Photoelektronenspektroskopie) is a μ-metal UHV chamber for both preparation and analysis of samples; its scheme is shown in Figure 3.1. The chamber was pumped with a Pfeiffer-Balzers turbomolecular pump (TMP),which was in October 2018 replaced by Pfeiffer HiPace 700 TMP. With the help of a titanium sublimation pump (TSP), the chamber has a base pressure of 5×10^{-11} mbar. The samples are inserted via loadlock which is separated from the main chamber by a manually operated gate valve. Before transferring new samples to the preparation chamber, the loadlock has to be baked for at least 5 hours and cooled down for 2 hours to preserve a low pressure in the main chamber during the transfer. A magnetically-coupled manipulator with linear and rotary motion is used for transfer between the loadlock and the main chamber.

The main chamber of PINUP (Figure 3.1) is equipped in the first level with a raster ion sputter gun (SPECS^{TM} IQE 12/38) with a Wien filter (we used a magnet for the

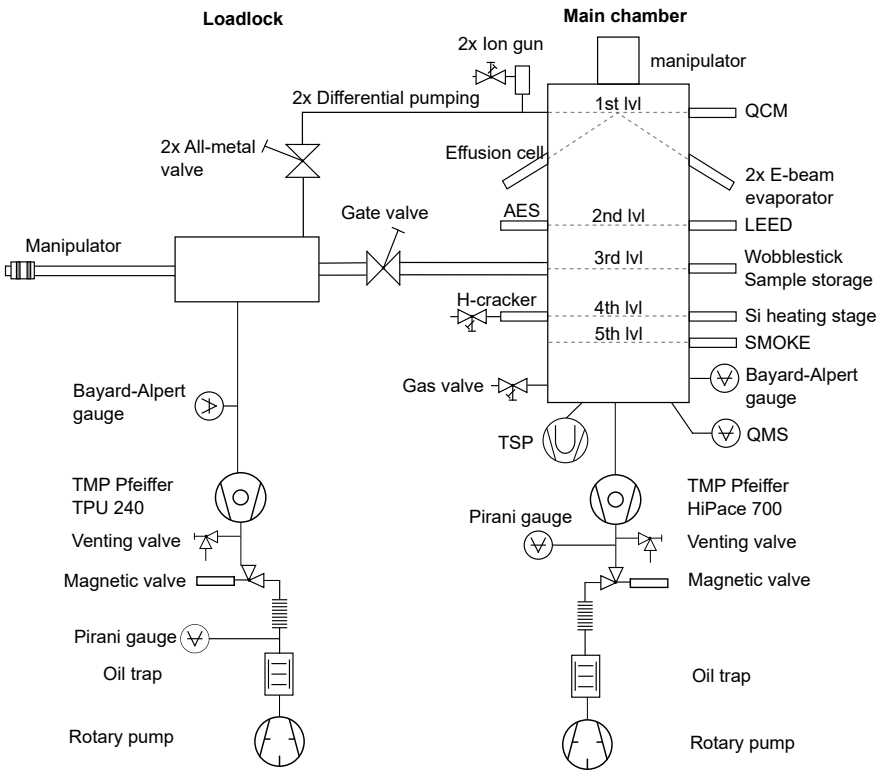

Figure 3.1 | Scheme of the PINUP chamber, which consists of two UHV vessels.

separation of lighter elements), a broad-beam Ar^+ ion gun for sputtering (Leybold Heraeus). The raster sputter gun was used for large-area irradiation throughout the in-situ experiments and it can also be used in combination with the Low Energy Ion Scattering (LEIS). For deposition, there are two electron-beam evaporators EFM3 (Focus) and EFM3T (Focus), and a Knudsen effusion cell (CreaTec). Deposition rates were calibrated with a quartz crystal microbalance (QCM), which can be moved to the position of the substrate, and the deposition was done at room temperature (RT) unless mentioned otherwise.

Cu was evaporated from crucibles in two sources, the e-beam evaporator EFM3, and the Knudsen effusion cell. The material of the effusion cell crucible contained a small amount of Ca contamination. Due to the thermal radiation, the temperature of the sample increased by 10 K during the deposition from the effusion cell. The pressure during the Cu deposition from both Cu sources was 10^{-10} mbar (with the help of a liquid-nitrogen-cooled cryopanel and the TSP). The deposition rate of both

Cu evaporators was 0.06 $Å s^{-1}$ (approx. 5.8 h for 130 nm).

The $Fe_{78}Ni_{22}$ layers were evaporated by the e-beam evaporator EFM3T (Focus) from a rod with a 2 mm diameter (MaTecK). A repelling voltage of +1.5 kV was applied to a cylindrical electrode (flux monitor) in the orifice of the evaporator to suppress high-energy ions, which may modify the growth mode of the films [60]. The base pressure during the deposition was 8×10^{-11} mbar, which was on purpose increased to 5×10^{-10} mbar of carbon monoxide (CO) to stabilize the fcc phase in line with previous observations [32]. The deposition rate of $Fe_{78}Ni_{22}$ was 0.02 $Å s^{-1}$ (approx. 1 h for 8 nm). The deposition was interrupted in 5-minute intervals at which we measured the ion flux and thereby verified that the deposition rate is constant.

In the second level are the analytical techniques, low-energy electron diffraction (LEED) (erLEED 1000-D) and Auger electron spectroscopy (AES) (Perkin-Elmer).

Below these (third level) is the sample storage and a wobblestick for transfer of the samples from the loadlock.

In the fourth level are devices which were built as a part of this thesis: a hydrogen cracker and a direct-current (DC) heating stage. For more details on the H cracker, please refer to Section 3.1.1 and for technical drawings to Appendix B. We designed and assembled the home-built heating stage for DC heating of Si samples; for technical drawings please see Appendix C.

A home-built surface magneto-optical Kerr effect (SMOKE) setup described in Section 2.3 and in [22] is in the fifth level.

The chambers are equipped with several leak valves to dose controlled amounts of CO, Ar, H_2, and O_2. The composition of the residual gas can be checked with a quadrupole mass spectrometer (QMS Pfeiffer Prisma Plus 220). The manipulator can be cooled down to 100 K by flowing cooled, gaseous N_2 through it. By counter-heating, the temperature of the manipulator can be stabilized between 100 K and room temperature. The maximum temperature reached by the e-beam heating of the target is 1100 K, when the copper cooling block is disconnected from the manipulator. Target holders for the DC heating were made of Mo; their design was similar to

that of a commercially available (Omicron) sample plates for the DC heating and can be found in Appendix D. The temperatures during experiments were checked by a thermocouple on the manipulator and by a pyrometer (IMPAC IGA 140/23). For details on the sample treatment, please refer to sections 4.2, 5.2, 6.2 and 7.2, and for an overview of the samples used, please refer to Appendix A.

3.1.1 Source of Atomic Hydrogen

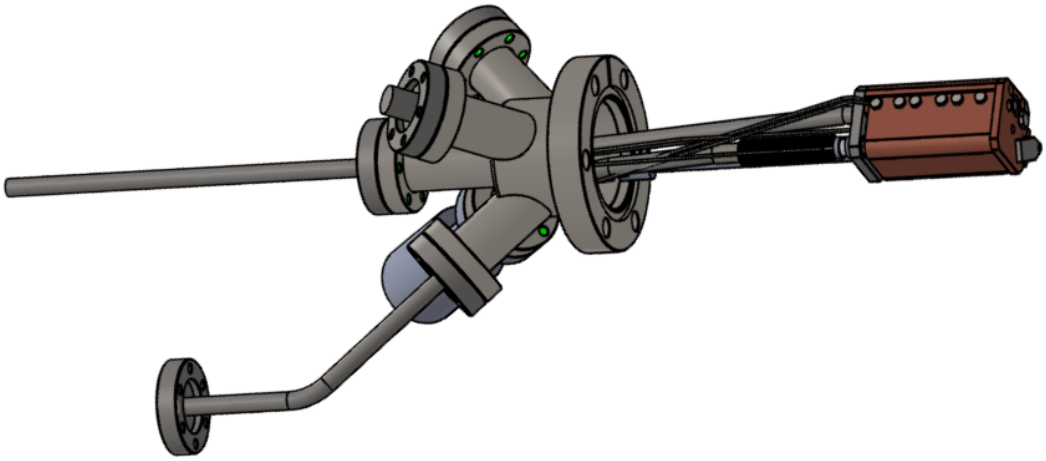

Figure 3.2 | A 3D view of the home-built H-cracker.

Atomic hydrogen is commonly applied in modern technologies in, for example, synthetic diamond production, aluminium etching or cleaning of semiconductors because of its high reactivity in comparison to H_2 [61]. We designed and built a source of atomic hydrogen, or H-cracker, which we then used for experiments on diamond and silicon. Its design was adapted from the design of Bischler [62] and it is shown in Figure 3.2. Molecular H_2 is introduced by a variable leak valve into a tungsten capillary (0.6 mm inner diameter), which is heated by 1 keV electron bombardment from a tungsten filament to approx. 2000 K. For a detailed technical description, please refer to Appendix B. The end of the capillary was approx. 3 cm from the sample. A liquid-nitrogen-cooled Cu plate between the W tube and the sample limits the sample heating to approx. 1 K/min. The temperature of the capillary was measured

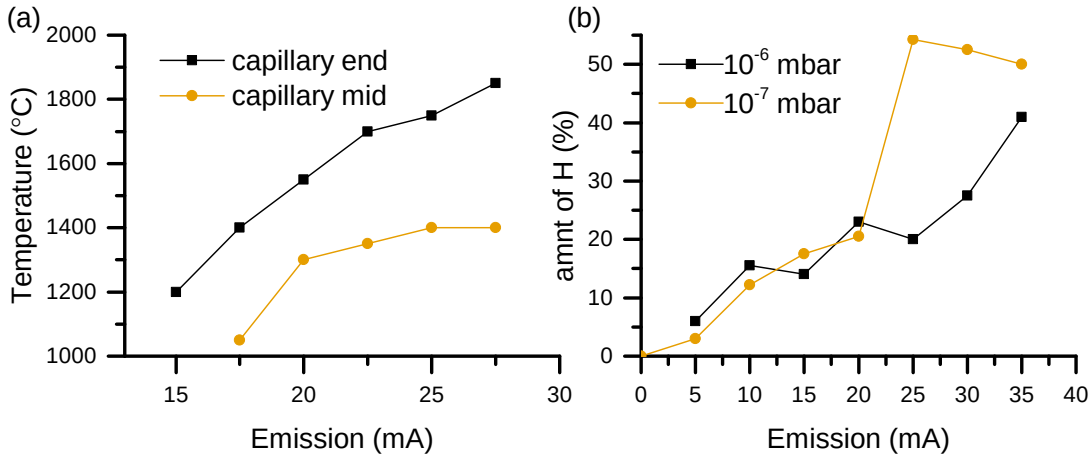

Figure 3.3 | (a) The temperature of the tungsten capillary for different emissions at the middle (orange) and end (black) of the capillary. Temperatures below 1200 °C are not plotted since they could not be measured precisely. An error of 50 °C is expected for all measurements. (b)The dependence of the amount of atomic H reaching the QMS on emission current of the filament, measured by percentual increase in the signal of atomic H on the QMS. Measurements at 10^{-7} mbar (orange line) and 10^{-6} mbar (black line).

by a disappearing filament pyrometer and its dependence on the emission current is plotted in Figure 3.3(a). A temperature of 1800 °C should lead to a complete dissociation of H_2 at a 10^{-6} mbar H_2 pressure and a well-collimated stream of atomic H should leave the capillary [61]. It should be noted, that the temperature of the tube decreased with increasing pressure, approximately by 100 K when going from 10^{-7} mbar to 10^{-6} mbar.

The efficiency of the H-cracker was measured by placing the quadrupole mass spectrometer (QMS) in direct line of sight of the tungsten capillary. The measurement confirmed an increase in the atomic-H signal upon opening the shutter on the H-cracker. The hydrogen pumping speed and compression ratio of the 30-years-old Pfeiffer-Balzers turbo-molecular pump (TMP) was extremely low and we therefore had to perform measurements in large background pressure, which did not allow for a sound quantification of the data. According to Figure 3.3(b), the H-cracker was the most efficient when running at 25 mA for 10^{-7} mbar and at 35 mA for 10^{-6} mbar pressure in the UHV chamber. We measured the temperature of the cooling shroud by a K-type thermocouple for different emission currents. At 30 mA, the temperat-

ure settled at ≈520 °C and at 35 mA, this was ≈600 °C when cooling by water. The temperatures were ≈40 °C lower when cooling with liquid nitrogen. We were careful in avoiding any "shortcut" in the cooling line. We attribute the extremely high temperature of the cooling shroud to a very low contact area between the cooling rod (stainless steel feedthrough) and the copper blocks (cooling body). This can be improved by using, for example, a tin or silver paste to increase the contact area between the cooling rod and the copper blocks.

We want to estimate the amount of atomic hydrogen produced by the H cracker to know the dose necessary for H termination of Si (Chapter 5) and cleaning of diamond (Chapter 6). For this, we use the following assumptions

- the H_2 molecules form an ideal gas in a molecular flow regime, and completely dissociate into atomic H
- the effective pumping speed of H_2 (including the effects of finite compression by the pump) is $S_{H_2} \approx 100\, Ls^{-1}$
- the base pressure of the PINUP chamber is neglected, because it is four orders of magnitude lower than the H_2 pressure
- the amount of H bound in the reactions is neglected, because the expected reactivity with diamond and silicon is negligible in comparison to the H_2 pressure

The pumping speed of the vacuum pump is:

$$S = \frac{dV}{dt} \quad , \tag{3.1}$$

where V is the volume of the chamber and t is time. The equation of state for an ideal H_2 gas yields

$$pV = \frac{1}{2} N_{H_2} k_B T \quad \left/ \frac{\partial}{\partial t}\right|_{p,T} \tag{3.2}$$

where p is the chamber pressure $p = 1{\times}10^{-6}$ mbar, N_{H_2} is the number of H atoms, k_B is the Boltzmann constant and T is the temperature. We can re-write this equation from

the partial derivation into a derivative, while keeping the pressure in the chamber and its temperature constant.

$$\left.\frac{\partial pV}{\partial t}\right|_p = \left.\frac{\partial N_{H_2} k_B T}{\partial t}\right|_T \tag{3.3}$$

$$p\frac{dV}{dt} = k_B T \frac{dN_{H_2}}{dt} \quad , \tag{3.4}$$

where $\frac{dN_{H_2}}{dt}$ is the number of H_2 emanating from the tube per second. The TMP only pumps away the H_2 because any H will recombine at the chamber walls. By combining 3.1 and 3.4, we obtain

$$S = \frac{dV}{dt} = \frac{k_B T}{p}\frac{dN_{H_2}}{dt} \quad , \tag{3.5}$$

The number of H atoms leaving the capillary (assuming a 100% dissociation efficiency) therefore is

$$\frac{dN_H}{dt} = 2 \times \frac{dN_{H_2}}{dt} = \frac{Sp}{k_B T} \approx 2.4 \times 10^{15} s^{-1} \quad , \tag{3.6}$$

The hydrogen flux j_H is defined as:

$$j_H = \frac{1}{A}\frac{dN_H}{dt} \quad , \tag{3.7}$$

where A is the area over which are the H-atoms spread out on the target.

The result in 3.6 gives an approximate number of atoms leaving the orifice of the tungsten capillary. In reality, however, we expect the effective number of atoms leaving the H-cracker to be lower. The reason for this is that the cooling shroud blocks some of the atomic H because the capillary is not perfectly aligned with the aperture of the cooling shroud. More thorough approaches to the calibration of the atomic hydrogen dose and the fraction of dissociated H_2 were elaborated elsewhere [61–63].

To determine the real amount of atomic H deposited on the substrate, we calibrated the dose experimentally by deposition on Si(100). This approach was used by Oura [64,

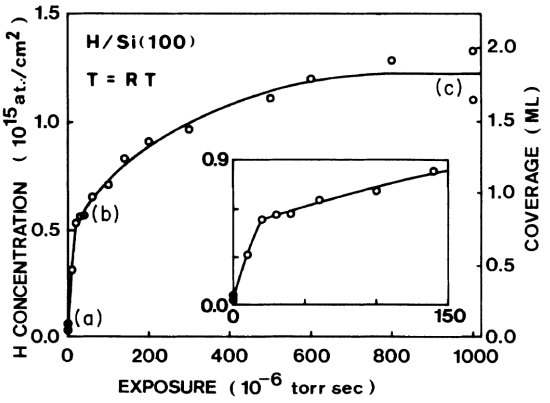

Figure 3.4 | The dependence of the coverage of Si(100) by atomic H on the H_2 dose. The inset portrays a detail from the plot for a very low exposure to show the linear increase in coverage. Adapted from [65].

65]. Figure 3.4 summarizes the results of measurements of the H-coverage on Si(100). The deposition of H_2 was performed by filling the chamber with H_2 and placing a tungsten filament in front of the Si(100) sample. This approach leads to cracking of H_2, which then flies in all directions and some of it falls onto the Si(100) surface. This approach is therefore not as effective as ours, where we have a collimated H-beam, but still shows the relation of the H-coverage on the H_2 dose. In other words, it shows the dependence of the sticking coefficient s on the H-coverage of the Si(100).

In the Figure 3.4, we can observe a linear increase of the H-coverage with the H_2-dose up to approximately 20 L of H_2; we assume that the sticking coefficient in this regime is $s \approx 1$. Above the 20 L dose, the sticking coefficient decreases with increasing coverage, as can be clearly seen from Figure 3.4. The dose required for the saturation of the Si(100) surface was approximately 1000 L. We must note that we used LEED to estimate the coverage by looking at the disappearance of the (2×1)reconstruction, which is not a very precise quantitative measurement. When we assume a similar behaviour for the change of the sticking coefficient also for our home-built H cracker, we can compare the dose necessary for the H saturation for our system and from this calculate the effective dose of our H cracker on the Si(100). The surface of Si(100) is in our case saturated after depositing ≈30 L in 10^{-6} mbar H_2, i.e. ≈ 30 L of H_2 leads to 2 ML H coverage. This means that we need ≈1.3 L H for a 0.75 ML coverage, which is

at the limit of the linear increase of the coverage s. The 0.75 ML coverage corresponds to 5×10^{14} cm^{-2}, and if we recalculate the coverage back to our dose at 10^{-6} mbar H_2, we deposit with our H-cracker approximately 4×10^{14} cm^{-2}s^{-1}. If we further assume that the area A over which our well-collimated H beam [61] spreads out from the capillary at the distance of the sample (3 cm) is approx. 3 cm^2, the number of H atoms leaving the capillary is (according to Equation 3.7) 1/2 of the speed calculated in Equation 3.6.

In this section, we showed that we successfully built and calibrated a H-cracker, which will be used in this thesis. We showed experimentally by QMS that we use the H-cracker at its highest efficiency and the power required for dissociating the H_2 molecules increases with the pressure in agreement with [61]. The theoretical prediction of the H-dose is twice larger than the H-dose measured experimentally on a Si(100). For the experiments on diamond and silicon in chapters 5 and 6, we are going to use the dose experimentally verified on Si(100).

3.2 The RT-STM system

The scanning tunneling microscopy (STM) measurements were performed in a room-temperature scanning tunneling microscopy (RT-STM) UHV system, which comprises a preparation and an analysis chamber shown in Figure 3.5. The chambers are connected by a transfer line with a magnetic transfer arm and separated by a gate valve. The preparation chamber is equipped with the e-beam EFM3T and EFM3 (Focus) evaporators, an Inficon QCM, QMS (Hiden HAL) and a sputter gun (VG EX05 with a scanning unit). The preparation chamber is pumped by a Pfeiffer HiPace 700 TMP backed by a rotary vane pump to achieve a base pressure below 10^{-10} mbar as measured by a Penning gauge. The analysis chamber is equipped with STM (Omicron μ-STM), LEED (VSI erLEED), x-ray photoelectron spectroscopy (XPS, Al and Mg anode X-ray source VG XR3E2 and SPECS Phoibos 100 electron analyzer), LEIS (Specs IQE 12/38 ion source, same analyzer as XPS), AES (Perkin Elmer) and QMS (Balzers

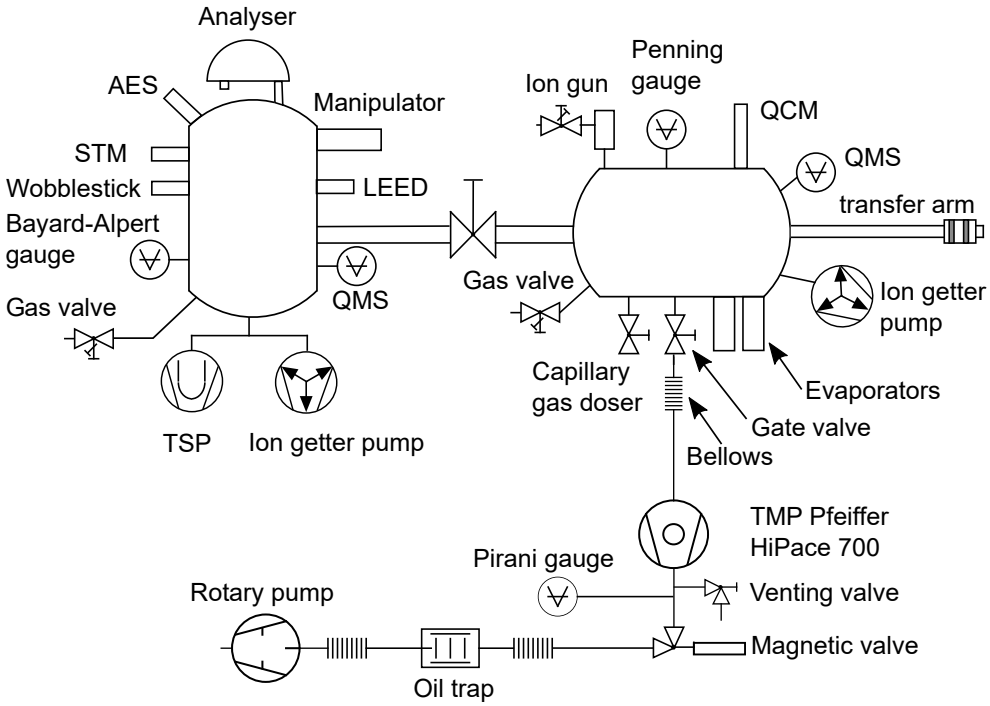

Figure 3.5 | Schematic view of the RT-STM setup, which consist of two UHV vessels. Adapted from [66].

QMG 125). The vacuum in the analysis chamber is maintained by an ion pump and a LN_2-cooled TSP and the base pressure (without cooling and TSP operation) is 7×10^{-11} mbar, as measured by a Bayard-Alpert ion gauge. The samples within the analysis chamber are transferred by a wobblestick. Samples are mounted on an Omicron sample plate and can be inserted by a magnetic transfer arm via a loadlock pumped initially by the rotary vane pump and then by a LN_2-cooled cryogenic pump (cryocan). More details on the RT-STM system can be found in [66].

3.3 The SPECS system

The SPECS system consists of four UHV chambers: preparation, analysis, transfer and PLD chamber and its setup is shown in Figure 3.6. The preparation chamber is equipped with an Ar^+ gun, electron beam annealing, QCM, leak valves for gas dosing, metal evaporators, and a load lock. The evaporators are EFM 3 (FOCUS GmbH) and an effusion cell (LTC-40-10-284-WK-SHM, CreaTec Fischer & Co. GmbH). The base

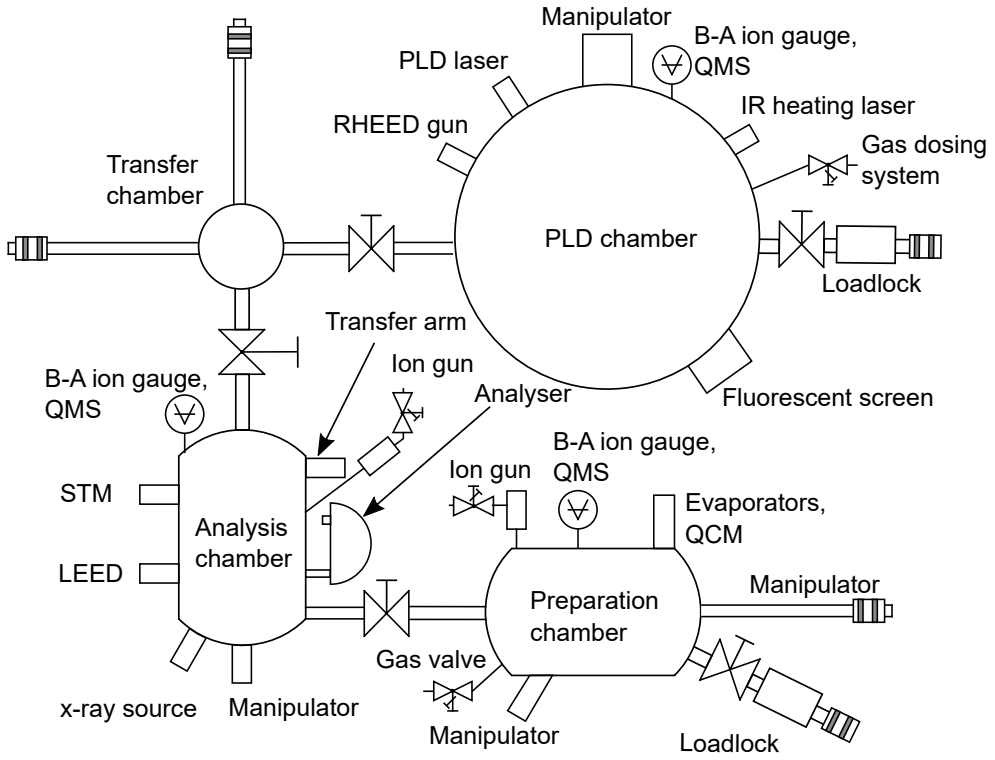

Figure 3.6 | Schematic view of the SPECS setup. The position of the PLD chamber is horizontally flipped around the transfer chamber.

pressure of the preparation chamber was below 4×10^{-10} mbar.

The analysis chamber is equipped with LEED (Omicron SPECTALEED), LEIS (SPECS IQE 12/38 ion source with Wien filter), QMS (SRS100), a SPECS Aarhus 150 STM operated at room temperature and an XPS. The XPS is a commercial setup with an X-ray source (Omicron DAR400) with dual anode to produce Al and Mg K_α radiation (300 W, 15 keV), and a hemispherical energy analyzer (HSA; SPECS Phoibos100). The base pressure of the analysis chamber was below 10^{-10} mbar.

The PLD chamber with a base pressure below 4×10^{-10} mbar is connected via a transfer chamber (base pressure below 10^{-10} mbar) to the surface analysis system described above. Pulsed UV laser light (248 nm laser COMPexPro 205F from Coherent) is passing through an attenuator module (Coherent MicroLas), which allows setting the UV pulse energy. The samples in the PLD chamber were annealed by shining an infra-red laser (DILAS compact evolution; wavelength 980 nm, 50 W for $\approx$ 1000°C) through the hole in the sample plate onto the backside of the sample and the temper-

ature was monitored by an IR pyrometer from the front side. The PLD chamber is equipped with a differentially pumped RHEED system from Staib Instruments GmbH (TorrRHEED^{TM}), which allows monitoring RHEED oscillations in up to 1 mbar oxygen pressure. The RHEED pattern and the intensity of the specular spot are recorded from a phosphor screen with a kSA400 acquisition system (camera integration time 16 ms). There is a sample-storage system in the transfer chamber and the transfer between the chambers is done via magnetically coupled transfer rods. For technical details of the deposition in the PLD chamber, please refer to Section 7.2, Table 7.1 and [51].

3.4 Focused Ion Beam and Scanning Electron Microscope

The nanofabrication and a preliminary nanocharacterization of the metastable films was performed on LYRA3 system (Tescan), which is a combined focused ion beam and scanning electron microscope (FIB/SEM) system. The pressure during the measurement and the ion bombardment was 10^{-7} mbar. The typical parameters for the nanopatterning by the Ga^{+} FIB were 30 keV electron energy with a spot size of 20 nm and a beam current of 40 pA.

In the current work, we varied the irradiation dose and scanning sequence between individual areas and then measured the resulting patterns by the SEM, the Kerr microscope and the micro-Kerr magnetometer (the latter two are briefly described in Section 2.3).

Chapter 4

Metastable Films on Copper

This chapter describes the deposition and transformation of the metastable films on Cu(100) single crystal. We published the results from the growth of $Fe_{78}Ni_{22}$/Cu(100) in *Appl. Phys. Lett.* **103**, 262405 (2013) [32]. The transformation by FIB was published in *APL Materials* **6**, 060701 (2018) [40].

4.1 Introduction

The growth of the metastable films on Cu(100) single crystals is a model system for the investigation of the metastable films, and it is a starting point for the investigation of the growth on Si(100) and C(100) in chapters 5 and 6, respectively. It was shown in Section 1.3 that it is possible to grow metastable Fe films by alloying with Ni, while depositing at a well-defined background pressure [27, 30, 32, 33, 40]. The experimental results from depositions of Fe_xNi_{1-x} with a low Ni concentration at different chamber backpressures were summarized in Figure 1.1(b). The chamber backpressure during these experiments consisted mainly of CO, which is produced in the evaporator, as confirmed by QMS. We can see that the metastable region [dashed red line in Figure 1.1(b)] is somewhat delicate to achieve and well-defined deposition parameters are necessary for reproducible preparation of the metastable $Fe_{78}Ni_{22}$ films.

W. Rupp [22, 26] and S. Shah Zaman [30, 31] studied applications of the pure Fe metastable films. They transformed the 8-ML-thick (1.4 nm) Fe/Cu(100) and showed that it is possible to fabricate ferromagnetic (FM) nanostructures by irradiation with an ion beam. The fabrication of the FM nanostructures in the metastable $Fe_{78}Ni_{22}$/Cu(100) has been only briefly addressed in [33]. The effect of the irradiation therefore remains open and it is intriguing to investigate the fabrication of the FM nanostructures by the FIB. Similarly, the effect of ion type and energy has not yet been addressed for the Ni-stabilized metastable films.

Based on the phase diagrams in Figure 1.1(b) and additional experiments in the Master thesis [33], we performed a series of depositions of an $Fe_{78}Ni_{22}$ alloy in 5×10^{-10} mbar CO backpressure on multiple Cu(100) substrates by which we confirmed the reproducibility in the preparation of the metastable films. From now on, we are going to describe the $Fe_{78}Ni_{22}$ films deposited at a well-defined partial pressure of CO as the metastable films, and we show in this chapter that it is possible to tune their magnetic saturation and magneto-crystalline anisotropy by the FIB. Finally, we compare the different ion types and energies used for the ion-beam-induced transformation and discuss their effect on the transformation efficiency.

4.2 Preparation of the Cu(100) surface

We used sputter-anneal cycles for the crystal preparation. For removing a previously deposited layer, the first sputtering (2 keV at $\approx 10^{13} Ar^+ cm^{-2} s^{-1}$) took approx. 40 minutes, until the whole 8-nm-thick layer was sputtered off, and it was followed by twice 10-min sputtering. The annealing (T=520 °C) took 10 min after each sputtering and a resulting surface was clean of any contamination (red line in Figure 4.1) and had the fcc(100) diffraction pattern. An out-of-the-box Cu crystal usually required a few sputter-anneal cycles. A summary of the samples used in the experiments in this chapter is in Appendix A.1.

Some of the Cu crystals did not have the 99.999% purity claimed by the producer

and they were heavily contaminated by sulphur, which segregates from the bulk Cu at 480 °C. Sulphur then forms small islands and leads to step-pinning and bunching. We observed in scanning electron microscope (SEM) after focused ion beam irradiation (FIB) that such defects lead to an easier fcc-to-bcc transformation, i.e., bcc nuclei occur preferentially at the S-islands. This was the reason why the sulphur-contaminated crystals Cu#7 and Cu#8 do not appear in Table A.1 and were replaced by Cu#9 and Cu#10.

4.3 Growth of the metastable films

As already mentioned in the introduction, we fixed the deposition parameters to have reproducible and well-defined growth conditions. The typical deposition parameters were 44 ML (8 nm) $Fe_{78}Ni_{22}$ in 5×10^{-10} mbar CO on Cu(100) and the depositions were performed by an e-beam evaporator EMF3T in PINUP. The cryopanel in PINUP was kept full of liquid nitrogen during deposition and the pressure before deposition was 7×10^{-11} mbar. For more details on the experimental setup, please refer to Section 2.5.

4.3.1 Results

Figure 4.1 shows AES results of a clean Cu(100) and 8 nm $Fe_{78}Ni_{22}$/Cu(100). The prepared Cu crystal does not have any contamination, and the as-deposited $Fe_{78}Ni_{22}$ has both Fe and Ni peaks along with the C and O peaks arising from the dissociation of CO on the Fe. The typical concentrations calculated from sensitivity factors [43] of the elements in the topmost layers of the metastable films measured by AES were 74at% Fe, 14at% Ni, 7.5at% C, and 4.5at% O.

The structure and magnetic properties of the as-deposited and irradiated films were investigated by LEED and SMOKE, respectively; the data is shown in Figure 4.2. The as-deposited films were paramagnetic [longitudinal SMOKE measurement marked by blue line in Figure 4.2(a)], and after irradiation by 4 keV Ar^+ with

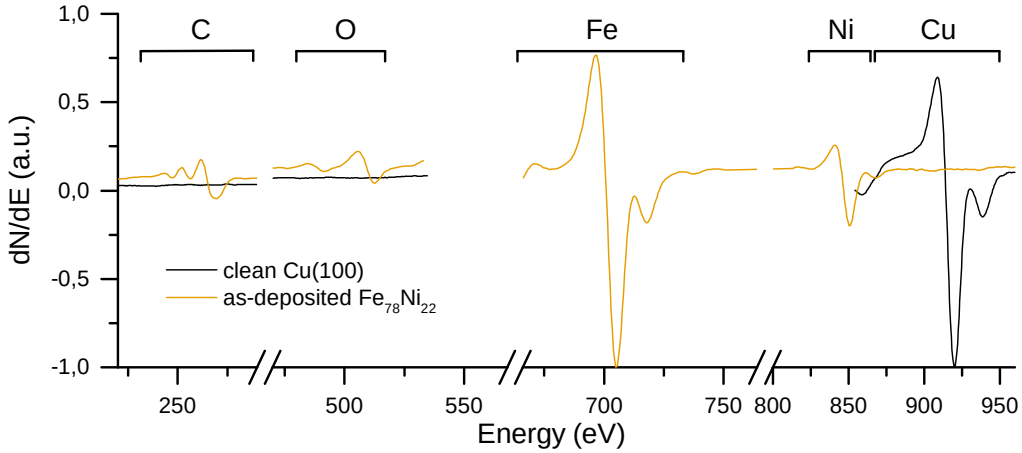

Figure 4.1 | AES before and after $Fe_{78}Ni_{22}$ deposition on Cu(100)#13. The black line corresponds to Cu(100) before deposition. The orange line was measured on 8 nm $Fe_{78}Ni_{22}$/Cu deposited in 5×10^{-10} mbar of CO.

a dose of 2.0×10^{15} cm^{-2}, they were partially transformed (violet line). The $Fe_{78}Ni_{22}$ films were completely transformed into the ferromagnetic phase after an ion dose of 3.5×10^{15} cm^{-2} (orange line). The polar SMOKE measurement did not show any magnetization. The LEED of the as-deposited films in Figure 4.2(b) portrays well-defined fcc (100) diffraction spots with a c(2×2). After irradiation, the spots correspond to elongated, diffused bcc (110) and we could observe a complete removal of the c(2×2) reconstruction.

4.3.2 Discussion

The AES in Figure 4.1 shows that the near-surface composition according to the APPH sensitivity factors (excluding the effect of CO) of the as-deposited Fe-Ni alloy is $\approx Fe_{81}Ni_{19}$, i.e., not precisely $Fe_{78}Ni_{22}$. We attribute this error in stoichiometry to the low precision of the AES measurement. According to the vapour pressure, Fe evaporates faster than Ni at a given temperature [see Figure 4.3]. This should cause the Ni content in the evaporation rod to rise so that in equilibrium the ratio of the atoms leaving the evaporator corresponds to the concentration of the evaporation material ($Fe_{78}Ni_{22}$ evaporation rod). We also observed that the speed of the deposition will affect the amount of CO dissociated; the slower the deposition, the higher the C

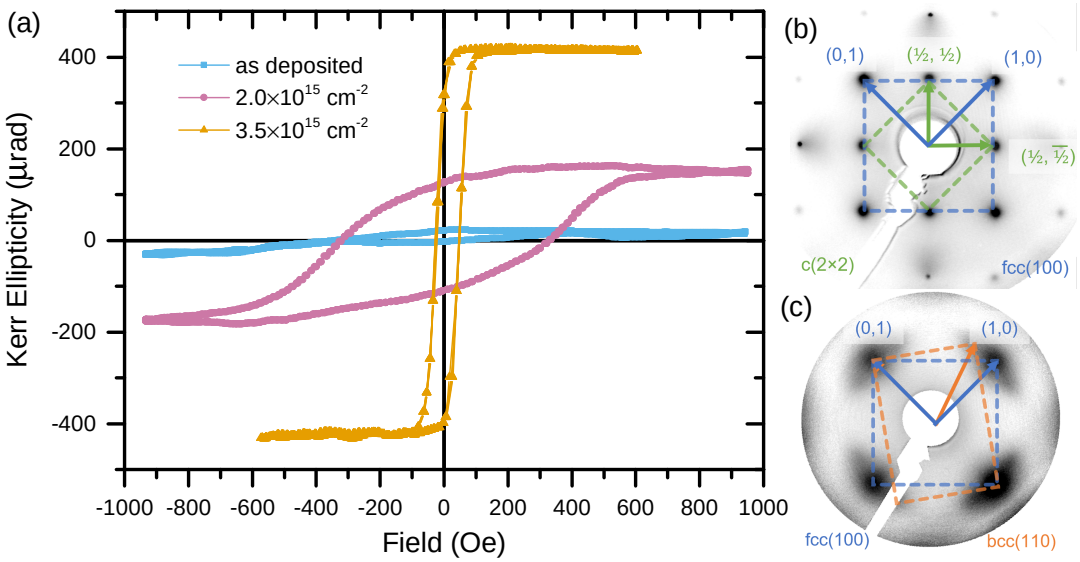

Figure 4.2 | Analysis of as-deposited and irradiated $Fe_{78}Ni_{22}$/Cu(100). (a) The blue line in SMOKE shows signal from a paramagnetic as-deposited film. The line is not perfectly straight because of an artefact of the measurement. The film is partially transformed after irradiation by 4 keV Ar^+ with an ion dose of 2.0×10^{15} cm^{-2} (violet line) and the orange line shows a hysteresis loop of a film completely transformed by an ion dose of 3.5×10^{15} cm^{-2}. This experiment was performed on Cu(100)#17. (b) The LEED at 130 eV of the as-deposited films shows the fcc(100) structure (blue sqare) with a c(2×2) reconstruction (green square). (c) The diffraction spots (LEED at 120 eV) on a completely transformed film are blurred and consist of four bcc(110) domains. One of these is shown by the orange rectangle. The LEED images are from experiments on Cu(100)#3.

and O contents because of a longer exposure.

The SMOKE measurement in Figure 4.2(a) served only to confirm that the films are transformable and it will be discussed in more detail in the following section. We performed a low-temperature experiment on the as-deposited metastable films, in which we observed a hysteresis loop appearing below ≈140 K. We attribute this to the pinning of small bcc ferromagnetic domains, which can grow spontaneously on defective sites of the Cu(100) substrate.

The fcc spots in LEED of the as-deposited film [Figure 4.2(b)] are sharp, because the electrons undergo diffraction on a flat film, whereas the bcc spots [Figure 4.2(c)] are blurred because the film consists of multiple, randomly oriented bcc needles [32]. The bcc needles are randomly oriented in both the azimuthal and polar directions. The diffraction spots measured on the transformed film correspond to the four bcc(110) domains, which means that the randomly oriented bcc needles measured by STM in [32] consist of four bcc domains rotated by ≈ 10°. In the following section we will see that FIB allows for control of the bcc needles' atomic ordering and thus the tuning of the easy axis of the transformed areas.

The metastable region is not perfectly defined by the dashed red line in Figure 1.1(b) because further investigations revealed that the stabilizing effect of CO decreases with an increasing Ni content. Experiments with varied CO backpressure and O-poisoning in [33] showed that the effect of CO decreases with increasing Ni content. In particular,

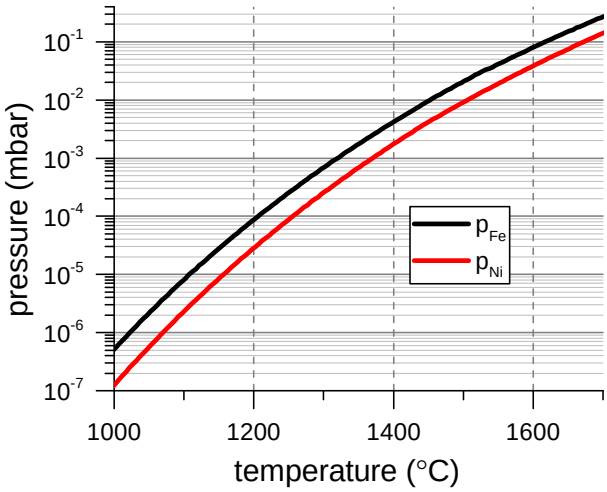

Figure 4.3 | Vapour pressure of Fe and Ni. The Fe vapour pressure is approx. 5× higher than the vapour pressure of Ni, which leads to a higher deposition speed at a constant concentration and temperature.

CO could completely stabilize a film deposited from a $Fe_{85}Ni_{15}$ evaporation rod, but the effect on stabilization of the film was lower for a film deposited from a $Fe_{78}Ni_{22}$ evaporation rod. The change in the stability of the metastable films resulted in a lower magnetic saturation and higher coercive field at the same irradiation dose for the more stable films (i.e. for films deposited in higher CO pressure and with higher Ni concentration), as shown in [33].

4.4 Ion-beam induced transformation

In this section, we show and discuss results from the article by Urbanek et al. [40] with an emphasis on the easy axis modification, which is defined by the atomic structure after ion-beam-induced transformation. We further connect the ion type and energy with the transformation efficiency.

We describe here two sets of measurements. The first one is a dose test on $6\times14\ \mu m^2$ rectangles fabricated by either a single high-dose scan or 100 low-dose scans. The second set of measurements was performed on circles with a $10\ \mu m$ diameter with a varying FIB-scanning angle with a 10° step. The ion dose was set to the dose necessary for a complete transformation in a single scan. The patterning and SEM characterization were performed by the FIB-SEM setup LYRA3, and the MOKE easy-axis measurement was performed by home-built MIRANDA Kerr microscope; these techniques are described in Section 3.4.

4.4.1 Nanopatterning and anisotropy modification

Figure 4.4 shows the results of the two different dose tests. The first one is the irradiation with 100 low-dose scans, where the red curve in Figure 4.4(a) marks the change in Kerr ellipticity with the ion dose. Figure 4.4(b) contains SEM of the irradiated areas corresponding to doses I, II and III in (a).

The Kerr ellipticity in (a) shows a small increase in the magnetization up to a dose of $4 \times 10^{15}\ cm^{-2}$, above which the ion beam transforms the film very efficiently

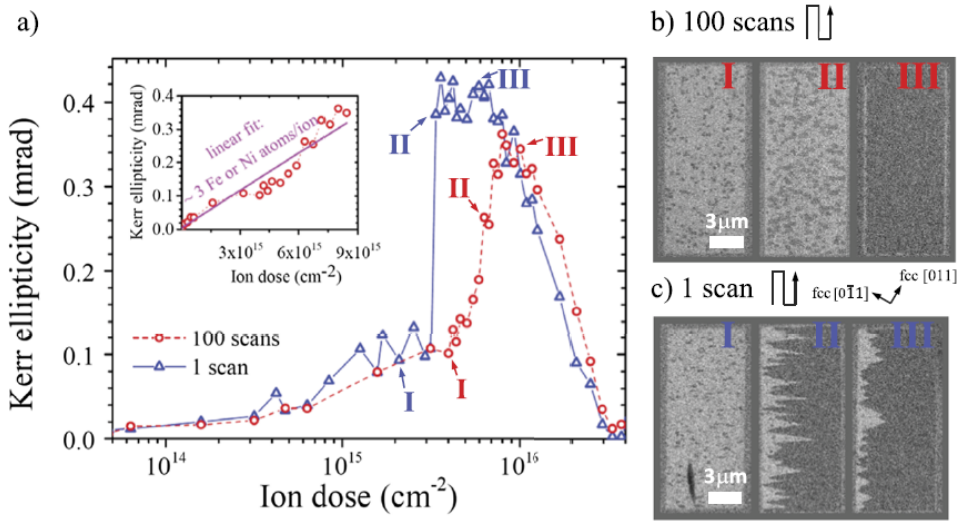

Figure 4.4 | MOKE and SEM analysis of 8 nm $Fe_{78}Ni_{22}$/Cu(100)#10 upon irradiation by 30 keV Ga^+ ions. (a) Dependence of the normalized saturation magnetization on the ion dose of two FIB scanning strategies: a single scan (blue) and 100 scans (red) with the same total irradiation dose. The inset shows the initial part of the transformation indicating an almost constant transformation efficiency with respect to the ion dose. (b) Evolution of the transformation in rectangles irradiated by multiple scans. (c) Evolution of the transformation in rectangles irradiated by a single scan. The numbers I, II, and III in (b) and (c) represent the corresponding points on the curves shown in plot (a). The contrast in (b) and (c) changed from grey (as-deposited film) to light-grey (irradiated but untransformed film) and finally to dark-grey (transformed film). The experiments were performed by L. Flajsman and V. Krizakova at CEITEC [40, 67].

with an approximate transformation efficiency of 3 atoms per incoming Ga^+ ion [see inset in Figure 4.4(a)]. Above a dose 10^{16} cm^{-2}, the Kerr ellipticity starts to decrease because of sputtering and intermixing with the Cu substrate of the $Fe_{78}Ni_{22}$ film. This approach to ion-beam induced transformation is similar to the one we used in the in-situ experiments, where we scanned the metastable films with 4 keV Ar^+ from the SPECS ion gun. Figure 4.4(b) in the first rectangle (I) shows an irradiated film (light-grey) with some transformed areas (dark-grey dots) surrounded by (grey) fcc metastable film. Increase in ion dose leads to an increase in the size of the dark bcc areas (II). The film is then in III completely transformed. We can see that the fcc-to-bcc transformation after the 100 low-dose scans exhibits a stochastic transformation process, because the complete transformation in (b) occurs randomly over the whole irradiated area.

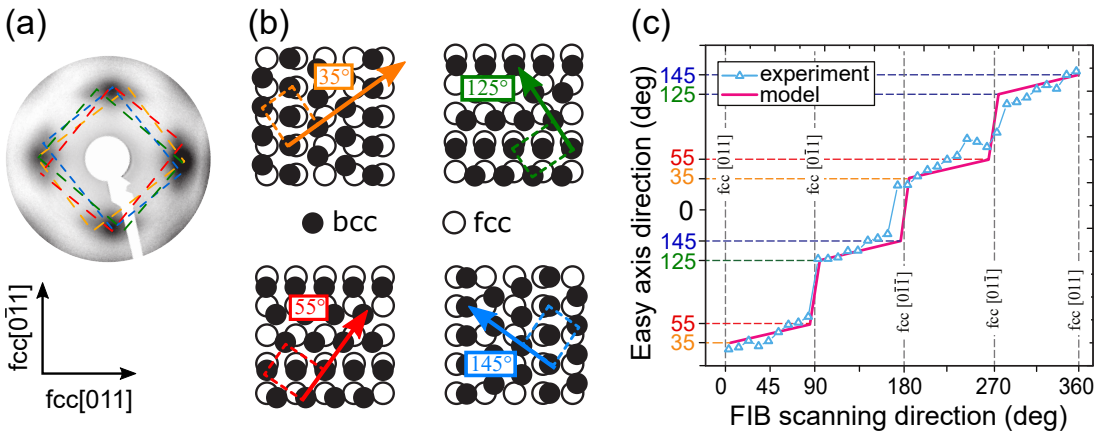

Figure 4.5 | Easy-axis direction change of completely transformed 8 nm $Fe_{78}Ni_{22}$/Cu(100) by FIB. (a) LEED at 120 eV of a metastable film completely transformed by an ion beam. (b) The LEED pattern consists of four bcc domains, of which the first is rotated by 35 ° with respect to the fcc[011]. (c) The easy-axis direction of the magnetic anisotropy changes as a function of the FIB scanning direction. The figure was adapted from [40].

The Kerr ellipticity evolves in a similar fashion in the single-scan experiment up to a dose of 3×10^{15} cm^{-2} [blue line in Figure 4.4(a)]. This is a threshold, above which the partially transformed film transforms almost completely into bcc, shown by the abrupt increase of the Kerr ellipticity. Similar to the low-dose experiment, the Kerr ellipticity then starts to decrease with ion dose above 8×10^{15} cm^{-2}. The data in (c) show that the bcc areas in the single scan grow from the bcc nuclei fabricated by the ion beam as it scans over the surface. However, for a steady migration of the bcc transformation, a critical dose is necessary. The critical ion dose of 4×10^{15} cm^{-2} is therefore needed for a steady migration of the bcc transformation front. The steady-state bcc boundary migration makes the single-scan transformation more efficient and leads to fabrication of magnetic patterns with a low number of bcc domains.

In the second set of experiments portrayed in Figure 4.5, we measured the change of the easy axis direction with respect to the FIB-scanning direction in the single-scan approach. The LEED pattern in Figure 4.5(a) shows that there are four bcc domains in a $Fe_{78}Ni_{22}$ film transformed by a broad Ar^+ ion beam [see Figure 4.2(c)], which correspond to four orientations of the bcc unit cell with respect to the fcc substrate/epitaxial film. These domains are rotated by approx. ±10° with respect to the [001] and [0$\bar{1}$0] crystallographic directions of the fcc substrate, as shown in Figure 4.5(b). Finally, (c)

shows the easy-axis-orientation dependence on the FIB scanning direction. We can see that there is a preferential orientation of the easy axis orientation depending on the FIB scanning direction and the easy axis jumps at 90°, 180° and 270°. The change of easy axis is connected to the change in the crystallographic orientation of the bcc domains. The experimental data (blue triangles) fit to the model (red line) where FIB scanning preferentially forms bcc domains which have [001] direction parallel to the scanning direction. The domain formation shown in Figure 4.4 therefore enables the growth of large bcc grains with a well-defined two-fold (uniaxial) magneto-crystalline anisotropy.

We could not observe this behavior in the *in-situ* experiments performed with the broad Ar^+ ion beam. The irradiation by the broad Ar^+ ion beam corresponds to the red curve in Figure 4.4, i.e., the result of the irradiation by the broad beam are many small bcc domains with no measurable magneto-crystalline anisotropy. Magneto-crystalline tuning of the easy axis is, therefore, not possible when we irradiate the metastable film multiple times over the whole area.

4.4.2 Comparison of ion type and energy

When we compare the transformation by the broad Ar^+ ion beam and the 100 low-dose scans of the Ga^+ FIB, the transformation performed by 4 keV Ar^+ in Figure 4.2(a) qualitatively shows the same behavior as the transformation by 30 keV Ga^+ ions in Figure 4.4. However, the ion dose necessary for a complete transformation is higher for the Ga^+ ions (see Table 4.1). We compared our measurements with the transformation of $Fe_{78}Ni_{22}$/Cu(100) by 2 keV Ar^+ in [32] and on CO-stabilized Fe/Cu(100) in [30]. The summary of the data is in Table 4.1.

To understand the change of the transformation dose with ion type and energy, we have performed Monte Carlo simulations using the stopping and range of ions in matter (SRIM) [58]. Calculations for the Ar^+ and Ga^+ ions used for the transformation are shown in Figures 4.6 and 4.7.

The magenta lines in Figure 4.6(a-c) show that 100% of the 2 keV Ar^+ , 98% of the

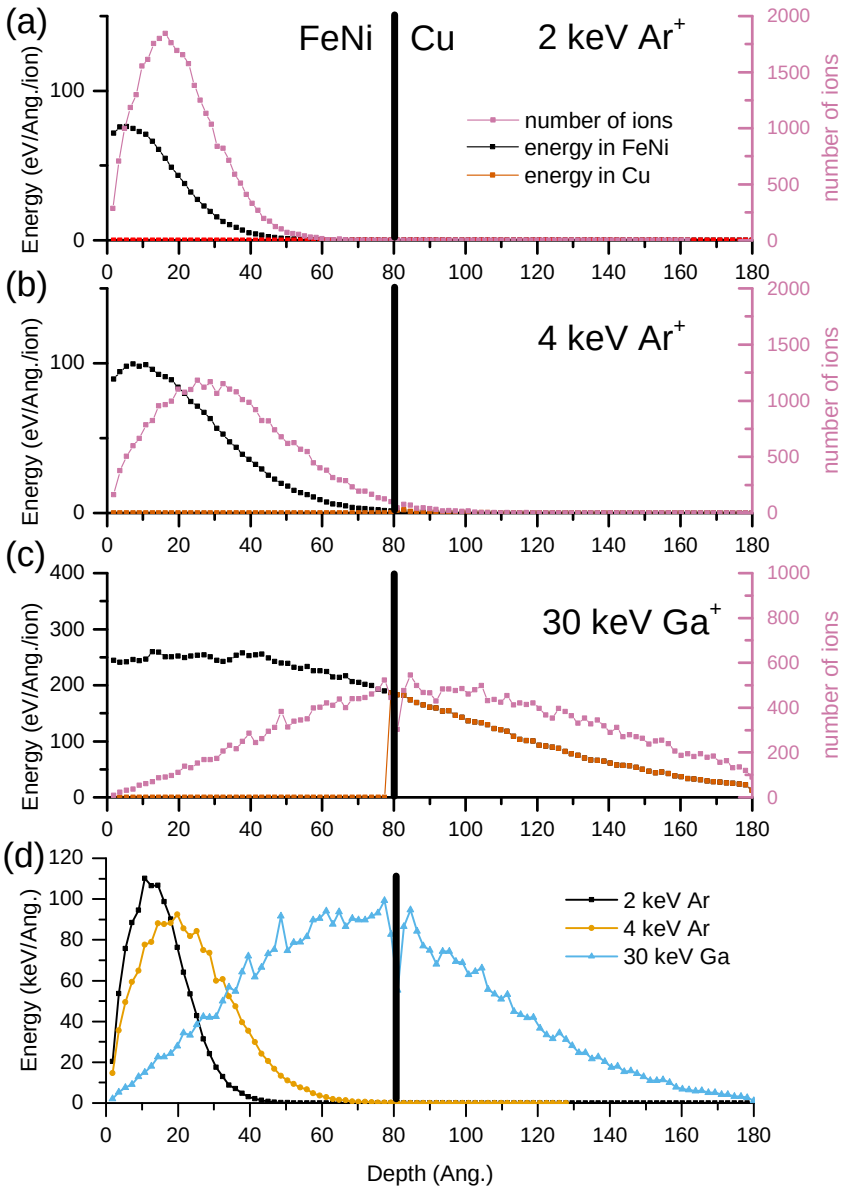

Figure 4.6 | SRIM calculations of ion penetration depth (number of ions) and energy deposition into 8 nm $Fe_{78}Ni_{22}$/Cu. (a) at 2 keV, the ions stop in the topmost part of the FeNi layer and deposit here most of the energy. (b) 4 keV Ar^+ ions penetrate through the whole metastable film and also to the top layers of the Cu substrate. (c) 30 keV Ga^+ ions penetrate deep into the Cu substrate. (d) combination of the results from (a-c). The results are from the trajectories of 30 000 ions.

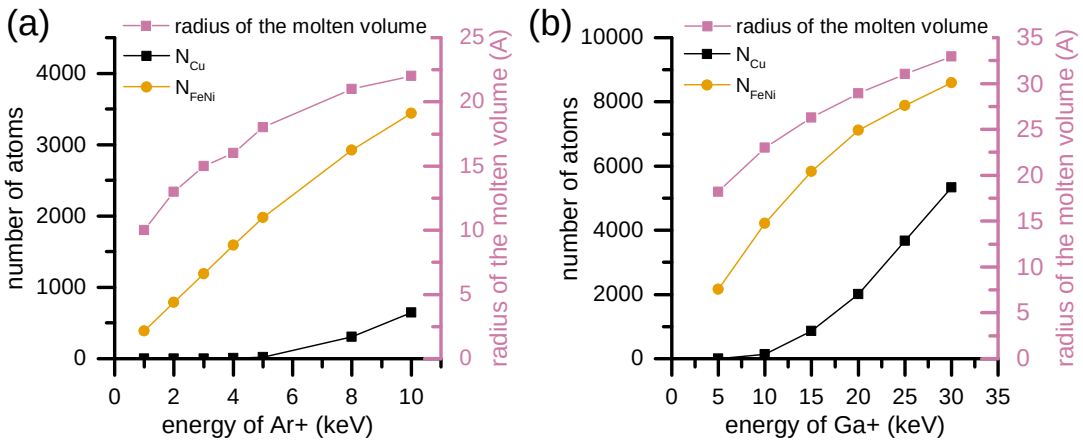

Figure 4.7 | SRIM calculations of the number and type of atoms in the molten volume (y-axis on the left) and the radius of the molten volume (y-axis on the right) in 8 nm $Fe_{78}Ni_{22}$/Cu. (a) dependence on the energy of Ar^+ ions shows that there is not a significant amount of Cu atoms in the molten volume below 6 keV. (b) The intermixing with Cu starts in the case of Ga^+ ions above 10 keV.

sample	thickness nm	ion type	ion energy keV	ion dose 10^{15} cm^{-2}
CO-stabilized Fe[30]	4	Ar	1	0.9
CO-stabilized Fe[30]	4	Ar	2	0.6
CO-stabilized Fe[30]	4	Ar	4	0.9
$Fe_{78}Ni_{22}$[32]	8	Ar	2	6.0
$Fe_{78}Ni_{22}$	8	Ar	4	3.5
$Fe_{78}Ni_{22}$	8	Ga	30	9.0

Table 4.1 | Comparison of ion dose, type and energy used for the complete transformation of the metastable films on Cu(100).

4 keV Ar^+ and 38% of the 30 keV Ga^+ ions remain in the 8 nm $Fe_{78}Ni_{22}$. However, when we consider the energy deposited in the metastable film, the Ar^+ deposits 2 and 4 keV/ion [integral of the black line in Figure 4.6 (a) and (b) respectively], but 30 keV Ga^+ deposits 20 keV/ion [integral of the black line in Figure 4.6(c)] in the $Fe_{78}Ni_{22}$ film, and the rest in the Cu below. The combination of the plots in Figure 4.6(a-c) shown in (d) describes the energy distribution per thickness in the $Fe_{78}Ni_{22}$ film. The 2 keV Ar^+ ions deposit most of the energy in the topmost 1/4 of the film (black line), whereas the 4 keV Ar^+ ions spread the energy down to 1/2 of the film (yellow line). The 30 keV Ga^+ with larger mass and energy penetrate deep into the substrate of the metastable film but they still deposit considerably more energy into the film than the low-energy and lighter Ar^+, which do not even penetrate through the whole film. The Ga^+ ions, however, deposit a significant amount of the energy at the $Fe_{78}Ni_{22}$-Cu interface.

Figure 4.7 describes the size of the molten volume along with the number of atoms in the molten volume for Ar^+ and Ga^+ ions at different energies. In this calculation, we assumed that the molten volume is a sphere, even though it is probably statistically distributed at the core of the collision cascade. The intermixing of the metastable films with Cu can stabilize the fcc phase because of the fcc nature of Cu. The black line in (a) shows that the number of Cu atoms in the molten volume is negligible until the Ar^+ energy exceeds 6 keV. At this energy, the radius of the molten volume is around 20 Å, which corresponds to approx. 1/4 of the metastable film's height. We can see that in the case of the 2 and 4 keV, which we used for the broad-beam *in-situ* transformation, the intermixing at the FeNi-Cu interface is negligible.

The behaviour at low energies is similar in the case of Ga^+ irradiation, but for the 30 keV Ga^+ energy we used in the FIB experiments, the Cu atoms attribute to approximately 1/3 of the molten volume [black line in figure 4.7(b)]. The radius of the molten volume at 30 keV [magenta line in figure 4.7(b)] is 33 Å, which means that nearly a half of the metastable layer might be intermixed with the underlying Cu buffer layer. We assume that this then leads to a decrease in the magnetic saturation

of the transformed films.

Based on Figures 4.6 and 4.7, we assume that the ion type and energy determine the efficiency of the ion-beam induced transformation by defining where and how much energy is deposited in the target material. In other words, the difference in the ion dose necessary for the transformation of the metastable films is connected to the higher cross section for creation of recoils with sufficient energy to locally melt the metastable film. The consequences can be illustrated on the system of CO-stabilized Fe/Cu(100) summarized in the Table 4.1. In case that the energy deposited in the metastable film is too low, the transformation has lower efficiency and therefore a larger ion dose is necessary for the ion-beam induced transformation. This is the case for 1 keV Ar^+ irradiation of the 4-nm thick CO-stabilized Fe/Cu(100) and for 2 keV Ar^+ irradiation of the 8-nm $Fe_{78}Ni_{22}$/Cu(100). In case that the ions deposit more energy at the Fe-Cu interface, the ions causing the intermixing at the interface do not contribute to the transformation of the film and the ion dose necessary for the transformation is higher. This is the case for 4 keV Ar^+ irradiation of the 4-nm thick CO-stabilized Fe/Cu(100) and for 30 keV Ga^+ irradiation of the 8-nm $Fe_{78}Ni_{22}$/Cu(100). The ideal case appears to be when the ions deposit most of their energy in the centre of the metastable film, which is the case for the remaining two films in Table 4.1.

4.5 Conclusion

We presented an experimental road to obtaining the Ni-and-CO-stabilized, metastable, paramagnetic fcc γ-Fe films transformable to the ferromagnetic bcc α-Fe phase by ion-beam irradiation. We defined the deposition parameters for a reproducible preparation of the films and showed how different ion energies, types, and scanning procedures change the properties of the irradiated areas. We showed that it is possible to tune the magneto-crystalline anisotropy of the ferromagnetic nanostructures by the direction of the FIB scanning. The dependence of the easy-axis orientation of the ferromagnetic nanostructures warrants further investigations. Possible explanation

might lie in the strain induced by ion implantation and defects (e.g. Ga interstitials). The SRIM analysis of the energy deposited by the ion-beam leads to the conclusion that using a lower energy for the FIB transformation by Ga^+ ions (e.g. 20 keV instead of 30 keV) should lead to a higher transformation efficiency.

In outlook, the tuning of the deposition parameters seems to be essential for the stabilization of the metastable films, and the possibility to tune the magnetic saturation. The change of the deposition parameters might also affect the possibility of tuning the magneto-crystalline anisotropy in the metastable films by FIB. It would, therefore, be interesting to try depositions of $Fe_{78}Ni_{22}$ in different CO pressures and then transform them by FIB. The different CO pressure might allow/prohibit the tuning of the magneto-crystalline anisotropy by FIB. Similarly, it might be possible that there is a dependence of the anisotropy on the Ni content. The reason for this is that both the C and Ni might block the propagation of the bcc needles and therefore too much of both can destroy the possibility to tune the magneto-crystalline anisotropy before disabling the transformation.

Applications of the metastable films might require their use at higher temperatures. It would therefore be intriguing to measure the effect of heating on the intermixing at the $Fe_{78}Ni_{22}$-Cu interface or on the decrease of magnetic saturation and anisotropy.

It might as well be possible to use the SPECS sputter source in PINUP to induce the growth in the preferential direction, as in FIB. To do this, one would have to tune the dose to be sufficiently large and rotate the crystal (or the scanning direction) to be aligned in the correct direction. However, the effect of the larger beam size of the SPECS ion gun would have to be checked by de-focusing the FIB. When combined with low-energy electron microscope at CEITEC, observing diffraction on the different bcc domains would allow a better understanding of the direction-specific transformation.

Chapter 5

Metastable Films on Silicon

In this chapter, we show that it is possible to substitute the Cu(100) single crystal by a more technologically interesting substrate, silicon, and it is based on an article published in *Applied Surface Science* **469** (2019) 747–752 [41], and contains additional information not available in the publication.

5.1 Introduction

Silicon has been the most commonly used material in the semiconductor industry and scientific research for decades, not only for its electronic properties but also because processes for the preparation of very well defined substrates with almost perfect crystallographic properties have been established. Our experiments described below indicate that the Fe does not grow epitaxially on Si(100) but it is possible to grow a Cu(100) buffer layer on Si(100) as a seed for the growth of the metastable films [36–38]. The Cu buffer layer grows in the desired (100) crystallographic orientation when the Si(100) surface is unreconstructed, hydrogen-terminated (H-Si), which is most commonly achieved by etching in hydrofluoric acid (HF) [36–38, 68–70]. Multiple studies reported the epitaxial growth of metals on H-Si with a Cu buffer layer [36, 69, 71–73], where the H-Si is degreased and etched in 10% HF. The lattice constants of Cu and unreconstructed Si lead to a lattice mismatch of -40% but change to

-6% for 45° azimuthal rotation between the lattices [with Cu(010) parallel to Si(011)]. The first experimental observation of the epitaxial growth of Cu(100)/H-Si(100) was reported by Chang [36, 68, 74]. Further investigations described the evolution of the microstructure on the Cu-Si interface [75], and AES indicated the presence of Si in the Cu layer up to 10 nm [37]. A scanning tunnelling microscopy (STM) study confirmed that Cu grows on Si(100) in island mode and also described the initial stages of growth, the formation of grains and silicides on the Cu-Si interface [76]. The silicides induce strain on the epitaxial film and thus support the grainy morphology/island growth of the fcc (100) Cu films [37, 69, 75–78]. The morphology of the film improves [i.e., the islands coalesce into relaxed mounds with a (100) texture] with increasing thickness [37] and, e.g., a 130-nm thick films consist of approx. 20-nm-wide well-defined crystallites which have sub-grain boundaries [37, 78, 79].

Even though the most common way of preparation of the H-Si is by etching in the HF, it is also possible to prepare the H-Si by annealing at 1200 °C followed by the deposition of the atomic hydrogen [80, 81]. Baker in 2005 described the initial stages of the Cu growth measured by STM [82]. Apart from this work, we could not find any evidence that it is possible to grow the epitaxial Cu buffer layer on H-Si prepared in the UHV.

It might, therefore, be possible to grow the metastable films on an epitaxial Cu buffer layer on both chemically and UHV-prepared H-Si(100). Multiple studies showed that it is possible to grow epitaxial layers of various materials on Cu/Si(100). For example, Vaz et al. showed that it is possible to use the corrugation of the underlying Cu buffer layer for magnetic modulation of a Co film [71–73, 83]. However, these films have not yet been used for the fabrication of ferromagnetic nanostructures in paramagnetic layers, as might be possible on the metastable films on the Cu/Si(100).

We describe in this chapter the growth of the metastable fcc $Fe_{78}Ni_{22}$ films on the 130 nm thick Cu(100) buffer layer grown on the H-Si substrates prepared both in the UHV and chemically. As already shown in Section 1.2 and Chapter 4, the metastable $Fe_{78}Ni_{22}$/Cu(100) is an excellent system for a one-step fabrication of mag-

netic nanostructures and we performed the transformation to the bcc phase both, in-situ by a weakly focused ion beam and ex-situ by FIB. Measurement of the magnetic properties of transformed thin films and nanostructures performed by the Kerr magnetometry show that the $Fe_{78}Ni_{22}$/Cu(100)/H-Si(100) is a viable alternative to the systems prepared on the Cu(100) single-crystal substrates. This chapter will start with the description of the preparation of the H-Si(100), then the deposition of the Cu-buffer layer and the metastable films. Finally, we are going to present the fabrication of the ferromagnetic nanostructures in a paramagnetic matrix.

5.2 Preparation of the H-terminated Si(100) surface

The experiments were performed on B-doped (p-type) Si(100) substrates with a resistivity of 5-20 Ωcm. The dimensions of the samples were $3 \times 12 \times 0.4\,\mathrm{mm}^3$; the sample numbers and experiments performed are summarized in Appendix A.4. Two different methods were applied for obtaining a H-terminated surface: a chemical and UHV procedures. Only three samples prepared by the chemical procedure are included in Appendix A.4. On the other hand, almost all of the samples treated by the UHV procedure are included in the appendix because most of the results presented here were performed on these samples.

For the chemical method, Si was etched for 2.5 minutes in 10% HF to remove the native oxide and to terminate the Si with hydrogen [70], then rinsed for 1 minute in high-purity (Merck Milli-Q) water, dried with argon gas and transferred into the loadlock connected to the UHV chamber PINUP within 10 minutes after the etching. The H-Si should be inert to the ambient atmosphere for such a period [70]. Then, the sample was outgassed in the UHV chamber at 100 °C for 30 minutes.

In the UHV method, we avoided any ex-situ preparation. We designed and assembled a home-built heating stage for direct current (DC) heating of Si samples (for technical drawings and a description, please refer to Appendix C). Target holders for the DC heating were made of Mo; their design was similar to that of a commercially

available (Omicron) sample plates for the DC heating and can be found in Appendix D. After introducing the sample into the UHV, we outgassed the sample and the sample holder by e-beam heating in the manipulator to 600 °C for approx. 20 h. The sample was then heated by DC in the Si heating stage also to 600 °C for approx. 20 h until the base pressure in the chamber was restored. After the outgassing phase, we annealed the samples repeatedly at 1200 °C by DC for 5 seconds with a 5-second ramp from the outgassing temperature. The highest pressure during the last annealing step was below 5×10^{-10} mbar. With this approach, we were able to completely remove both, the native SiO_2 and any organic impurities. The temperatures were checked by the thermocouple on the manipulator and by the pyrometer described in Section 3.1.

In the last step of the UHV method, we performed the H termination of Si by a home-built H-cracker based on the design of Bischler [62]. The H-cracker is described in the section 3.1 and its design is shown and discussed in Appendix B. The Si samples were exposed to atomic hydrogen (10^{-7} mbar H_2 pressure in the UHV chamber) for 7 mins to achieve a complete 2-ML H termination.

5.2.1 Results

The chemically prepared H-Si(100) samples had a (1×1) diffraction pattern after introduction into the UHV and the annealing at 100 °C, which is shown by a green square in Figure 5.1(a). The unetched, UHV treated Si(100) showed (2×1)-reconstructed domains after annealing to 1200 °C [blue rectangles in Figure 5.1] with blurred streaks between the 1/2-order spots. The reconstruction of the annealed Si changed into a (1×1) after the termination with the atomic H [green square in Figure 5.1(c)]. The change in reconstruction confirms that the atomic H had saturated all the Si dangling bonds [64, 80]. The low-index diffraction spots of the UHV-prepared H-Si are brighter than the diffraction spots on the chemically prepared sample.

The AES measurement shows that impurities cover the HF-etched surface after annealing at 100 °C; quantification of the Auger peaks indicates concentrations of roughly 15% C and 2% O (blue lines in Figure 5.2). The outgassed Si with a native SiO_2

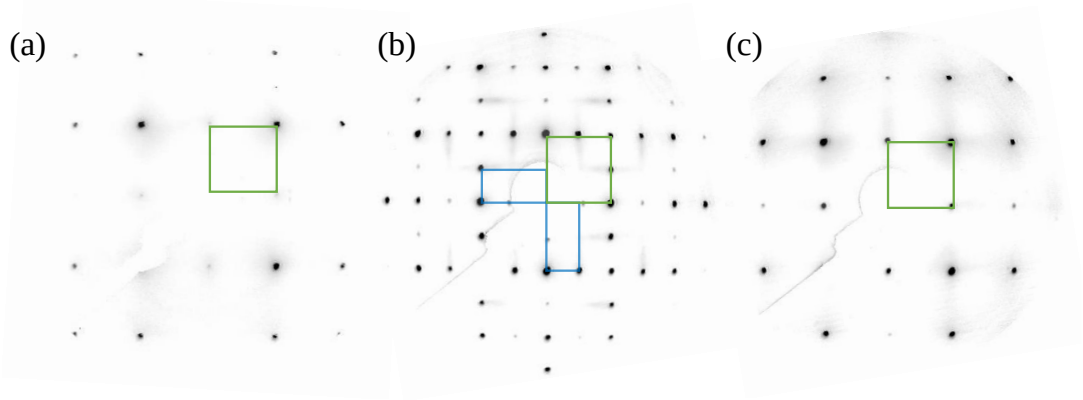

Figure 5.1 | LEED of Si(100) at 120 eV treated chemically and in UHV. (a) H-Si(100)#HF3 with its (1×1) unit cell prepared by HF-etching. (b) UHV-treated Si#17; blue rectangles are the (2×1) reconstruction with streaks between the 1/2-order spots. (c) The (2×1) reconstruction disappears after the H-termination. The Si-unit cell is a green rectangle in all images.

is still slightly contaminated by C (black lines in Figure 5.2), and after the annealing, we observe a complete removal of the native oxide and the carbon contamination (compare the black and the red lines in Figure 5.2). Dosing atomic H to obtain an H-terminated surface does not introduce any impurities (orange lines in Figure 5.2). For a more detailed overview of the experiments, please refer to the summary of the samples and experiments in Appendix A.4.

5.2.2 Discussion

The H-Si prepared chemically and in the UHV showed the same reconstruction in LEED (Figure 5.1), which means that both approaches are potentially suitable for the growth of epitaxial Cu(100). The (2×1) reconstruction arises from the existence of the Si dimers. The streaks are related to the disorder of the dimer buckling, which would otherwise form a $c(4 \times 2)$ superstructure of alternately buckled dimers, as shown in Figure 5.3. Figure 5.3(a) shows a detail of the first Brillouin zone in our measurement, which is very similar to the one measured at 24 K by Shirasawa, et al. after a 50 s electron bombardment of the $c(4 \times 2)$ Si reconstruction [Figure 5.3(b)], which led to disordering of the dimer rows and thus streaks instead of well-defined diffraction spots [85]. One real-space c(4×2) Si domain is portrayed in Figure 5.3(c),

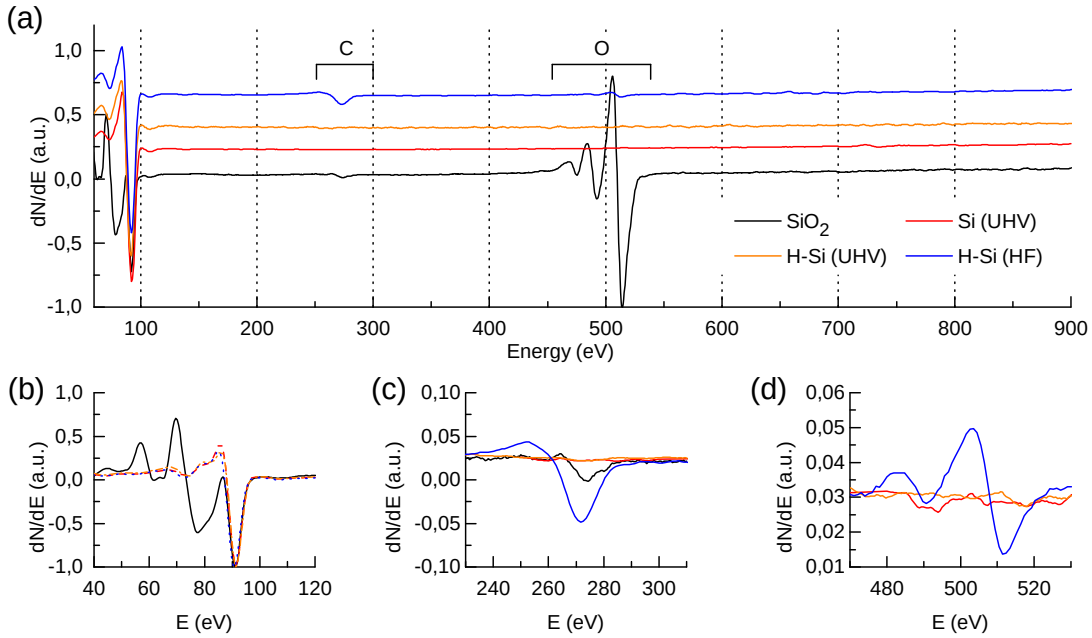

Figure 5.2 | AES analysis of the steps in the preparation of the H-Si(100). (a) Overview AES of the substrate on Si#23. The details in (b),(c) and (d) portray the Si, C and O peaks, respectively. The UHV-treated Si was outgassed (black - Si#23), annealed (red - Si#12) and H-terminated (orange - Si#12). The blue line corresponds to the chemically treated (HF-etched) H-Si#HF2. The black line is not included in (d).

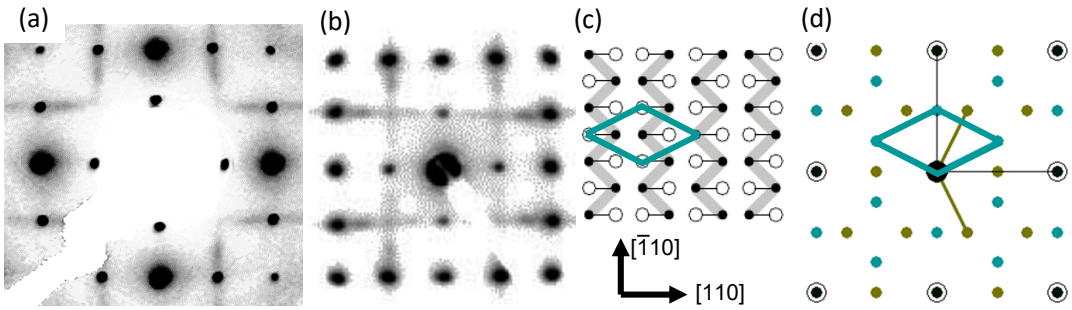

Figure 5.3 | Analysis of LEED of Si after flashing (a) A detail of the first Brillouin zone shown in Figure 5.1 (b) An inverted image from Shirasawa at 24 K. (c) real-space structure corresponding to the LEED pattern portrayed in (d). The open and full circles represent dimer atoms and the grey line represents the zig-zag rows of the buckled-down Si atoms. (d) A simulation of two c(4 × 2) domains performed by LEEDpat42 [84]. (b,c) are adapted from [85].

along with a simulation of the reconstruction in the reciprocal space. The zig-zag of the buckled dimers in the neighboring rows runs in antiphase, which gives rise to the c(4×2) superstructure.

The low-index diffraction spots of the chemically prepared H-Si [5.1(a)] are weaker than the ones on the UHV prepared H-Si [5.1(c)], which suggests that the chemically treated surface is not as clean as the UHV-treated one. AES confirmed this in Figure 5.2, where the blue line corresponding to the chemically prepared H-Si shows both C and O signals which did not desorb during the mild annealing. Because etching in HF for 2.5 minutes completely removes the SiO_2, we contribute this signal to an imperfect H termination of Si and a contamination during transport from the ambient atmosphere before introducing the sample into the UHV. Multiple steps of cleaning before the last HF-etch can reduce this contamination [70, 76].

5.3 Growth of the Cu(100) buffer layer

Cu was evaporated from two sources, the e-beam evaporator EFM3 (Focus), and the effusion cell (CreaTec). The material of the effusion cell crucible contained a small amount of Ca contamination. Due to the thermal radiation, the temperature of the sample increased by 10 K during the deposition from the effusion cell. The pressure during the deposition was 10^{-10} mbar (with the help of a liquid-nitrogen-cooled cryopanel and the TSP). The deposition rate of both Cu evaporators was 0.06 $Å s^{-1}$ (approx. 5.8 h for 130 nm). The deposition of the $Fe_{78}Ni_{22}$ layers is described in Section 2.5.

5.3.1 Results

We deposited Cu on both, the H-Si(100) substrates prepared chemically and in UHV. We grew 130-nm thick films because at this thickness we found a good compromise between the film morphology which improves with the film thickness [37] and keeping the deposition time manageable. The corresponding experiments are summarized in Appendix A.4. The deposition of Cu resulted in LEED patterns which confirm that

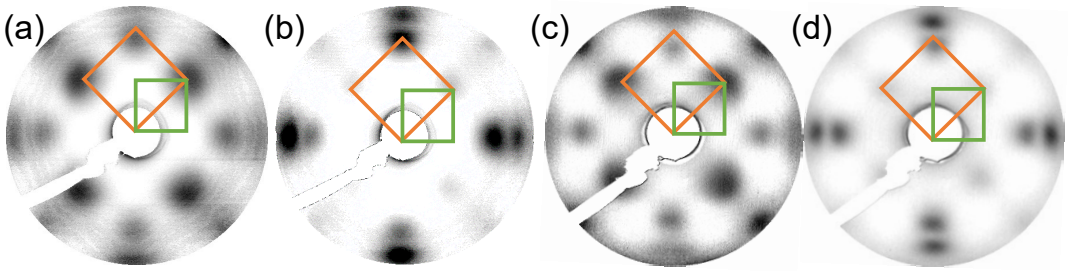

Figure 5.4 | LEED of 130 nm Cu/Si(100). The green rectangles correspond to the unit cell of the Si and the orange rectangles are the unit cell of the Cu. (a),(b) Cu buffer layer on the Si#13 prepared in the UHV. (c),(d) Cu buffer layer on chemically-prepared Si#HF1. (a) and (c) were acquired at 120 eV. Spot splitting is pronounced at the (1,1) diffraction maxima in (b) and (d) at 130 eV.

the as-grown Cu film on the chemically treated substrate was very similar to the one on the H-Si prepared in the UHV (see Figure 5.4). Both films showed a 45° rotation of their unit cell with respect to the underlying substrate and a real-space unit cell reduced by a factor of $\sqrt{2}$. In the reciprocal space, the unit cell is larger by a factor of $\sqrt{2}$, marked by orange and green squares in Figure 5.4. The fcc (100) diffraction spots are diffuse, and we could also observe their splitting at some energies, most significant at 130 eV, marked in Figure 5.4(b) and (d). We could also observe that the deposition of the Cu(100) on the HF-treated Si was not perfectly reproducible, and as a consequence, the Cu film grew in its more stable (111) structure (data not included, similar to [81]). However, it was not possible to connect this observation directly to the contamination of the chemically prepared H-Si or any parameter of the Cu deposition.

The 130-nm Cu buffer layer grown with the EFM3 e-beam evaporator on the chemically prepared H-Si was completely clean according to AES [violet lines in Figure 5.5], indicating that the impurities have either desorbed or got buried by the Cu deposition. We were not able to deposit an fcc (100) Cu buffer layer on the UHV-prepared H-Si by depositing pure Cu; the deposition resulted in a polycrystalline Cu(111) film. We were successful, however, in growing an fcc (100) Cu buffer layer when we used a

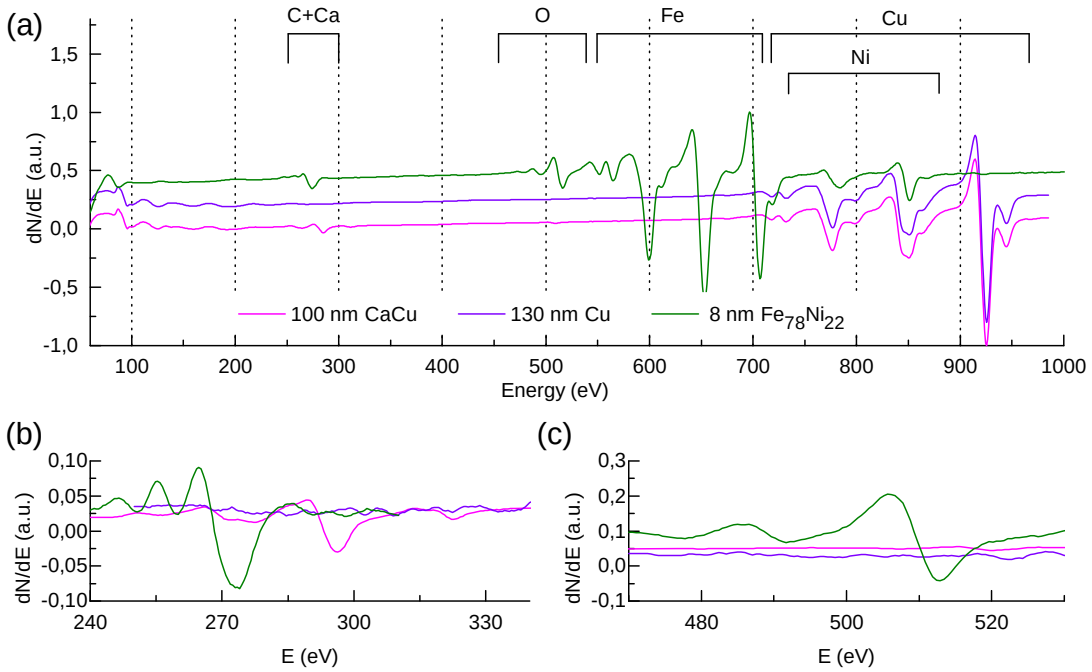

Figure 5.5 | (a) Overview AES after the consecutive deposition of Ca-contaminated Cu (pink), pure Cu (violet) on H-Si(100)#22 and $Fe_{78}Ni_{22}$ (green) on Cu/Si(100)#17. AES in (b) marks the details of C and Ca peaks and (c) is a detail of the O peak.

Ca-containing Mo crucible in the effusion cell. The surface of the 100 nm Cu films deposited from the Ca-containing Mo crucible had 2% of Ca, as estimated from the AES. After deposition of 100 nm Ca-contaminated Cu (pink lines in Figure 5.5) showing an fcc (100) structure, we have continued with the deposition of 30 nm of pure Cu, and the AES measurements after the deposition (identical with the violet lines in Figure 5.5) revealed that the completed film does not have any Ca on the surface. The structure of the 100+30 nm Cu film is fcc (100), marked in Figure 5.4(a) and (b). There is no trace of oxygen on both the Ca-containing Cu film and the as-deposited completed Cu buffer layer, as portrayed in Figure 5.5(c).

Deposition assisted with ion bombardment from the sputter gun did not bring any significant difference in the as-grown films. Deposition at lower or higher temperatures (-20 °C, ≥50 °C) led to a growth of polycrystalline fcc (111) films, in line with previous observations [78, 86]. Post-annealing did not lead to flattening of the films; in fact, we could observe a signal from Si in AES after heating to 150 °C for two hours,

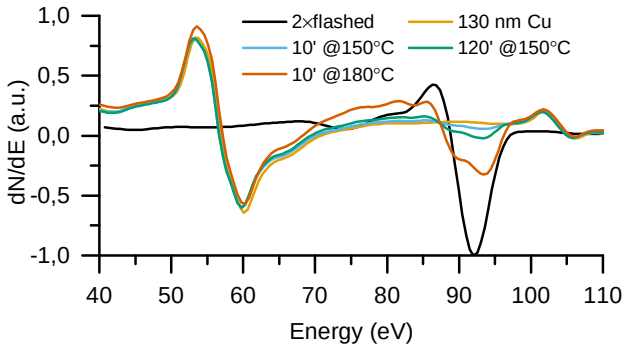

Figure 5.6 | Change of the AES signal of a low energy Si peak during post-annealing of a 130 nm Cu/Si#22. The red line represents a clean Si surface after annealing to 1200°C (normalized to Si_{92}). The yellow line is as-deposited 130 nm Cu, which then undergoes a brief post-annealing to 150 °C (blue), 2 h at 150 °C (green) and a brief post-annealing to 180°C (red). A splitting in the Si_{92} peak is visible. Peaks after the deposition and the post-annealing are normalized to Cu_{940}.

in contrast to Lukaszew et al. [79]. The 92 eV Si peak showed a splitting after the post-annealing (Figure 5.6). The black line corresponds to a clean Si(100) surface and serves as a reference for the data. The as-deposited film (yellow) does not have any Si signal, which starts to appear after 10 minutes annealing at 150 °C. It becomes more pronounced after longer post-anneal, and finally, the splitting of the Si peak is visible after post-anneal to 180 °C.

5.3.2 Discussion

Excessive contamination of the etched Si can prevent the growth of an epitaxial Cu(100) buffer layer; Cu then grows in (111) orientation [75]. The contamination of the chemically treated Si led to a low reproducibility of the epitaxial depositions on chemically prepared H-Si, and it was the main reason why we performed most of the experiments on substrates prepared by the UHV method, which enabled us to prepare completely clean substrates reproducibly. H-Si prepared in UHV is cleaner than the chemically treated Si [compare the orange and blue lines in Figure 5.2(a),(c) and (d)].

The fcc (100) diffraction spots of the Cu film are diffuse, and we could also observe their splitting at some energies, most significant at 130 eV, marked in Figure 5.4. Both

the diffuse spots and the splitting indicate a high density of (roughly equidistant) steps, in agreement with reports that the Cu grows as epitaxial islands with terrace widths of only a few nm [38]. We did not attempt to quantify the size of the terraces and islands, because exhaustive STM studies of fcc (100) Cu grown on the chemically prepared H-Si have been published [37, 38], and also an STM study of the initial phases of the Cu growth on H-Si prepared in UHV is available [87]. Nevertheless, we confirmed the morphology of the surface by SEM and AFM (data not shown).

Contamination by Ca proved to be an essential element in the epitaxial growth of Cu(100) on the UHV-prepared H-Si. The Ca concentration in the AES presented in Figure 5.5 is not necessarily the concentration in the films; Ca is virtually insoluble in Cu [88] so it is likely that Ca floats to the top during growth and only a negligible part is incorporated. We observed disappearance of the Ca signal upon depositing 30 nm of pure Cu on the Ca-containing 100-nm thick Cu film, which has confirmed the incorporation of Ca. If we would consider that the volume close to the surface (probed by AES) contains 2% of Ca and that this is incorporated in 165 ML (30 nm) of pure Cu, the minimal solubility of Ca in Cu is $\geq$0.01 %. Further experiments showed that even 10 nm of pure Cu suffice to incorporate the 2 % Ca, which increases the min. solubility to $\geq$0.04 %. Ca has an fcc structure and a 2.8% lattice mismatch to Si(100) and in this case, it most probably served as a surfactant supporting the epitaxial growth. The lack of oxygen in the as-deposited Cu layers confirms that the depositions were clean and there was no CaO deposited with the Cu.

We attempted to flatten the films by post-annealing to 180 °C, as described by Lukaszew et al., [79]. However, already upon post-annealing to 150 °C, the 92 eV Si peak started to appear (see Figure 5.6) and showed a splitting which got more pronounced with the time at 150 °C. The splitting corresponds to the formation of bulk copper silicides, i.e., hybridization between the Si 3p states and the Cu 3d states [69]. The hybridization either means that the Cu islands ripened so that the layer of copper silicides at the Cu-Si interface [69] were visible to the AES, or the interdiffusion of Cu and Si turned the whole film into the copper silicide.

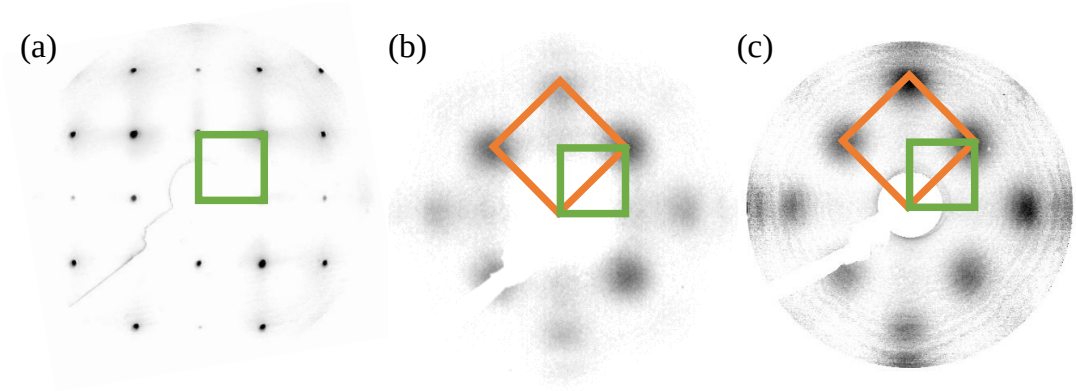

Figure 5.7 | LEED at 120 eV of a H-Si(100) and an 8 nm $Fe_{78}Ni_{22}$/130 nm Cu/Si(100). (a) the (1×1) unit cell of H-Si(100)#17 unit cell is a green rectangle in all images and orange is the unit cell of the metastable film. (b) Metastable films on chemically prepared substrate Si#HF1. (c) Metastable films on substrate prepared in UHV Si#20.

5.4 Growth of the metastable films

5.4.1 Results

We finished the preparation of the metastable films by depositing 8 nm of $Fe_{78}Ni_{22}$ on the epitaxial Cu(100) buffer layer grown on both chemically and UHV-prepared substrates. The diffraction spots in Figure 5.7(b),(c) are commensurate with and similarly diffuse as the ones on the Cu buffer layer [Figure 5.4]. The unit cell of the diffraction marked by an orange square is rotated by 45° with respect to the unit cell of the underlying H-Si (green rectangle in all images) and is $\sqrt{2}$ larger [Figure 5.7]. The similar spot shape indicates that the metastable film and the buffer layers beneath have a similar morphology and that the structure of the metastable film is also fcc (100). As the films were deposited with a CO background pressure, the surface of the metastable films contained 8% C and 5% O, as shown by the green line in Figure 5.5(a) and by the details of the C- and O-peaks in Figure 5.5(b) and (c), respectively. The C and O peaks arise from the dissociation of the CO, as described elsewhere [28]. The oxygen serves as a surfactant and forms a very weak c(2×2) superstructure at the bottom right and top left corners of the squares in Figure 5.4(b) and (c).

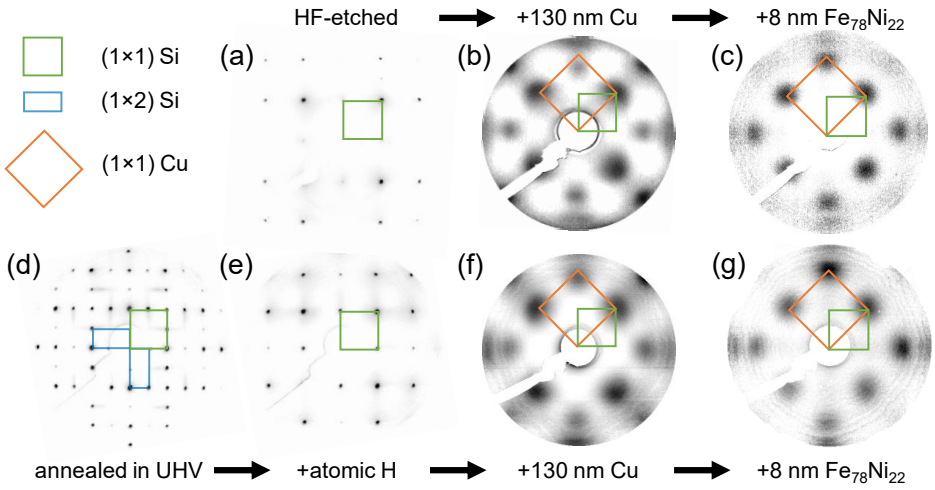

Figure 5.8 | Summary of the LEED images in Figures 5.1 5.4 and 5.7. Images taken at 130 eV except for (c) and (g) which were taken at 120 eV. (a) H-Si(100) with its (1×1) unit cell (green in all images) prepared chemically. (b) 130 nm Cu/H-Si(100) with its (1×1) unit cell (orange in all images). (c) 8 nm $Fe_{78}Ni_{22}$/130 nm Cu/H-Si(100) with its (1×1) unit cell. (d) UHV-treated Si; blue rectangles are the (2×1) reconstructions, which change into the (1×1) after H-termination, shown in (e). LEED patterns (f) and (g) correspond to the deposition steps (b) and (c) on the UHV-prepared substrate.

5.4.2 Discussion

The combination of LEED (Figure 5.7) and AES (Figure 5.5) demonstrates that it is possible to grow epitaxial films of $Fe_{78}Ni_{22}(100)$ using a Cu(100) buffer layer on H-Si(100) prepared by either wet chemistry or in UHV. The position and size of the diffraction maxima mean that the $Fe_{78}Ni_{22}(100)$ films are commensurate with the underlying Cu(100) buffer layer.

Figure 5.8 is a combination of the previously shown LEED (Figures 5.1, 5.4 and 5.7) to have an overview of the LEED images for a direct comparison. We see from the figure that the UHV and chemical approaches give very similar results.

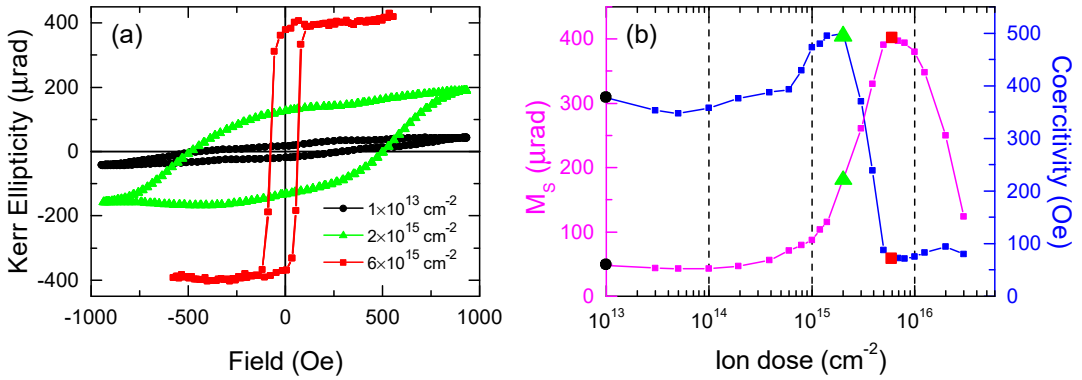

Figure 5.9 | Longitudinal UHV SMOKE *in-situ* measurements of an 8 nm $Fe_{78}Ni_{22}$ film/ 130 nm Cu/ Si(100)#17. The irradiation was performed by 4 keV Ar^+ ions. (a) the as-deposited film is weakly FM (black). The film partially transforms to bcc (green) after irradiation with dose of 2×10^{15} cm^{-2}. The magnetization reaches a maximum at an ion dose 6×10^{15} cm^{-2} (red). (b) dependence of the Kerr ellipticity at magnetic saturation (M_S, magenta) and coercivity (blue) on the ion dose. Black, green and red symbols correspond to the measurements in (a).

5.5 Ion-beam induced transformation

5.5.1 Results

The experiments presented in Figure 5.9 and 5.10 were performed on samples prepared by the UHV treatment; the samples treated by wet chemistry showed equivalent results. SMOKE measurements of the as-deposited films and mildly irradiated films [ion dose 10^{13} cm^{-2} - black circles in Figure 5.9(a)] show a non-zero magnetic signal suggesting that a small fraction of the film is already in the bcc ferromagnetic (FM) phase. Irradiation with a dose of 2×10^{15} cm^{-2} leads to a partial magnetic transformation; the hysteresis loop [green line in Figure 5.9(a)] exhibits high coercivity, and the Kerr signal reaches approx. 50% of the maximum value measured for the fully transformed film. An ion dose of 6×10^{15} cm^{-2} completely transforms the film [red rectangles in Figure 5.9(a)]. The magenta line in Figure 5.9(b) shows the magnetic transformation of the metastable film with the increasing ion dose and includes the black, green and red datasets from 5.9(a). We do not detect any measurable increase up to an ion dose of 2×10^{14} cm^{-2}. The magnetic signal then increases with increasing ion dose up to 6×10^{15} cm^{-2}, where it reaches a maximum and then decreases as the

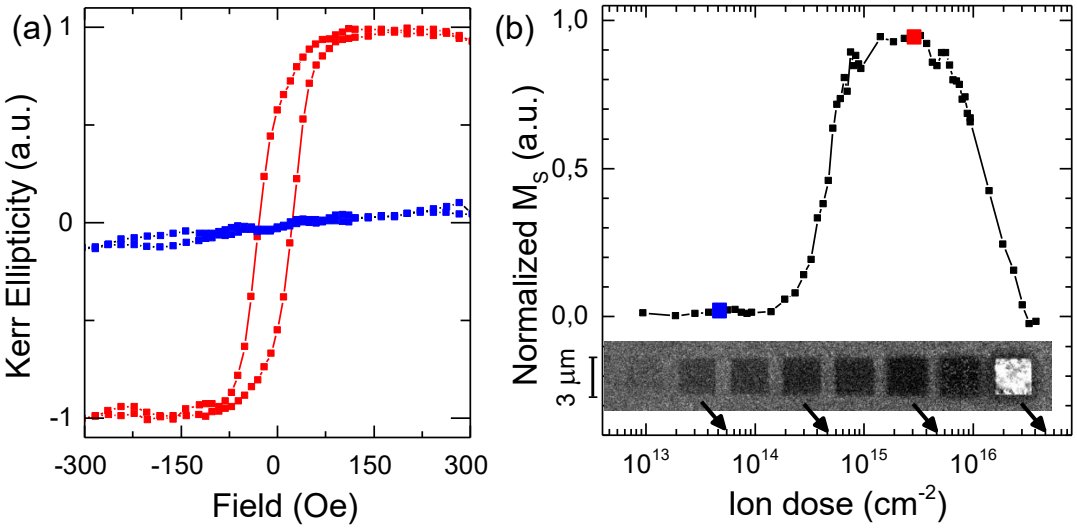

Figure 5.10 | SEM and Kerr microscope analysis of $3 \times 3\,\mu m^2$ squares in a 8-nm $Fe_{78}Ni_{22}$/130 nm Cu/Si(100)#20 films irradiated by a 30 keV Ga^+ FIB for different ion doses. (a) The Kerr microscope shows that there is no ferromagnetic signal on the as-deposited films and films irradiated with dose up to 1.5×10^{14} cm^{-2}. These are represented by the blue line, which corresponds to a square irradiated with an ion dose of 5×10^{13} cm^{-2} (blue line). The film has the maximum magnetic saturation (M_S) when irradiated by an ion dose 2–3 $\times 10^{15}$ cm^{-2} (red line). The surrounding fcc area does not show any hysteresis. (b) Summary of the Kerr signal at saturation for various ion doses with the Kerr signal from the as-deposited film subtracted. The inset at the bottom shows SEM images of the irradiated squares for the ion doses at the abscissa (with a half-an-order step starting at 10^{13} cm^{-2}). The nanopatterns were made and characterized by Viola Krizakova and Lukas Flajsman at CEITEC.

magnetic thin film is sputtered away and intermixes with the Cu layer below. The ion dose where we reach the maximum transformation is equal to the transformation dose for the metastable films grown on a Cu(100) single crystal [32]. The maximum Kerr ellipticity of the films on the Cu buffer layer is 10% lower than for films deposited on a Cu(100) single crystal [32]. The coercivity [blue line in Figure 5.9(b)] starts increasing at the same ion dose as the magnetic saturation (around 2×10^{14} cm^{-2}) to reach a maximum at 2×10^{15} cm^{-2}. It then falls rapidly to its minimum, which matches the maximum of the magnetic saturation at 6×10^{15} cm^{-2}.

Figure 5.10 shows the results of patterning the metastable films with the FIB. The grey level in SEM [inset at the bottom of Figure 5.10(b)] can be used for distinguishing the as-deposited (grey) areas and the irradiated (darker or brighter) areas and serves as

a valuable pre-characterization tool. The irradiated areas become darker at a dose of 5×10^{13} cm^{-2} but brighten again at doses above 10^{16} cm^{-2}. The last square then shows the signal from the Cu below after a complete removal of the $Fe_{78}Ni_{22}$ film. The data from Kerr magnetometry (Figure 5.10) show the onset of the magnetic transformation at an ion dose of 10^{14} cm^{-2}. The maximum of the magnetization is achieved at ion doses of $2–3 \times 10^{15}$ cm^{-2}. The transformation by 30 keV Ga^+ ions qualitatively shows the same behavior as the transformation performed in-situ [see Figure 5.9(b)], but the ion dose needed to achieve full transformation is lower for the Ga^+. Figure 5.10(a) shows the hysteresis loops of the squares irradiated by a low ion dose (black line) and at the maximum of the magnetization (red line). The squares irradiated by the low ion dose do not show any FM signal, which contrasts with the measurement by UHV SMOKE in Figure 5.9 (black line).

5.5.2 Discussion

UHV SMOKE of the as-deposited and the irradiated films confirms that the films are metastable, i.e. it is possible to induce a magnetic transformation from paramagnetic to ferromagnetic phase by ion beam irradiation. The as-deposited and the weakly irradiated films already exhibit some FM signal, which contrasts with the measurements by the Kerr microscope [compare black line in Figure 5.9(a) and blue line in Figure 5.10(a)]. We assume we do not measure any signal on the as-deposited and the weakly irradiated metastable films in the Kerr microscope because the UHV SMOKE setup collects the signal from a large area, and the Kerr microscope measured none of the minority areas already in the bcc FM phase. At the optimal ion dose, the maximum Kerr signal is 10% lower than that on the Cu single crystal, which we attribute to the corrugation of the film arising from the underlying Cu buffer layer.

From observations on the Cu(100) single-crystal substrates we know that increasing the ion dose increases the number and size of bcc nuclei randomly dispersed in the fcc layer. The maximum in the coercive field corresponds to the nuclei reaching the maximum size for single magnetic domains. This property is well known from

magnetic nanoparticle studies [89]. Further lowering of the coercive field is attributed to multi-domain states of magnetic particles and more efficient interaction in between the nanoparticles through the stray field of individual particles.

The coercive field dependence on ion dose has not been addressed for the microstructures presented in Figure 5.10 because we could not tune the magnetic anisotropy in the same extent as in the case of $Fe_{78}Ni_{22}$/Cu(100), discussed in Section 4.4. We could observe that the coercive field of the microstructures reflected the shape of the prepared structures and the number of defects found in the structures and we, therefore, think that the coercive field possesses a stochastic character [67].

The SEM measurement in Figure 5.10 shows that the irradiated areas decrease in brightness with an increasing ion dose. The reason for the decrease of the SEM signal is the fcc $\rightarrow$ bcc structural change, which affects electron channelling and associated secondary electron emission [40]. An ion dose above 10^{16} cm^{-2} removes the metastable film entirely and thus exposes the Cu buffer layer. The change of the brightness in this case might be explained by the change of the work function (Φ), which is directly connected to the emission of the secondary electrons. Even though the experimental value of Φ for the fcc (100) plane of Fe [$\Phi_{Fe} = 4.57$ eV [90]] is very similar to that of Cu [$\Phi_{Cu} = 4.59$ eV [91]], the FeC has a slightly higher work function [$\Phi_{FeC} = 5.83$ eV [92]] with respect to CuC [$\Phi_{CuC} = 5.66$ eV [92]]. The change in the contrast might therefore suggest that carbides form on both the Fe and Cu surfaces, which is not surprising because the specimens are irradiated by an 10 keV electron beam in 10^{-7} mbar.

The transformation by 30 keV Ga^+ ions qualitatively shows the same behavior as the transformation performed by lower energy Ar^+, and the ion dose needed to achieve full transformation is lower for the Ga^+ as was the case for the metastable films on the Cu(100) single crystal. In the discussion of Chapter 4, Section 4.4, we showed that the penetration depth, energy deposition and intermixing are higher for the Ga^+ ions, and the transformation is therefore more rapid with respect to the transformation induced by Ar^+ ions.

5.6 Conclusion

We showed in this chapter that it is possible to use the hydrogen-terminated Si(100) with an epitaxial Cu buffer layer to grow metastable $Fe_{78}Ni_{22}$ films. The films are paramagnetic and an ion irradiation transforms them into the ferromagnetic (FM) phase, and we can tune their magnetization by the ion dose. We fabricated in the metastable films (paramagnetic matrix) FM microstructures via FIB. The Kerr signal of metastable films on the new Cu/Si(100) substrate is 10% lower than that on the Cu single crystal [32, 40], which we assume is caused by its corrugation. For the ion-beam-induced transformation, we used Ga^+ and Ar^+ ions, and they exhibited different transformation efficiency, which is similar to what we observed on the metastable films on Cu(100) single crystal.

We have presented two (UHV and chemical) possibilities for the preparation of the H-Si(100) substrate of which the UHV alternative has not been used in the past for the growth of the Cu buffer layer. We explored the UHV method of the H-Si preparation for the deposition of the buffer layer, and we found that the presence of 2% Ca is necessary to stabilize the growth of the fcc (100) Cu. The role of the Ca in the stabilization of the epitaxial growth of Cu(100) warrants further investigations. Post-annealing of the Cu buffer layer led to dewetting, and future research should investigate alternative ways for obtaining flat films.

Chapter 6

Metastable Films on Diamond

In this section, we show and discuss the results obtained from depositing and transforming the metastable $Fe_{78}Ni_{22}$ films on diamond.

6.1 Introduction

Diamond is an attractive material for industrial applications because of its high thermal conductivity, hardness, chemical stability, transparency to the visible light, and to the lack of electrical conductivity [5.45 eV band gap [93]]. The H-termination of diamond [H-C(100)] changes the position of the Fermi level and therefore leads to negative electron affinity, which can be used in cold cathode devices, or carrier-injecting electrical contacts [94]. The undoped H-C(100) can, therefore, be used as a surface-channel field effect transistor (MESFET or MISFET) in high-speed switches [95]. Face-centered-cubic (fcc) Fe, or γ-Fe, grows epitaxially on the diamond because of a small lattice mismatch (0.1%) and Fe intermixes with C at the interface [96–99]. The fcc Fe can be a template for the epitaxial growth of other metals and thus interesting for the applications in electronics because the fcc Fe enables contacting of non-carbide-forming metals, such as Cu, to diamond.

The metastability of the fcc Fe films on diamond presents a second class of applications, in which a focused ion beam (FIB) can write magnetic nanopatterns in a

nonmagnetic matrix, as shown in the chapters 4 and 5. Such an approach can lead to the fabrication of magnonic crystals and bring magnonics onto a transparent and non-conductive substrate. An option for magnon excitation in spintronics is the parametric pumping through a transparent substrate [100], which might be enabled by the metastable films on diamond.

Fe forms a flat and polycrystalline film on the diamond (100) at room temperature (RT) with a critical thickness of 5-ML (0.9 nm), at which it transforms into its stable bcc form [98, 101]. However, when the films are deposited in steps ($\leq$5 ML) and consequently post-annealed to 350 °C, the γ-Fe grows epitaxially on diamond up to 13 ML (2.4 nm) [99]. The step-wise deposition does not allow for the critical thickness to induce relaxations in the form of the energetically more favourable bcc-defects, and the post-annealing leads to the diffusion of C from the diamond surface and to re-organization into the austenite, γ-Fe [99]. The deposition at RT restricts the C-diffusion, and this poses the critical thickness barrier [97]. For applications, however, it would be suitable to increase the thickness of the fcc films above 13 ML, and in the case of the fcc-to-bcc ion-beam-induced transformation, the fcc Fe should not be in a stable austenite state which is formed because of the C interstitials. On top of that, the diamond preparation for deposition presented in the literature requires *ex-situ* treatment to remove the deposited metals, and an *in-situ* cleaning procedure would simplify the preparation. The *in-situ* treatment would include sputtering of the Fe film. The sputtering would inevitably lead to irradiation of the diamond, which would result in an sp_3 (diamond) $\rightarrow sp_2$ (graphite) transformation.

We present in this chapter that it is possible to clean the diamond *in-situ* by sputtering the Fe layer and then etching by atomic H in UHV. We show that it is possible to grow metastable fcc $Fe_{78}Ni_{22}$ on diamond, when the growth is performed at 450°C in a carbon monoxide (CO) backpressure. The increased deposition temperature leads to a relaxation of the as-deposited film into the metastable fcc state, and the CO assures a stable, well-defined C-doping of the whole film. Finally, the Ni has a similar atomic radius as Fe and supports the fcc-Fe phase [32]; on top of that, we showed in Chapter 4

that it overcomes the thickness limit on Cu(100). We confirm the metastability of these films by ion-beam-induced magnetic and structural transformation.

6.2 Preparation of the C(100) surface

We prepared the diamond surface in two UHV systems (RT-STM and PINUP) described in sections 3.2 and 3.1, respectively. The experiments were performed on undoped C(100) crystals type IIa from Element Six with dimensions $4.5\times4.5\times0.3\,\mathrm{mm}^3$, with a roughness of $R_a \leq 5\,\mathrm{nm}$ and $3\times3\times0.3\,\mathrm{mm}^3$ with $R_a \leq 20\,\mathrm{nm}$. The summary of the samples used for the experiments shown in this chapter is included in Appendix A.3. The samples were cleaned *ex-situ* in aqua regia and in boiling Piranha solution, with sonication in ultrapure Merck (miliQ) water in between and afterwards. After introducing the samples into the UHV, we outgassed the samples at 800 °C and etched them by atomic H. The H-etching was performed by a home-built H-cracker; its typical operation parameters are shown and discussed in Section 3.1.1 and the technical details are in the appendix B. The sample was exposed at 10^{-6} mbar H_2 pressure and was kept at 500 °C to achieve fastest graphite etching [61, 63]. We calibrated the atomic H dose from achieving a H-termination of Si(100), as shown in Section 3.1.1. We also inserted out-of-the-box samples and they had the same purity after outgassing and cleaning with atomic H as the etched samples.

AES measured the chemical composition of the C(100) surface. We used the G-factor to describe the purity of the diamond substrates. There is a difference between the sp_2 (graphitic) and the sp_3 (diamond) AES signals and we used this to measure the cleanliness of the diamond, as described elsewhere [102]. The G-factor has been calculated as a ratio of the difference between the graphitic (sp_2) and diamond (sp_3) average peak-to-peak height (APPH) and the APPH of the whole C-peak [see Figure 6.1(d)] [102].

6.2.1 Results

We measured no contamination in AES on an annealed C(100) and we decreased the amount of graphite by atomic hydrogen etching. The G-factor slightly decreased and after dosing approx. 10^3 L [see blue data points in Figure 6.1(e)] we assumed the crystal is clean of graphite, as shown by the blue line in Figure 6.1(d). We then irradiated the sample with 2.3×10^{14} cm^{-2} Ar^+ ions with 500 eV energy to induce an $sp_3 \rightarrow sp_2$ transition. The G-factor immediately changed in favour of the graphitic peak [red line in Figure 6.1(d)]. The diamond exhibited a weak diffraction pattern which arises from the bulk diamond [Figure 6.1(b)]. Consecutive H-etching initially did not lead to a change in the G-factor, with a step decrease around the H-dose of 11×10^3 L. The G-factor was constant after dosing above 24×10^3 L of atomic H. The H-etched surface in Figure 6.3(c) corresponds to the last data point in Figure 6.3(e) and exhibits an fcc(100) diffraction pattern, where the spots are larger than the ones of the as-inserted surface in Figure 6.1(a). The G-factor of the irradiated and H-etched diamond was like the one on the as-inserted and H-etched diamond [compare the green and blue datapoints in Figure 6.1(e)]. We also post-annealed the substrate treated by atomic H to 800 °C, but this did not change the G-factor.

6.2.2 Discussion

The (2×1) reconstruction with elongated diffraction spots, portrayed in Figure 6.1(a) arises from dimerization of the surface atoms, which are connected by both σ and π bonds. It is possible that the spots are elongated because of the non-conductive substrate, which becomes charged. We assume that the 500 eV Ar^+ ions transformed only the top layers of diamond because it is possible to see diffraction spots in the LEED image after the sputtering [Figure 6.1(b)]. This is in contrast to Monte Carlo simulations using the stopping and range of ions in matter (SRIM) [58]. According to SRIM, the average ion penetration depth into carbon (and therefore the ion-beam-induced $sp_3 \rightarrow sp_2$ transition) is approx. 2 nm. After sputtering and consecutive

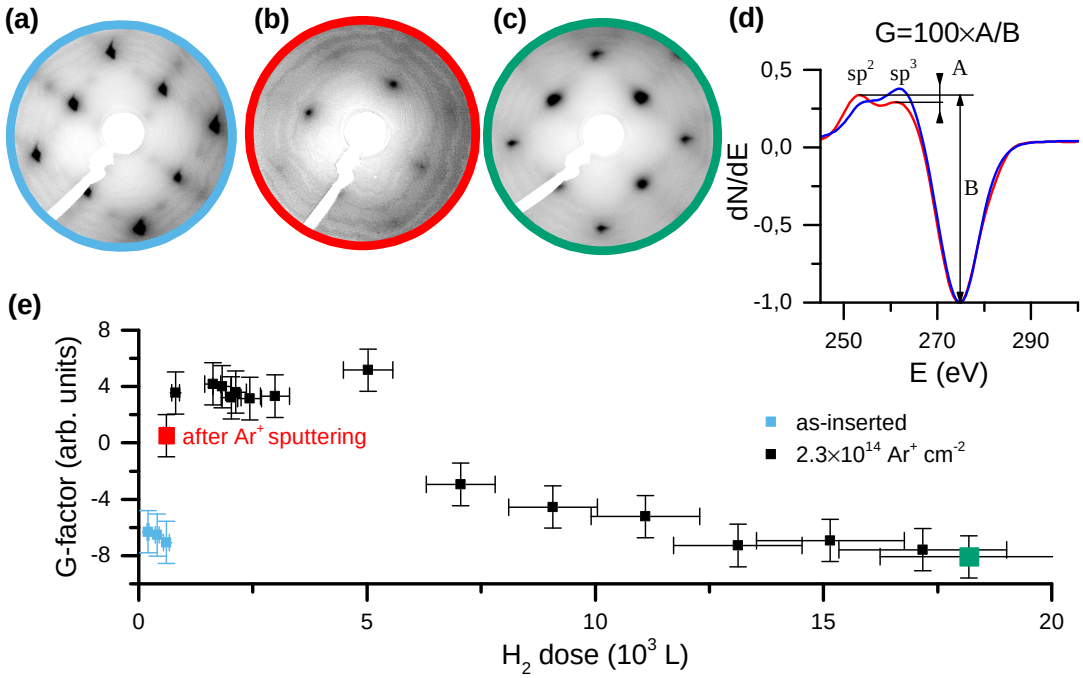

Figure 6.1 | AES of C#3 treated by ion beam irradiation and by atomic hydrogen. a) LEED at 125 eV on as-inserted and annealed diamond. b) LEED at 135 eV of diamond sputtered by 2.3×10^{14} cm^{-2} 500 eV Ar^+. c) LEED at 135 eV of a sputtered diamond cleaned by 39 000 L of atomic H. d) G-factor calculation. Blue and red colour correspond to as-inserted and irradiated diamond, respectively. The difference in APPH of sp_2 and sp_3 signal is visible. e) Dependence of the G-factor on the H dose. Blue and black data points were measured after consecutive steps of H-deposition on as-inserted and irradiated diamond, respectively.

cleaning, the spots are larger than the ones on the surface of an as-inserted diamond sample, which most probably means that the size of the flat terraces has decreased. This is supported by the lack of the (2×1) reconstruction, which points out that there are no large flat areas where the relaxation of surface C atoms could take place. Figure 6.1 therefore suggests that diamond single crystals sputtered and etched by atomic hydrogen lead to a corrugated surface with the same phase purity as before sputtering. A similar effect was observed by XPS on diamond [103]. We avoided any effect on the reproducibility of our experiments by the sputter-induced corrugation by depositing the metastable films on out-of-the box C(100) annealed to 900°C and cleaned by atomic H. We confirmed, however, that it is also possible to grow the metastable films on the previously sputtered substrates. The diamond surface can be made flatter by a H plasma at high temperature [103].

6.3 Growth of the metastable films

The depositions were performed in the PINUP and RT-STM systems. For deposition, we used the parameters we found to be sufficient to stabilize the fcc Fe on Cu(100) [Chapter 4 and [32]] and Cu(100)/Si(100) [Chapter 5 and [41]]. These were alloying of Fe with 22% Ni and deposition in 5×10^{-10} mbar CO. In the following, it will be shown that it is necessary to increase the temperature of the substrate to achieve epitaxial growth of the $Fe_{78}Ni_{22}$/C(100). We tried two approaches to grow the epitaxial metastable films at elevated temperatures. Firstly, we post-annealed the film grown in steps below the 5-ML (0.9 nm) critical thickness. Secondly, we varied the temperature of the substrate during growth.

6.3.1 Results

Deposition of 4-nm-thick layers on C(100) at RT resulted in a diffuse LEED pattern caused by the stable bcc phase (confirmed also by SMOKE). Figure 6.2(a) shows the reconstruction on the C(100) for a reference and Figure 6.2(b) the diffraction pattern

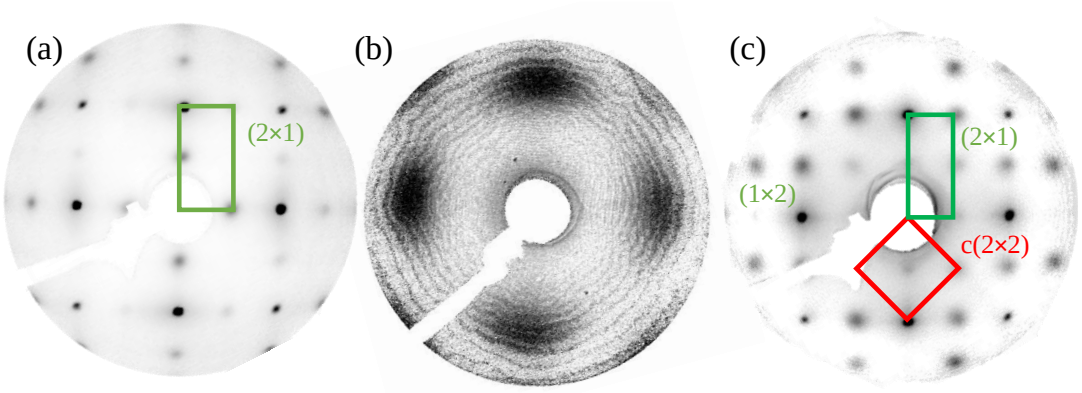

Figure 6.2 | LEED of C(100)#4 and deposition of $Fe_{78}Ni_{22}$/C(100)#4. (a) C(100) with a (2×1) reconstruction, LEED at 145 eV. (b) 4 nm $Fe_{78}Ni_{22}$/C(100) deposited at RT, LEED at 120 eV for best visibility of the spots. The roughly concentric ring-like features are an artifact. (c) 4 nm $Fe_{78}Ni_{22}$/C(100) deposited in 4-ML (0.72 nm) steps with post-annealing, LEED at 145 eV.

on the 4-nm-thick film deposited at RT. Metastable fcc films obtained by depositing in 4-ML (0.72 nm) steps. For pure Fe/C(100), this avoids the critical thickness [99], at which the stable bcc dislocations are introduced. The deposition was then followed by annealing up to a temperature (450 °C) at which we could observe the formation of the fcc structure with a diffraction pattern. The final thickness of the film deposited step-wise presented in Figure 6.2(c) was 4 nm. After deposition and annealing, the LEED pattern in Figure 6.2(c) shows the fcc(100) diffraction spots and the O-c(2×2) and (2×1) superstructures. The (2×1) superstructure was already observed on the substrate.

We measured STM after each deposition and post-anneal steps but did not achieve atomic resolution on films thinner than 4 nm. Once the film reached a sufficient 4-nm thickness, we were able to measure the atomic distribution on the surface, as shown in Figure 6.3(a). The STM view at the atomic scale shows the c(2 × 2) oxygen superstructure with missing oxygen rows on the $Fe_{78}Ni_{22}$. The atomic distance in the oxygen reconstruction corresponds to the $\sqrt{2}/2 \times a_{\text{fcc Fe}}$. An STM image of a larger area depicted in Figure 6.3(b) shows the missing oxygen rows on a flat terrace with a diameter of approx. 20 nm. There are a few threading dislocations appearing on the surface of the islands. The island has rather steep edges, and thus we observe the

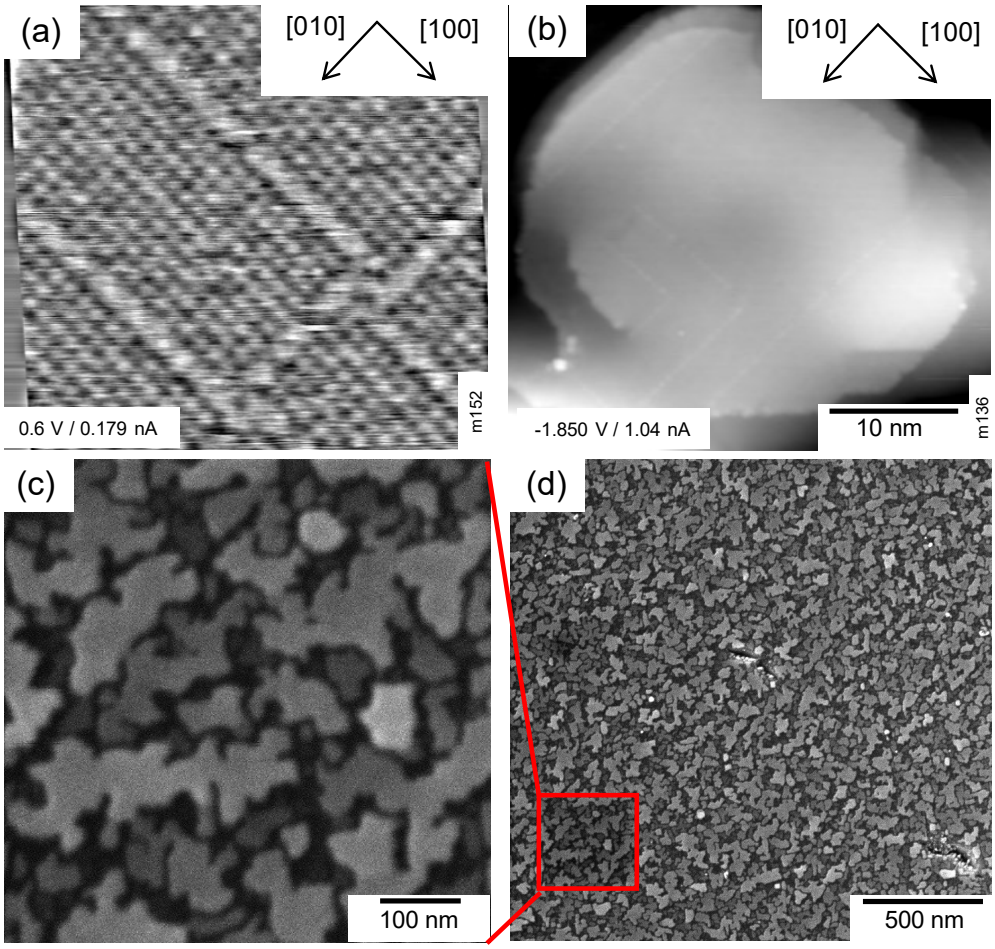

Figure 6.3 | Structural analysis of $Fe_{78}Ni_{22}$/C(100). (a) high-pass filtered STM of 4 nm $Fe_{78}Ni_{22}$/C(100)#4 depict the surface of the metastable film with atomic resolution. (b) STM of 4 nm $Fe_{78}Ni_{22}$/C(100)#4. The sharp edges of the island show the convolution of the tip with the edges. (c), (d) SEM on 8 nm $Fe_{78}Ni_{22}$/C(100)#6 shows the morphology of the metastable film's islands.

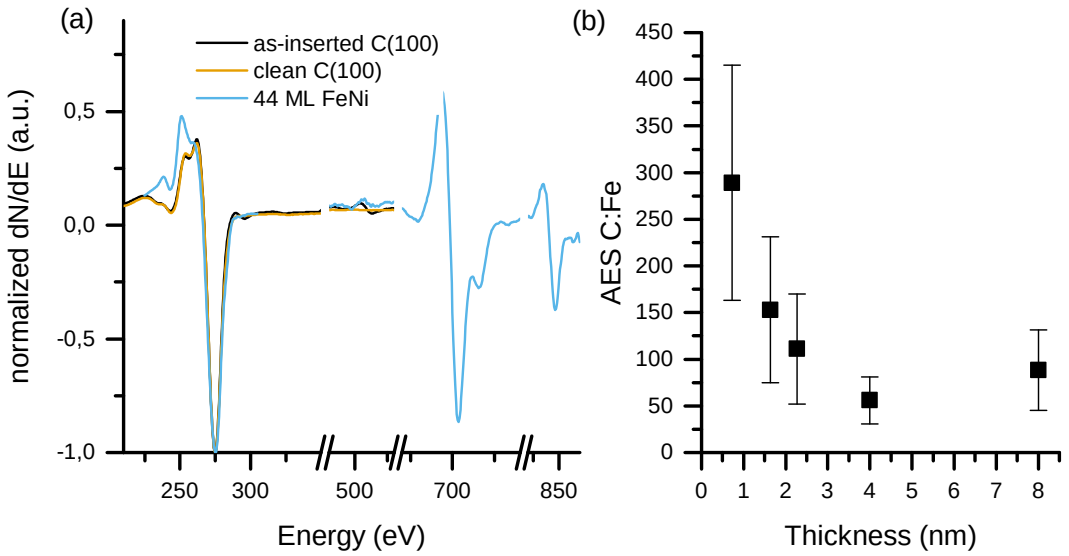

Figure 6.4 | AES analysis of steps in the deposition of the $Fe_{78}Ni_{22}$/Cu(100). (a) AES of as-inserted, cleaned C(100)#9 and on 8 nm$Fe_{78}Ni_{22}$/C(100)#9 deposited at 450 °C. Changes in the C and O peaks are visible. (b) AES of the APPH of C with respect to the APPH of Fe on the step-wise deposited metastable films at 450 °C on C#2,4,6,7,9.

signal arising from the convolution of the tip shape and the edge of the island.

We then deposited 8 nm $Fe_{78}Ni_{22}$ in one step, at the temperature we used for post-annealing in the step-by-step deposition (450°C). Deposition at 450 °C led to the same LEED pattern as in Figure 6.2(c), confirming that this substrate temperature allows for the epitaxial growth of fcc $Fe_{78}Ni_{22}$. Figure 6.3(c) and (d) shows the morphology of these 8-nm-thick films as measured by SEM. The islands seem to have random shapes and sizes with a roughly constant height within each island. However, SEM is not a technique that is very sensitive to height. The SEM images show that the metastable film forms islands with narrow grooves between the islands.

The chemical analysis of the diamond substrate and the respective deposition steps by AES are portrayed in Figure 6.4. The as-inserted diamond has some adsorbates on the surface [O peak in the black line in Figure 6.4(a)], which are removed by annealing and H-etching (orange line), shown and discussed in Figure 6.1. The deposition of 8 nm of $Fe_{78}Ni_{22}$ at 450 °C results in AES marked by the blue line in the Figure 6.4(a). We combined the data from step-by-step and one-step depositions on five substrates (C#2,4,6,7,9) which led to the formation of the metastable films to show

the dependence of the C-signal on the thickness of the metastable film. The data from these multiple depositions are presented in Figure 6.4(b) and show a decrease in the C signal with respect to the Fe peak. The C:Fe ratio always increased after post-annealing the step-wise deposited layers. After post-annealing to 450 °C of the 4 nm $Fe_{78}Ni_{22}$ deposited at RT, we measured a six-fold decrease in O signal (from 12% to 2% APPH, not sensitized).

6.3.2 Discussion

The bcc diffraction pattern on the 4-nm-thick film deposited at RT in Figure 6.2(b) resembles the bcc $Fe_{78}Ni_{22}$/Cu(100)[32]. The splitting of the bcc spots is due to the 15° rotation of the bcc areas with respect to the fcc(100), as was already shown and discussed in Chapter 4. The transformation into the bcc Fe(110) was observed and discussed for Fe/C(100) thicker than 5 ML (0.9 nm) without any stabilizing agents [99]. Figures 6.2 and 6.3 show that it is possible for the metastable films to grow thicker if they are given enough energy, to intermix with the substrate and form fcc Fe and to continuously reorganize into the epitaxial metastable state [99]. The LEED, STM and SEM observations suggest the growth at RT is kinematically limited and the post-annealing or the deposition of the whole film at the 450 °C allows the system to reach its thermal equilibrium for the growth of the metastable films. We do not assume that the kinematic limitation of the growth comes from the Ehrlich-Schwöbel barrier, because the barrier is known to be low for metals in the (100) orientation [104]. Yet, the increased temperature is necessary for the formation of the epitaxial fcc Fe islands.

In Figure 6.2(c), the oxygen in the c(2×2) reconstruction originates from the dissociation of CO on Fe [28]. As was the case on the metastable films on Cu, we assume the C is incorporated into the film and supports the fcc Fe, and O serves as a surfactant and forms the c(2×2) [27, 28]. We attribute the decrease of the O content upon post annealing to the desorption of weakly bound CO molecules on the polycrystalline film during the reorganization of the surface. The Fe-O bond is strong enough to

withstand the post-annealing temperature [104].

We measured STM after each deposition and post-anneal step but did not achieve atomic resolution on films thinner than 4 nm [Figure 6.3(a) and (b)], which could be explained by the following: Firstly, the as-deposited films are poorly ordered and thus there is no measurable atomic order prior post-anneal (confirmed by LEED). Secondly, coarsening of films thinner than 4 nm leads to disconnected $Fe_{78}Ni_{22}$ islands and thus removes the conductive overlayer from the nonconductive substrate. Finally, the coarsening of the metastable film upon post-annealing made the size of the atomically flat areas below the smallest scale for scanning of the STM. The flat terrace has a few threading dislocations, which directly confirm the suggestion of Hoff et al. [98] that the strain relaxation in Fe/C(100) might occur through the introduction of the threading dislocations. These dislocations therefore form an alternative stress relaxation to the transformation into the energetically stable bcc Fe(110). We assume the stress comes from the half-step of diamond, which cannot be accommodated by the full ML of Fe and thus propagates through the whole epitaxial layer.

The C:Fe ratio always increased after post-annealing the step-wise deposited layers, which corresponds either to diffusion of C, or the exposure of the diamond substrate, or the combination of both. The STM and SEM show that the metastable film forms islands with very narrow grooves between the islands and LEED with STM confirm the O-reconstruction on the surface of the metastable islands. At the same time, LEED shows that there is a pronounced (2×1) reconstruction visible. Its intensity is stronger than what we observed on diamond substrates; in case that it arose from the substrate, there would have to be large flat patches of diamond with the C dimers. It should, however, be energetically more favourable for the C to form a chemical bond with Fe, without the possibility of breaking it at 450 °C. The experimental evidence therefore suggests a formation of a new crystalline Fe-C phase beneath the metastable film which appears in the grooves between the islands. We could observe that the AES peaks on the step-by-step deposited films had a triple C-peak, which points to the formation of a new phase. Yet, the triple C-peak was not confirmed for the films

deposited at 450 °C. The shape of the AES peak and the possible formation of the new Fe-C phase therefore warrants further investigations.

6.4 Ion-beam-induced transformation

We extend the analysis of the as-deposited and irradiated metastable films by SMOKE and micro-MOKE measurements, which give us information about the magnetic properties of the films. Large-Area irradiation of one set of samples was performed in-situ in the PINUP system by the Specs ion gun with ion beam perpendicular to the sample with a current density $10^{13}\,\mathrm{cm^{-2}s^{-1}}$. We used 4 keV Ar^+ ions, which penetrate deep into the 8-nm-thick $Fe_{78}Ni_{22}$ layer and do not cause significant intermixing at the interface with the substrate as was shown in Section 4.4. During the ion beam irradiation, we periodically measured magnetic hysteresis loops by the home-built SMOKE. Ex-situ magnetic nanopatterning was performed in the combined FIB-SEM Tescan LYRA 3. A series of circles with 3 μm^2 diameter was irradiated with the Ga^+ FIB at 30 keV. After the irradiation, the magnetic properties of the patterns were measured by the micro-Kerr magnetometer MIRANDA.

6.4.1 Results

Figure 6.5 shows SMOKE on 8 nm $Fe_{78}Ni_{22}$/C(100) which we irradiated and measured *in-situ* with the broad ion beam; the film was grown in one step at 450 °C. The as-deposited layer has a non-zero magnetic saturation and it reaches an approx. six-fold increase in magnetic saturation (M_S) after the ion beam dose of $1.5 \times 10^{16}\,\mathrm{cm^{-2}}$. The magnetic saturation then decreases with further irradiation. The magenta line in Figure 6.5 shows the evolution of the coercive field (H_C) with the ion dose. We observe the Hc has a similar dependence on the ion dose as the M_S, but does not decrease for the doses above $1.5 \times 10^{16}\,\mathrm{cm^{-2}}$. The inset shows hysteresis curves of the as-deposited 8 nm film (orange line) and the irradiated film (blue and green lines) which correspond to the points with respective colours on the black and magenta

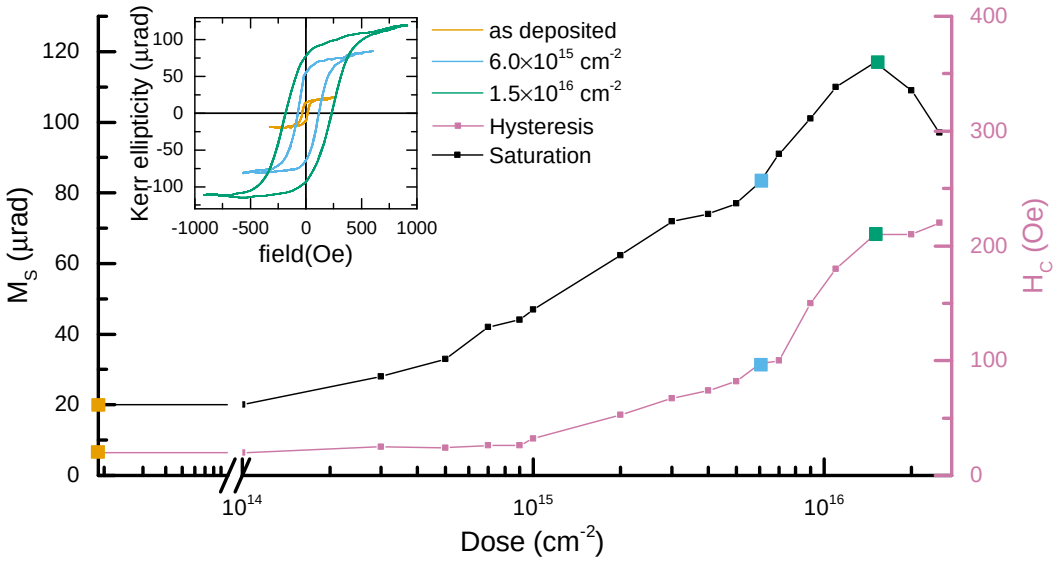

Figure 6.5 | Dependence of the magnetic saturation (M_S) and coercivity (H_C) on the 4 keV Ar^+ ion dose for 8 nm $Fe_{78}Ni_{22}$/C(100)#9 measured in-situ by longitudinal SMOKE. The inset shows hysteresis curves for as-deposited film (yellow), slightly transformed film (blue) and a film with maximal M_S (green).

lines.

Figure 6.6 portrays the circular areas irradiated by the Ga^+ ions measured by SEM. We observed a change of magnetic saturation with the ion dose, shown in Figure 6.6(a). The as-deposited film (black line) shows a very low magnetic hysteresis (close to noise level) and the highest M_S is achieved after irradiating the metastable film with 5×10^{15} cm^{-2} (red line). Increasing the dose even further leads to a decrease in the M_S, as shown by the green line. The SEM image in Figure 6.6(b) shows a brightness difference dependent upon the ion dose, where the irradiated areas are darker than the as-deposited metastable film.

6.4.2 Discussion

The ferromagnetic signal on the as-deposited films shown in Figure 6.5 means that some areas of the film grew in the stable bcc state. SMOKE is a sensitive method for the measurement of any bcc Fe, even though there is no trace of bcc in LEED. We expect that the bcc areas are between the fcc islands and most probably occur

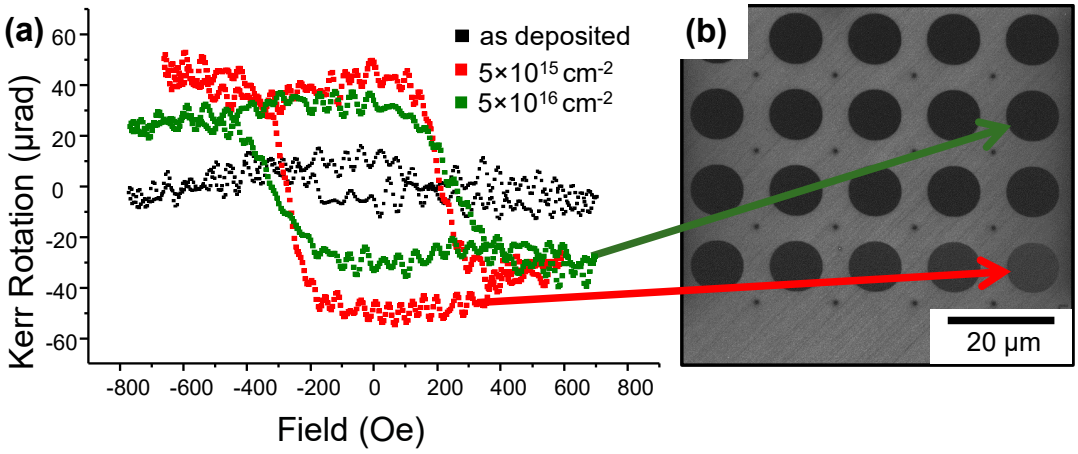

Figure 6.6 | (a) µMOKE measurement of 3 μm circles produced by 30 keV Ga^+ FIB in $Fe_{78}Ni_{22}$/C(100)#4; black is the signal on non-irradiated areas, green is irradiated with 5×10^{16} cm^{-2} and red is having highest M_S after irradiating with 5×10^{15} cm^{-2}. (b) SEM image of the irradiated areas (dark). Measurement points of µMOKE are marked with arrows.

in places where the epitaxial growth is not energetically favourable, which might be either in regions with higher graphite content or in regions with a large corrugation, where the strain induces a spontaneous bcc growth. The corrugation might also arise from the step height of diamond, which is half of the step height of Fe and cannot be accommodated by the Fe lattice. Also, we collect the SMOKE signal over a large area, which might have some defects from polishing which are not a substrate favourable for the growth of the metastable films. We managed depositing a film on C#8 with no ferromagnetic signal. This might support the explanation that the cleanliness and corrugation of the substrate is crucial for the number of transformed areas.

In case of 4 keV Ar^+ ion beam irradiation, the magnetization of the $Fe_{78}Ni_{22}$ film increases above an ion dose of 10^{14} cm^{-2} and the film is completely transformed at an ion dose between 1 and $2{\times}10^{16}$ cm^{-2}, which is two times higher than for $Fe_{78}Ni_{22}$/Cu(100). We attribute the decrease in M_S above the dose of 10^{16} cm^{-2} to sputtering of the ferromagnetic material, which we already observed on $Fe_{78}Ni_{22}$/Cu [32] and $Fe_{78}Ni_{22}$/Cu/Si [41].

For both 4 nm and 8 nm films, the M_S is approximately 2.5 times lower in comparison to the maximum M_S on the CO-stabilized 4 nm/Cu(100) [27] and 4 times lower

than 8 nm $Fe_{78}Ni_{22}$/Cu(100) [32]. It is surprising that the M_S of the completely transformed films does not increase with the thickness of the films. One of the reasons might be the diffusion of C into Fe, which makes part the film stable γ-Fe. The diffusion of C depends on the square root of time, and since the thicker films are kept at the higher temperature for a longer time, the C might stabilize a thicker proportion of the film. This would also explain why the maximal M_S is only 1/4 of the one on Cu and why the ion dose necessary for the full transformation is $\approx 2\times$ higher than in the case of $Fe_{78}Ni_{22}$/Cu(100).

The coercive field (H_C) in Figure 6.5 shows a completely different behaviour with respect to the metastable films on Cu(100) [41] up to the point of a complete transformation. In the case of $Fe_{78}Ni_{22}$/Cu(100), we argued that the increase in H_C with ion dose occurs because of the increase in the size of the bcc nuclei, which then reach a critical size, above which there are multiple ferromagnetic domains in the nuclei. This then decreases the H_C above certain dose, and it stays then constant, even though the ferromagnetic material is sputtered off. This is not the case for the $Fe_{78}Ni_{22}$/C(100), where the H_C increases gradually with the ion dose and remains constant at its maximum, even though the M_S starts to decrease. We assume this is because of a shape anisotropy of the islands of $Fe_{78}Ni_{22}$/C(100), which are visible in STM and SEM. With an increasing ion dose, the bcc areas in the fcc islands increase in size, until the whole $Fe_{78}Ni_{22}$ islands are transformed into the bcc phase, at which point the H_C is governed by the shape anisotropy.

The SEM in Figure 6.6(b) shows a brightness difference because of a change in work function in the irradiated and non-irradiated areas and a different channelling of electrons in areas with a different crystallography, as was already discussed in Section 5.5.2.

The character of the 4 nm and 8 nm thick films as measured by SMOKE, LEED and AES has been very similar, and the $Fe_{78}Ni_{22}$ formed islands thicker than the 8 nm. We, therefore, assume that it is possible to grow also thicker metastable films on diamond.

6.5 Conclusion

We showed that it is possible to deposit fcc Fe on diamond and that it is possible to prepare a graphite-free diamond surface in UHV. The cleaning of diamond with atomic H is possible also after sputtering and thus allows to recover the phase purity by *in-situ*-only treatment of diamond. The metastable films were grown on diamond by depositing $Fe_{78}Ni_{22}$ alloy at 450°C in a CO atmosphere which results in island (Volmer-Weber) growth. We showed we can tune the magnetic saturation of these with the ion dose. The metastable films allow for a one-step fabrication of ferromagnetic nanostructures by focused ion beam on a new, transparent and non-conductive substrate. We hope this opens a way for the use of, e.g., magnetic transmission x-ray microscopy for the measurement of periodically structured magnetic nanostructures (magnonic crystals) in the metastable films on diamond.

In the future, we would like to investigate the shape of the C peak in AES, which changes with thickness and temperature-treatment of the layers. This might give more information about the intermixing of Fe and C. It might also be possible to obtain some information from MFM measurements with a hard-magnetic tip to measure the out-of-plane magnetization of the metastable films before and after the ion-beam-induced transformation. The hard magnetic tip should affect the soft-magnetic $Fe_{78}Ni_{22}$ and thus make any magnetization measurable by MFM. The aim would be to measure the magnetic signal in the grooves between the islands. In case that there would be no magnetic signal, it will confirm that there is a stable paramagnetic layer underneath the metastable islands.

Another option to shine more light on the Fe-C intermixing is to use the X-ray diffraction (XRD), even though it is a technique to measure bulk materials. Reciprocal space mapping in XRD might show whether there is a new iron carbide phase forming at the higher temperature. Transmission electron microscopy combined with electron energy loss spectroscopy (EELS) should help us identify the new phase; signal from EELS should differ for areas with a different C concentration and $Fe_{78}Ni_{22}$ density. We could use other diamond samples with a larger miscut (collaboration with Augsburg)

which results in step-bunching and large terraces at the same time. B-doping should allow us to measure STM from the very beginning of the $Fe_{78}Ni_{22}$ growth and thus understand the growth mechanism.

Chapter 7

Metastable Films on $SrTiO_3(100)$

7.1 Introduction

Strontium titanate $SrTiO_3(100)$ is a perovskite oxide important for a wide range of applications in, e.g, photocatalytic water-splitting [105] and formation of two-dimensional electron gases at its surfaces [106]. $SrTiO_3(100)$ is compatible with current microelectronic technology because it grows epitaxially on the commonly used substrate Si(100) [107]. It is a potential substrate for the growth of the metastable films because of a similar lattice constant with respect to Cu and Fe.

$SrTiO_3(100)$ is commonly prepared by etching in hydrofluoric acid (HF), which results in a surface with well-defined crystallographic properties [108]. It has been shown that it is possible to have even more well-defined surfaces by etching in buffered-HF (BHF) and consequent annealing in UHV [109]. In-situ preparation, which includes only sputter-anneal cycles, leads to surface reconstructions because of preferential sputtering of the constituents. For the growth of the metastable $Fe_{78}Ni_{22}$ films, we decided to use a Cu (a=3.615 Å) buffer layer. The Cu should grow epitaxially on $SrTiO_3(100)$ (a=3.905 Å, 8% lattice mismatch) and it should wet the surface when deposited by pulsed laser deposition (PLD) [35]. Thus, an epitaxial and continuous Cu(100) buffer layer could serve as a substrate for the epitaxial growth of the metastable films.

The continuous layer-by-layer (Frank van der Merwe) growth of metals on oxides is not favourable close to thermal equilibrium because of the lower surface energy of the underlying oxide with respect to the one of the metallic film. The surface energy of Cu is 2.09 J/m^2 (0.85 eV/atom) [91] and (2×2) reconstructed TiO_2 on the HF-etched $SrTiO_3$(100) has 1.57 J/m^2(0.38 eV/atom) [110]. Such a surface energy difference commonly leads to dewetting of the Cu buffer layer which then rather follows an island (Wolmer-Weber) growth mode [111] (see Section 2.5 for details).

Deposition of many atoms in time (instantaneous flux, F), which is much shorter than the time the atoms need to diffuse to the next island (diffusion, D) results in a diffusion-limited growth. The consequence of a diffusion-limited growth (i.e. of a very low D/F ratio) is that the growing islands will be smaller. Diffusion-limited growth can lead to a layer-by-layer growth mode because the landing atoms will form small islands instead of diffusing to the nearest island and ascending on top of it. PLD provides extremely high instantaneous flux while keeping comparable time-averaged growth rates as MBE (for more details, please refer to Section 2.6).

We performed experiments on $SrTiO_3$(100) to reproduce the growth of a Cu(100) epitaxial buffer layer published in [35]. After this, we increased the deposition temperature to support the epitaxial growth and then tested the three-step approach, which proved to be the most robust one. Finally, we deposited Cu on an $SrTiO_3$(100) prepared only in UHV by sputter-anneal cycles to avoid the possibility of contamination by fluorine because the HF-etching results in F-contamination [112]. We did not manage to prepare a buffer layer appropriate for the growth of the metastable films.

7.2 Preparation of the $SrTiO_3$(100) surface

The experiments were performed in the PINUP and SPECS chambers described in sections 3.1 and 3.3, respectively. We studied two ways of substrate preparation: firstly, it was chemical treatment followed by annealing in UHV and secondly the whole treatment was conducted in UHV. An overview of the samples used with

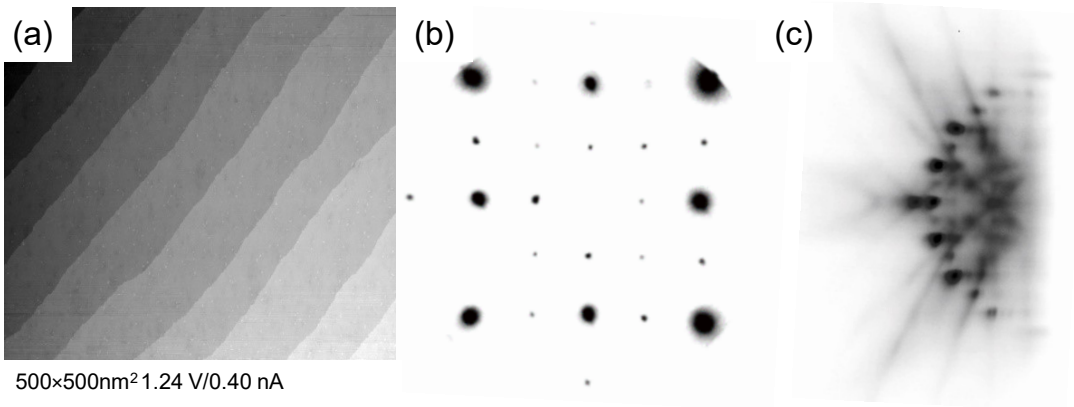

Figure 7.1 | Structural analysis of an etched and annealed $SrTiO_3(100)$ #1. (a) in STM, the teraces are approx. 50 nm wide. (b) LEED shows that the $SrTiO_3(100)$ exhibits a (2×2) reconstruction with a clear RHEED pattern with Kikuchi lines portrayed in (c).

relevant results is in Appendix A.2. The samples we used were niobium doped (0.05 wt.%) $SrTiO_3(100)$ purchased from MaTecK Company, Germany, with dimensions $5\times5\times0.5mm^3$.

The chemical preparation consisted of ex-situ etching in BHF and in-situ annealing according to Shimizu et al., which results in a TiO_2-terminated surface [109]. The resulting surface of the chemical substrate preparation showed approx. 50-nm-wide terraces in STM [Figure 7.1(a)]. LEED in Figure 7.1(b) shows weak (2×2) reconstruction spots and confirms the atomic organization of the surface. In RHEED [Figure 7.1(c)] we can observe diffraction spots and Kikuchi lines. Substrates prepared in this way did not have any contamination and a typical XPS spectrum is shown in Figure 7.6.

The data from Figures 7.1 and 7.6 show that the chemical preparation of the $SrTiO_3(100)$ leads to a clean substrate with well-defined crystallographic properties. Such a substrate should be a good candidate for the growth of the Cu buffer layer, as described by Francis et al. [35].

The UHV-preparation consisted of sputter-anneal cycles, where the annealing followed the recipe of Shimizu et al. [109]. The substrates prepared in UHV by sputter-anneal cycles had a flat and reconstructed surface; Figure 7.2(a) and (b) shows the (6×2) reconstruction in LEED and RHEED, respectively. The reconstruction changed with changes in the parameters of the sputter-anneal cycles, but we do not attempt

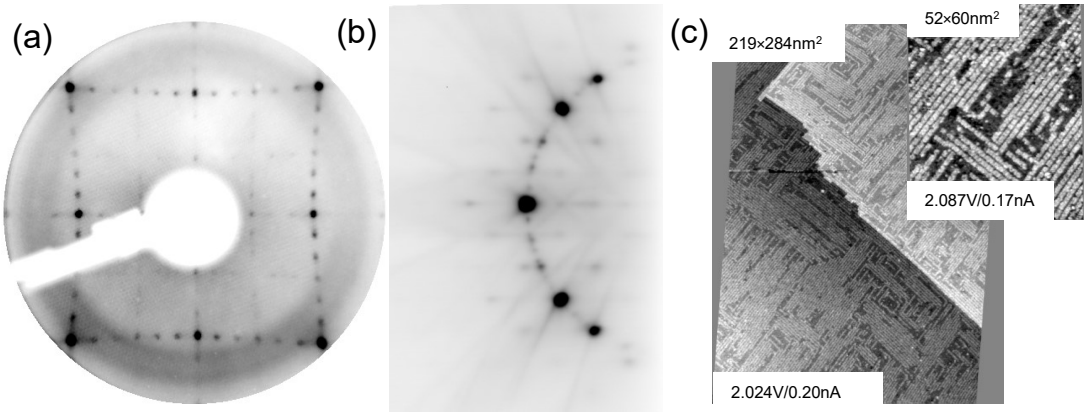

Figure 7.2 | UHV-preparation of $SrTiO_3$(100) by 2 sputter-anneal cycles. (a) LEED at 100 eV shows a (6×2) reconstruction. (b) RHEED portrays well-defined diffraction spots with a Kikuchi pattern. (c) STM shows rows perpendicular to each other. STO#12

to give an exhausting description of this phenomenon because it was published elsewhere [113]. RHEED shows the Kikuchi lines, which were already observed on the chemically treated $SrTiO_3$(100) shows in Figure 7.1(c); they confirm a flat crystalline surface. Figure 7.2(c) shows STM images of the $SrTiO_3$(100) surface, with protruding rows along the in-plane low-index directions of $SrTiO_3$(100) . The lines in STM correspond to a SrO-reconstruction because sputtering leads to a Sr-rich surface. The reason for this is that Ti (atomic mass 48) is preferentially sputtered by Ar^+ in comparison to Sr (atomic mass 88).

The UHV-prepared substrate might as well be a good template because of the rows shown in STM [Figure 7.2(c)], which might stabilize the epitaxial growth of Cu(100).

7.3 Deposition of the Cu(100) buffer layer

We deposited the Cu buffer layer on both the chemically and UHV-prepared samples. We performed three types of depositions on the chemically prepared samples. Firstly, we deposited the whole film at 100 °C and then post-annealed it to repeat the first experiment reported by Francis et al. [35] who reported the growth of epitaxial and flat Cu films. Secondly, we deposited the whole film at 300 °C to promote the epitaxial growth. Finally, we repeated the three-step process, in which we deposited a seed

Reference	A.J. Francis et al. [35]	This work
laser	Compex 201 laser	COMPexPro 205F
manufacture	Lambda Physik	Coherent
wavelength	248 nm	248 nm
pulse duration	20 ns	20 ns
pulse rate	3 Hz	3 Hz
laser energy density	8.0 J cm^{-2}	7.2 J cm^{-2}
target-to-substrate	60 mm	60 mm
ablation time	5 mins	15 mins
growth rate	4×10^{-3} nm/pulse	4×10^{-3} nm/pulse
growth time	60 mins	60 mins
no. of pulses	11 000	11 000
Ar pressure	1.3×10^{-2} mbar	1.0×10^{-1} mbar

Table 7.1 | Comparison of the PLD parameters used in the depositions by Francis [35] and presented in this chapter.

layer at 300 °C, then continued with the deposition of a thicker film at 100 °C, which was then post-annealed. On the UHV treated samples, we performed only the most robust, three-step deposition.

The AFM measurements in Figures 7.3 and 7.4 were performed using an Asylum Research Cypher setup measuring in tapping mode. The thickness of the films was estimated from the AFM measurement of the holes marked in Figure 7.4(e,f). A comparison of the parameters used in the depositions done by Francis and presented here are shown in Table 7.1. The laser energy density (L) was calculated from the formula:

$$L = \frac{\text{pulse energy} \times \text{Transmission}}{\text{Area}} = \frac{79.7\,\text{mJ/pulse} \times 0.92}{0.60 \times 1.53\,\text{mm}^2} = 7.2\ \text{J cm}^{-2} \tag{7.1}$$

7.3.1 Results

Figure 7.3 shows the results from the deposition of the Cu film at 100 °C. The as-deposited film is polycrystalline, as shown by the rings in RHEED in Figure 7.3(a). We could not observe any intensity oscillations in RHEED, and we therefore cannot define precisely the thickness of the Cu buffer layer, even though we used very similar

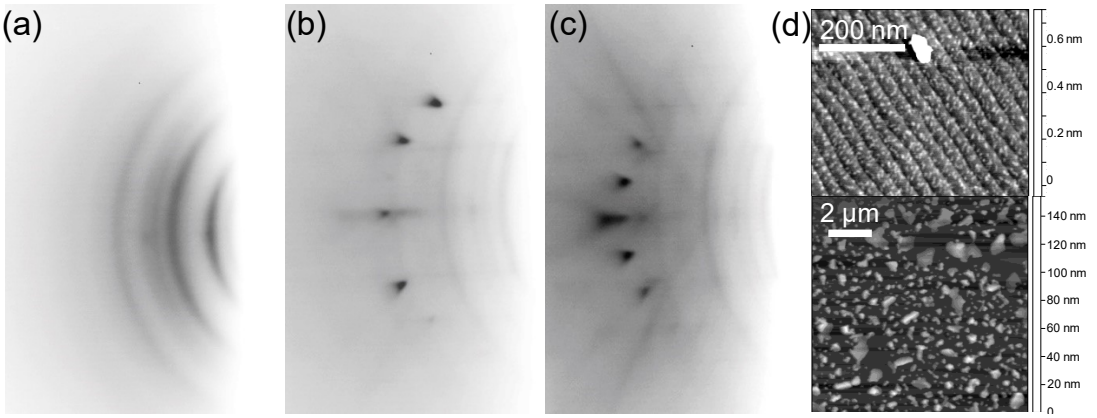

Figure 7.3 | RHEED and AFM analysis of 40 nm Cu deposited on $SrTiO_3(100)$ #1 at 100 °C. Beam incident along $SrTiO_3$ [001]. (a) The as-deposited film is polycrystalline, as shown by the circles. (b) After annealing for 10 min at 300 °C, some diffraction spots are visible. (c) After annealing 60 min at 500 °C, more pronounced diffraction spots and Kikuchi lines are visible. (d) ex-situ AFM after post-annealing shows the disconnected Cu islands. The upper image shows an area between the islands, which is the $SrTiO_3(100)$ substrate with periodic terraces already measured by STM, see Fig. 7.1(a).

parameters to Francis [35]. Post-annealing at 300 °C decreases the intensity of the polycrystalline rings and lets diffraction spots appear. Prolonged post-annealing to 500 °C does not seem to decrease the intensity of the polycrystalline rings, but it is possible to see diffraction maxima to appear with higher intensity alongside the Kikuchi lines in Figure 7.3(c). Ex-situ AFM marked in Figure 7.3(d) shows islands with a maximum height of 150 nm.

Deposition at 300 °C shown in Figure 7.4(a) leads to a diffraction pattern with diffraction maxima and polycrystalline circles as well as the presence of periodic spots in the direction orthogonal to the sample surface. This is consistent with the growth of some epitaxial 3D islands on the surface. LEED at 80 eV in Figure 7.4(b) shows two different diffraction maxima, with a 8% difference in the spot-to-spot distance. These were not visible at 100 eV [Figure 7.4(c)]. An AFM analysis of the surface showed that Cu grew in islands with randomly distributed holes. From the depth of the hole, we can assume that the thickness of the layer is more than the 30 nm.

Figure 7.5(a) shows the RHEED after the three-step deposition. The first step was the deposition of a 10-nm-thick Cu seed layer at 300 °C, which was followed by depos-

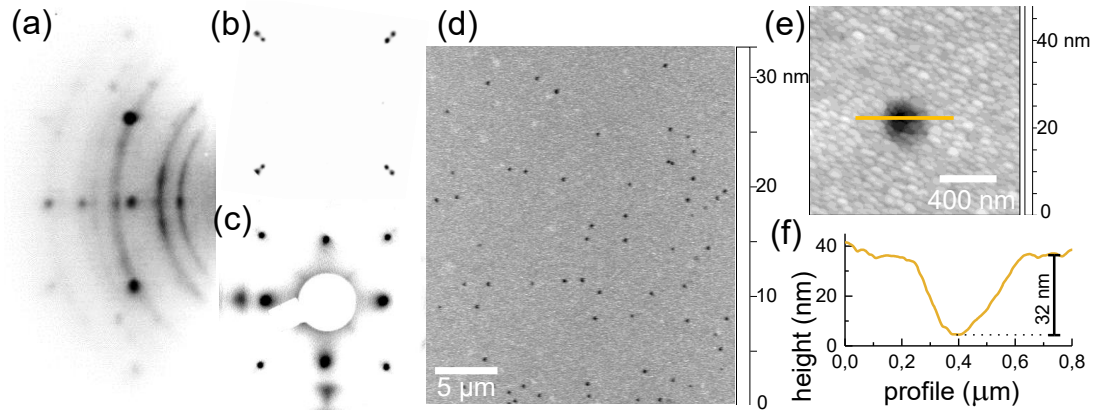

Figure 7.4 | RHEED, LEED and AFM analysis of 40 nm Cu/$SrTiO_3$(100) #3 deposited at 300 °C. The as-deposited film is partly epitaxial with some polycrystalline content, as shown by the circles. LEED at 80 eV and (c) 100 eV shows lattices with two different atomic distances are present after the deposition. (d) *Ex-situ* AFM after post-anneal shows the Cu islands. (e) AFM detail of one of the pits. (f) A height profile of the pit shows that it is approx. 32 nm deep.

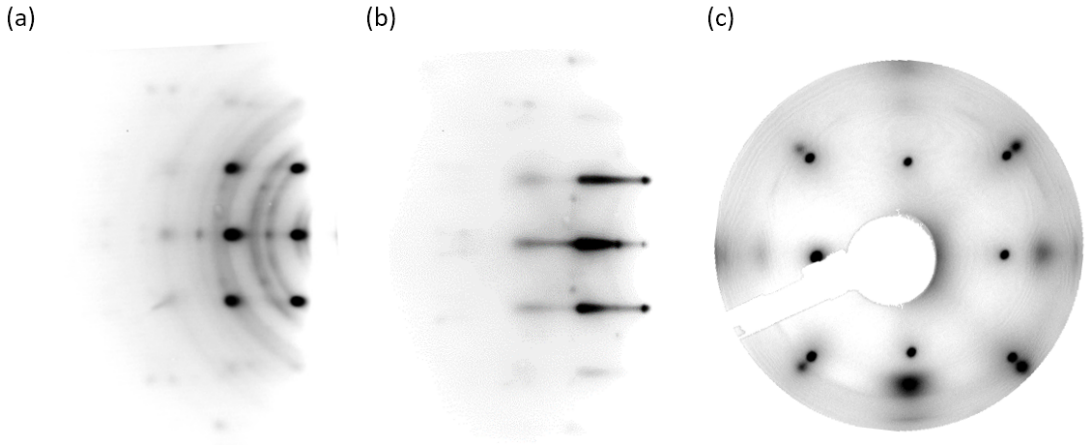

Figure 7.5 | Analysis of 40 nm Cu on $SrTiO_3$(100) #6 deposited in the three-step approach. (a) RHEED on the whole film deposited at 100 °C. (b) RHEED after post-annealing to 300 °C. (c) LEED at 100 eV after post-annealing at 300 °C shows lattices with two different atomic distances are present after the deposition.

ition of 30 nm Cu at 100 °C. The third step was the post-annealing of the whole film. Post-anneal of the as-deposited film at 300 °C leads to elongated RHEED spots shown in Figure 7.5(b). The LEED image of the post-annealed surface shows the double spots already observed in Figure 7.4(b) after deposition at 300 °C with a difference in the spot distance of 8.9%. Corresponding AFM (data not shown) gave results similar to the ones in Figure 7.4(d). The RHEED and LEED after deposition and post-annealing in Figures 7.4 and 7.5 are different. The RHEED diffraction spots in Figure 7.5(b) are elongated, which we could not observe in Figure 7.4. However, a three-dimensional periodicity with spots in the direction orthogonal to the sample surface is visible also in this case, suggesting that the film follows the island growth mode. Similarly, LEED at 100 eV in Figure 7.4 did not show the diffraction spots from both the substrate and the Cu islands, as is the case in Figure 7.5 after the three-step deposition.

The XPS measurement in Figure 7.6 shows the spectra from a clean $SrTiO_3(100)$ substrate (black line), a polycrystalline Cu film deposited at 100 °C (orange line) and the Cu film after post-annealing to 300 °C (blue line) and corresponds to the experiment marked in Figure 7.3. We can see that the cleaned $SrTiO_3(100)$ after annealing is completely free of any contamination. The Cu film deposited at 100 °C has a slight signal from Sr and Ti. After annealing at 300 °C, the signal from both Sr and Ti are more pronounced, consistently with the dewetting observed in AFM. We considered the 3D morphology of the film resulting from the growth on HF-etched $SrTiO_3(100)$ inadequate for the subsequent growth of the metastable films.

Figure 7.7(a) is a RHEED image of the 40-nm-thick seed layer grown at 100 °C on a UHV-prepared (sputtered and reconstructed) $SrTiO_3(100)$ substrate, and subsequently post-annealed to 300 °C. The pattern shows a combination of diffraction spots in direction perpendicular to the surface suggesting 3D growth and polycrystalline rings. LEED in Figure 7.7(b) on the same layer shows only one set of diffraction spots which is consistent with the ones from the $SrTiO_3(100)$ substrate. XPS on the post-annealed film showed a signal from $SrTiO_3(100)$. Finally, we deposited a ≈400 nm Cu film on the seed layer and this resulted in the fcc (111) orientation, as shown in

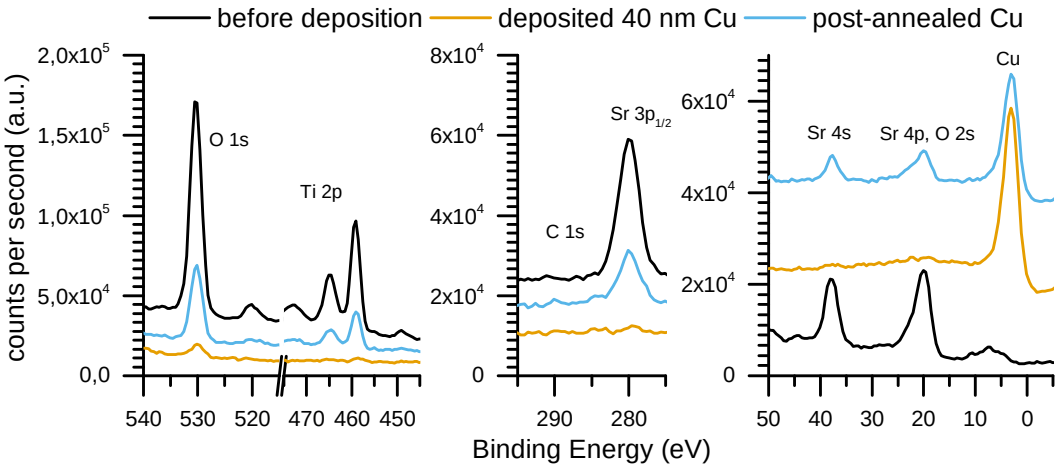

Figure 7.6 | XPS on $SrTiO_3$(100) #1 of the first experiment, in which we deposited 40 nm Cu at 100 °C and post-annealed at 300 °C (Figure 7.3). The $SrTiO_3$(100) (black line) is clear of any contamination, and the substrate is nearly completely covered by Cu after the deposition at 100 °C (orange line). The Sr, Ti and O peaks become clearly visible after post-annealing to 300 °C (blue line).

Figure 7.7(c,d). RHEED [Figure 7.7(c)] after the deposition of the whole layer and post-annealing shows elongated diffraction spots, but they have a different shape than the ones in Figure 7.5(b). LEED in Figure 7.7(d) on the same film shows a polycrystalline ring with 12 brighter areas, which are characteristic for an fcc (111) polycrystal with preferred growth directions. The XPS did not show any signal from the $SrTiO_3$.

7.3.2 Discussion

The deposition at 100 °C results in a polycrystalline Cu film as shown by RHEED [Figure 7.3(a)]. This means that the film growth is kinetically limited because the lower surface energy of oxide with respect to the metal should lead to an island growth and the 8% lattice mismatch should allow epitaxial growth. Post-annealing then leads to dewetting of the film, which is confirmed by the spots, which are very similar to those of the pristine STO substrate in the RHEED and the AFM of Cu islands [Figure 7.3(c,d)].

Films deposited at 100 °C are polycrystalline, and based on our data, we cannot exclude that some parts of the film deposited at 100 °C are epitaxial, but these would

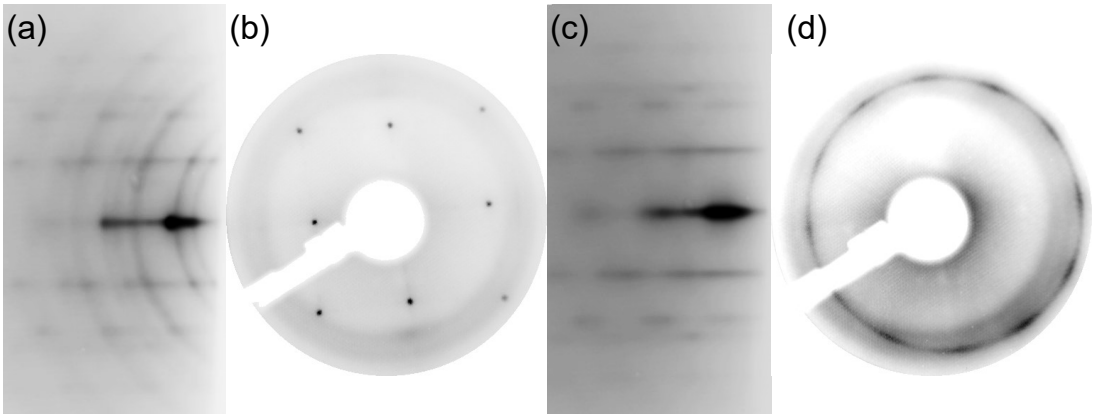

Figure 7.7 | Cu on sputter-anneal prepared $SrTiO_3$(100) #13. (a) RHEED and (b) LEED at 120 eV of 40 nm Cu grown at 100 °C after a 10 min post-anneal at 300 °C, which previously led to a removal of the polycrystalline rings [7.3(b)]. (c) RHEED and (d) LEED at 130 eV of 400 nm Cu after a 10 min post-anneal at 300 °C.

form a minority not detectable by RHEED. This is in contrary with the claim of Francis, who reported based on XRD and AFM that the Cu film is flat and epitaxial when grown at 100 °C [35]. We think the XRD presented by Francis does not give a sufficient structural analysis because it does not attribute for polycrystalline parts of the film.

In our case, it is necessary to deposit at a higher temperature to approach the thermal equilibrium and achieve the epitaxial growth.

Deposition at 300 °C leads to an epitaxial growth [Figure 7.4(a-c)] but also allows the de-wetting, i.e., the formation of Cu islands [Figure 7.4(d)]. This means that at this temperature the film grows close to the thermal equilibrium because the more energetically favourable $SrTiO_3$(100) surface is exposed and the Cu agglomerates into the epitaxial islands. The use of PLD imposes a kinetic limitation on the growth because the very low D/F ratio leads to island nucleation and formation of smaller islands close to each other. This kinetic limitation should then promote the 2D rather than 3D island formation even at elevated temperatures (e.g. 300 °C) because it would be easier for the islands to coalesce. We see, however, that this is not the case. Therefore, it seems that there is not a single temperature region at which the films are flat and at the same time epitaxial, as was claimed by Francis. We assume that the slight dif-

ference in our laser fluence and pressure with respect to Francis did not dramatically change the behavior of the system.

Finally, we followed the three-step method shown by Francis because it allowed for the growth of epitaxial films in systems, which would not grow flat and epitaxial at any single temperature. The as-deposited film on the seed layer was polycrystalline [rings in Figure 7.5(a)]. Figure 7.5(b,c) shows that the post-annealing of the polycrystalline film deposited on the epitaxial seed layer leads to de-wetting of the film, which forms epitaxial islands, similar to the growth at 300 °C. The indication of this comes from the double spots in Figure 7.5(c). The RHEED and LEED patterns after the three-step approach are not identical with the deposition at 300 °C. The spot-to-spot distance in LEED which is different by ≈8% confirms the lattice mismatch between the $SrTiO_3$(100) and Cu(100). At the same time, the Cu film seems to be fully relaxed, although maintaining the epitaxial relation with the substrate. The spot-to-spot distance is similar to the one in Figure 7.4(b). The seed layer of Cu(100) therefore does not help to grow the epitaxial Cu buffer layer.

Cu films deposited on the UHV-prepared $SrTiO_3$(100) do not grow in the (100) orientation. Figure 7.7(c,d) shows the results of the three-step deposition of 400 nm Cu but at these conditions we can see that Cu grows exposing {111} oriented facets parallel to the surface, instead of the expected (100) surface. The period of the spots in Figure 7.7(a) and (c) is similar, which suggests that there already was a fraction of the {111}-oriented Cu in the 40-nm-thick Cu seed layer. We assume the resulting 400 nm Cu film organized into the most stable Cu(111) because the surface reconstructions of the substrate did not allow for epitaxial growth. Consequently, the Cu grew in the more stable Cu(111) because it has a lower surface energy [91, 114].

Deposition of the $Fe_{78}Ni_{22}$ film at RT directly onto the $SrTiO_3$(100) prepared in UHV resulted in a ferromagnetic signal in MOKE, i.e., the film grew in the bcc phase. We did not expect that it would be possible to grow the metastable films directly on $SrTiO_3$(100) either by PLD or by MBE. The first reason is that it might be impossible to deposit these films by PLD because the plasma produced during the heating of

the target material contains ions which can hit the substrate. These ions would then cause an ion-beam-induced transformation and the films would grow as stable bcc $Fe_{78}Ni_{22}$. The deposition by evaporation does not allow for epitaxial growth, because the 8% lattice mismatch between Fe and $SrTiO_3(100)$ leads to a very low critical thickness, which would result in dislocations which could be nuclei for a spontaneous transformation of the film into the stable bcc phase.

7.4 Conclusion

We could not confirm that PLD is a method for the growth of epitaxial Cu on $SrTiO_3(100)$, even though Francis concluded based on XRD and AFM that the Cu films are epitaxial and flat [35]. In our experiments, the growth of the epitaxial films required deposition/post-annealing at high temperatures which led to dewetting of the Cu film, i.e., it had to get close to thermal equilibrium in order to be epitaxial. The growth of the metastable films directly on $SrTiO_3(100)$ is also not possible. Therefore, we could not use $SrTiO_3(100)$ as a substrate for the growth of the metastable films.

Chapter 8

Summary and Outlook

We investigated the growth and properties of the metastable iron-nickel thin films on three substrates: Cu(100) in Chapter 4, Cu/Si(100) in Chapter 5 and C(100) in Chapter 6. Attempts to grow these films on Cu/$SrTiO_3$(100) were not successful (Chapter 7).

Growth on Cu(100) is a model system, which has been used to tune the Ni content and CO backpressure during the growth of the metastable films [32, 33]. We showed that such metastable films allow ferromagnetic nanopatterning and we could tune not only the magnetic saturation but also the magneto-crystalline anisotropy by irradiation with a focused ion beam (FIB) [40]. Linear scanning of the FIB fabricates bcc(100) domains with easy axes (in [001] directions) parallel to the FIB scanning direction. Tuning of the anisotropy makes it possible to have different directions of the easy axis within one ferromagnetic structure. The size limit of the microstructures is the size of the bcc needle-like nuclei (approx. 100 nm), which form upon ion-beam transformation [27]. For the ion-beam-induced transformation, we used Ga^+ and Ar^+ ions, and they exhibited different transformation efficiency. According to the SRIM calculations, we confirmed that this comes from the energy transferred to the recoils in the metastable films and the intermixing at the $Fe_{78}Ni_{22}$-Cu interface. Defining the properties of the metastable films on the Cu(100) gave us a better understanding of the $Fe_{78}Ni_{22}$ system which we used on the other substrates.

We then investigated the $SrTiO_3$(100) and Si(100) with an epitaxial Cu(100) buffer layer as potential alternatives to the Cu single crystal. In the first case, we were not able to prepare a flat and epitaxial Cu(100) buffer layer, in contrast to what was reported by Francis et al. [35]. On the other side, Si(100) proved to be a good substrate for the growth of the buffer layer and we showed that it is possible to transfer the nanofabrication from an expensive Cu(100) single crystal to an application-friendly Si(100) substrate [41]. We therefore moved the metastable films to a cheaper substrate, which is a significant step towards the fabrication of soft ferromagnetic nanostructures on an industrial scale.

Broadband ferromagnetic resonance (FMR) and Brillouin light scattering (BLS) measurements were performed to quantify the magnetization and magnetic damping of the completely transformed metastable films by a Ga^+ ion beam (see Table 8.1). For a description of the FMR measurements, please refer to [67]. The extremely large error bars in FMR measurements suggest that the FMR is not an ideal technique for the measurement of the ferromagnetic thin films. The BLS measurements, however, allowed for a well-defined quantification of the magnetization of the transformed $Fe_{78}Ni_{22}$ films. The FMR and BLS measurements in the Table 8.1 indicate that the $Fe_{78}Ni_{22}$ films on Cu(100) single crystal and Cu/Si(100) are superior to permalloy in terms of magnetization $\mu_0 M_S$ and Gilbert damping α. At the same time, the nanopatterning of the metastable films requires only FIB irradiation, which is technologically more convenient than the multi-step lithography necessary for the fabrication of the permalloy nanostructures.

The last substrate, C(100), is not an economically more interesting substitute for the copper single crystal, but the growth of the metastable films on this substrate enables new methods of studying of the ferromagnetic nanopatterns. Such an approach can lead to applications in magnonics, where an insulating and transmissive substrate permits laser excitation of magnons in the metastable film through the substrate. The availability of thin diamond nanomembranes (e.g. from Diamond Materials GmbH, Freiburg, Germany) enables the characterization via, e.g., magnetic transmission x-

sample	thickness	$\mu_0 M_S$ magnetization	$\gamma/(2\pi)$ gyromagnetic ratio	α Gilbert damping
	nm	T	GHz/T	$\times 10^{-3}$
$Fe_{78}Ni_{22}$/Cu/Si(100)	8	$1.8 \pm 1.5^*$	28.5 ± 1.6	8.79 ± 0.27
$Fe_{78}Ni_{22}$/Cu(100)	8	$1.2 \pm 0.9^*$	26.0 ± 1.0	8.84 ± 1.1
Fe/Si(100)	8	1.6 ± 0.6	28.9 ± 0.5	12.4 ± 1.0
permalloy/Si(100)	8	0.86 ± 0.31	29.5 ± 0.5	14.0 ± 1.3
$Fe_{78}Ni_{22}$/Cu(100)†	10	1.97 ± 0.05	28^{**}	–

Table 8.1 | Broadband FMR and BLS measurements of the transformed metastable films and permalloy. The $Fe_{78}Ni_{22}$ films were transformed completely into bcc by ion beam. The Fe/Si(100) grew in the bcc phase. *large error in M_S does not allow a sound quantification of the data. The FMR measurements were performed by Viola Krizakova and the table is adapted from [67]. †BLS measurements were performed on FIB-made spin waveguides and analyzed by Lukas Flajsman. **The $\gamma/(2\pi) = 29\,GHz/T$ was used for fitting of the spin wave dispersion model.

ray microscopy.

The experiments on C(100) and Si(100) led to a design and fabrication of equipment for hydrogen termination and direct current heating. The hydrogen cracker was used for H-termination of Si and for cleaning of C(100). This approach facilitates UHV-only preparation of both C(100) and H-Si(100) for the epitaxial growth, which was not used in the past. The growth of the epitaxial Cu buffer layer on the UHV-prepared H-Si(100) is a new method, which was enabled by stabilization of the Cu(100) by calcium. These methods extend the range of experimental approaches for the preparation of the metastable films on the new substrates.

We propose in the following investigations to tune the deposition parameters of $Fe_{78}Ni_{22}$ on the substrates which support the growth of the metastable films. Firstly, Cu(100) was the only substrate on which we could tune the magneto-crystalline anisotropy by FIB and we assume that this property is connected to the CO pressure and Ni content during the deposition. We, therefore, propose to investigate the FIB-induced tuning of anisotropy for metastable films grown in different CO pressures and with a different Ni content. Secondly, the buffer layer on Si(100) supported the epitaxial growth of $Fe_{78}Ni_{22}$, but its morphology was not ideal; it might be possible

to decrease the corrugation of the buffer layer by a surfactant or a wetting layer between the Cu and Si. The effect of Ca on the stabilization of the epitaxial growth of the buffer layer warrants further investigations. Finally, increasing the thickness of the metastable films on C(100) might enable the fabrication of nanostructures with larger grains, lower corrugation and higher magnetization of nanopatterns. Also, it is not yet completely clear, whether a new phase forms at the Fe-C boundary and what is its composition and thickness.

We moved the research of metastable iron-nickel thin films from a single-crystalline Cu(100) substrate to Si(100) and C(100), which makes the metastable films more interesting both for applications and fundamental research. We further showed the fabrication of ferromagnetic microstructures in a paramagnetic matrix by FIB on these substrates and in case of Cu(100) we also tuned the magneto-crystalline anisotropy of the ferromagnetic microstructures.

References

1. Ohring, M. *Materials Science of Thin Films* 794. DOI: 10.1016/B978-0-12-524975-1.X5000-9 (Academic Press, 2002).
2. Oura, K., Lifshits, V., Saranin, A., Zotov, A. & Katayama, M. *Surface Science: An Introduction* (Springer Berlin Heidelberg, 2003).
3. Biedermann, A., Schmid, M. & Varga, P. Nucleation of bcc iron in ultrathin fcc films. *Phys. Rev. Lett.* **86,** 464–7. DOI: 10.1103/PhysRevLett.86.464 (2001).
4. Biedermann, A., Tscheliessnig, R., Schmid, M. & Varga, P. Crystallographic structure of ultrathin Fe films on Cu(100). *Phys. Rev. Lett.* **87,** 086103. DOI: 10.1103/PhysRevLett.87.086103 (2001).
5. Biedermann, A., Tscheliessnig, R., Schmid, M. & Varga, P. Local atomic structure of ultra-thin Fe films grown on Cu(100). *Applied Physics A: Materials Science & Processing* **78,** 807–816. DOI: 10.1007/s00339-003-2435-7 (2004).
6. Pescia, D., Stampanoni, M., Bona, G. L., Vaterlaus, A., Willis, R. F. & Meier, F. Magnetism of Epitaxial fcc Iron Films on Cu(001) Investigated by Spin-Polarized Photoelectron Emission. *Phys. Rev. Lett.* **58,** 2126–2129. DOI: 10.1103/PhysRevLett.58.2126 (1987).
7. Liu, C., Moog, E. R. & Bader, S. D. Polar Kerr-Effect Observation of Perpendicular Surface Anisotropy for Ultrathin fcc Fe Grown on Cu(100). *Phys. Rev. Lett.* **60,** 2422–2425. DOI: 10.1103/PhysRevLett.60.2422 (1988).
8. Ben-Menahem, A. *Historical Encyclopedia of Natural and Mathematical Sciences* DOI: 10.1108/09504121011045764 (Springer, 2009).

9. Faraday, M. The Bakerian Lecture. — Experimental relations of gold (and other metals) to light. *Phil. Trans. R. Soc. Lond.* **147,** 145–181. DOI: https://doi.org/10.1098/rstl.1857.0011 (1857).

10. Kerr, J. On rotation of the plane of polarization by reflection from the pole of a magnet. *The London, Edinburgh, and Dublin Philosophical Magazine and Journal of Science* **3,** 321–343. DOI: 10.1080/14786447708639245. eprint: https://doi.org/10.1080/14786447708639245 (1877).

11. J. Fassbender, J. M. Magnetic patterning by means of ion irradiation and implantation. *J. Magn. Magn. Mat.* **320,** 579–596 (2008).

12. Stamps, R. L., Breitkreutz, S., Akerman, J., Chumak, A. V., Otani, Y., Bauer, G. E. W., Thiele, J.-U., Bowen, M., Majetich, S. A., Klaeui, M., Prejbeanu, I. L., Dieny, B., Dempsey, N. M. & Hillebrands, B. The 2014 Magnetism Roadmap. *Journal of Physics D: Applied Physics* **47,** 333001. DOI: 10.1088/0022-3727/47/33/333001 (2014).

13. Bloch, F. Zur Theorie Des Ferromagnetismus. *Zeitschrift fuer Physik* **61,** 206. DOI: 10.1007/BF01339661 (1930).

14. Kruglyak, V. V., Demokritov, S. O. & Grundler, D. Magnonics. *Journal of Physics D: Applied Physics* **43,** 264001. DOI: 10.1088/0022-3727/43/26/264001 (2010).

15. Chumak, A. V., Vasyuchka, V. I., Serga, A. A. & Hillebrands, B. Magnon spintronics. *Nature Physics* **11,** 453–461. DOI: 10.1038/nphys3347 (2015).

16. Chumak, A. V., Serga, A. A. & Hillebrands, B. Magnonic crystals for data processing. *Journal of Physics D: Applied Physics* **50,** 244001. DOI: 10.1088/1361-6463/aa6a65 (2017).

17. Serga, A. A., Chumak, A. V. & Hillebrands, B. YIG magnonics. *Journal of Physics D: Applied Physics* **43,** 264002. DOI: 10.1088/0022-3727/43/26/264002 (2010).

18. Chumak, A. V., Pirro, P., Serga, A. A., Kostylev, M. P., Stamps, R. L., Schultheiss, H., Vogt, K., Hermsdoerfer, S. J., Laegel, B., Beck, P. A. & Hillebrands, B. Spin-wave propagation in a microstructured magnonic crystal. *Appl. Phys. Lett.* **95,** 262508. DOI: 10.1063/1.3279138. eprint: https://doi.org/10.1063/1.3279138 (2009).

19. Yu, H., Huber, R., Schwarze, T., Brandl, F., Rapp, T., Berberich, P., Duerr, G. & Grundler, D. High propagating velocity of spin waves and temperature dependent damping in a CoFeB thin film. *Appl. Phys. Lett.* **100,** 262412. DOI: 10.1063/1.4731273. eprint: https://doi.org/10.1063/1.4731273 (2012).

20. Demokritov, S. O., Hillebrands, B. & Slavin, A. N. Brillouin light scattering studies of confined spin waves: linear and nonlinear confinement. *Physics Reports* **348,** 441–489 (2001).

21. Kittel, C. On the Theory of Ferromagnetic Resonance Absorption. *Phys. Rev.* **73,** 155–161. DOI: 10.1103/PhysRev.73.155 (1948).

22. Rupp, W. *Ionenstrahl induzierter Ferromagnetismus von dünnen Fe-Schichten auf Cu(100)* Dissertation (Institute of Applied Physics, TU Wien, 2009).

23. Gustafson, P. A Thermodynamic Evaluation of the Fe-C System. *Scand. J. Metall.* **14,** 259–267 (1985).

24. Thomassen, J., May, F., Feldmann, B., Wuttig, M. & Ibach, H. Magnetic live surface layers in Fe/Cu(100). *Phys. Rev. Lett.* **69,** 3831–3834. DOI: 10.1103/PhysRevLett.69.3831 (1992).

25. Biedermann, A. Stability of the nanomartensitic phase in ultrathin Fe films on Cu(100). *Physical Review B* **80.** DOI: 10.1103/PhysRevB.80.235403 (2009).

26. Rupp, W., Biedermann, A., Kamenik, B., Ritter, R., Klein, C., Platzgummer, E., Schmid, M. & Varga, P. Ion-beam induced fcc-bcc transition in ultrathin Fe films for ferromagnetic patterning. *Appl. Phys. Lett.* **93,** 063102. DOI: 10.1063/1.2969795 (2008).

27. Shah Zaman, S., Oßmer, H., Jonner, J., Novotný, Z., Buchsbaum, A., Schmid, M. & Varga, P. Ion-beam-induced magnetic transformation of CO-stabilized fcc Fe films on Cu(100). *Phys. Rev. B.* **82,** 235401. DOI: 10.1103/PhysRevB.82.235401 (2010).

28. Kirilyuk, A., Giergiel, J., Shen, J., Straub, M. & Kirschner, J. Growth of stabilized gamma-Fe films and their magnetic properties. *Phys. Rev. B* **54,** 1050–1063. DOI: 10.1103/PhysRevB.54.1050 (1996).

29. Bain, E. C. *Functions of the alloying elements in steel* (American Society for metals, 1940).

30. Shah Zaman, S. *Ion-beam induced magnetic nano-structures of Fe grown on Cu(100)* Dissertation (Institute of Applied Physics, TU Wien, 2011).

31. Shah Zaman, S., Dvořák, P., Ritter, R., Buchsbaum, A., Stickler, D., Oepen, H. P., Schmid, M. & Varga, P. In-situ magnetic nano-patterning of Fe films grown on Cu(100). *J. Appl. Phys.* **110,** 024309. DOI: 10.1063/1.3609078 (2011).

32. Gloss, J., Shah Zaman, S., Jonner, J., Novotny, Z., Schmid, M., Varga, P. & Urbanek, M. Ion-beam-induced magnetic and structural phase transformation of Ni-stabilized face-centered-cubic Fe films on Cu(100). *Appl. Phys. Lett.* **103,** 262405. DOI: 10.1063/1.4856775 (2013).

33. Gloss, J. *Magnetic transformation of metastable fcc Fe/Cu(100) films by focused ion beam* Master Thesis (Institute of Physical Engineering, Brno University of Technology, 2014).

34. Entel, P., Hoffmann, E., Mohn, P., Schwarz, K. & Moruzzi, V. L. First-principles calculations of the instability leading to the Invar effect. *Physical Review B* **47,** 8706–8720. DOI: 10.1103/PhysRevB.47.8706 (1993).

35. Francis, A. J., Cao, Y. & Salvador, P. A. Epitaxial growth of Cu(100) and Pt(100) thin films on perovskite substrates. *Thin Solid Films* **496,** 317–325. DOI: 10.1016/j.tsf.2005.08.367 (2006).

36. Chang, C.-A. Outdiffusion of Cu through Au: Comparison of (100) and (111) Cu films epitaxially deposited on Si, and effects of annealing ambients. *Appl. Phys. Lett.* **55,** 2754–2756. DOI: 10.1063/1.101944 (1989).

37. Meunier, A., Gilles, B. & Verdier, M. Cu/Si(001) epitaxial growth: role of the epitaxial silicide formation in the structure and the morphology. *J. Cryst. Growth* **275,** e1059–e1065. DOI: 10.1016/j.jcrysgro.2004.11.132 (2005).

38. Mewes, T., Rickart, M., Mougin, A., Demokritov, S. O., Fassbender, J., Hillebrands, B. & Scheib, M. Comparative study of the epitaxial growth of Cu on MgO(001) and on hydrogen terminated Si(001). *Surf. Sci.* **481,** 87–96. DOI: 10.1016/S0039-6028(01)01000-7 (2001).

39. Han, D. S., Vogel, A., Jung, H., Lee, K. S., Weigand, M., Stoll, H., Schütz, G., Fischer, P., Meier, G. & Kim, S. K. Wave modes of collective vortex gyration in dipolar-coupled-dot-array magnonic crystals. *Sci Rep* **3,** 2262. DOI: 10.1038/srep02262 (2013).

40. Urbanek, M., Flajsman, L., Krizakova, V., Gloss, J., Horky, M., Schmid, M. & Varga, P. Research Update: Focused ion beam direct writing of magnetic patterns with controlled structural and magnetic properties. *APL Materials* **6,** 060701. DOI: 10.1063/1.5029367 (2018).

41. Gloss, J., Horký, M., Křižáková, V., Flajšman, L., Schmid, M., Urbánek, M. & Varga, P. The growth of metastable fcc $Fe_{78}Ni_{22}$ thin films on H-Si(100) substrates suitable for focused ion beam direct magnetic patterning. *Applied Surface Science.* DOI: 10.1016/j.apsusc.2018.10.263 (2018).

42. Vickerman, J. C. & Gilmore, I. S. *Surface Analysis - The Principal Techniques.* (UK: John Wiley and Sons, second ed., 2009).

43. Davis, L. E. *Handbook of Auger electron spectroscopy: a reference book standard data for identification and interpretation of Auger electron spectroscopy data* 2nd (Physical Electronics Industries, 1976).

44. Koller, R., Bergermayer, W., Kresse, G., Konvicka, C., Schmid, M., Redinger, J., Podloucky, R. & Varga, P. The structure of the oxygen-induced c(6×2) reconstruction of V(110). *Surf. Sci.* **512,** 16–28. DOI: 10.1016/S0039-6028(02)01722-3 (2002).

45. Davisson, C. & Germer, L. Diffraction of Electrons by a Crystal of Nickel. *Phys. Rev. (2nd series)* **30,** 705 (1927).

46. Qiu, Z. Q. & Bader, S. D. Surface magneto-optic Kerr effect. *Review of Scientific Instruments* **71,** 1243–1255. DOI: 10.1063/1.1150496. eprint: https://doi.org/10.1063/1.1150496 (2000).

47. Flajšman, L., Urbánek, M., Křižáková, V., Vaňatka, M., Turčan, I. & Šikola, T. High-resolution fully vectorial scanning Kerr magnetometer. *Rev. Sci. Instrum.* **87,** 053704. DOI: 10.1063/1.4948595 (2016).

48. Binnig, G. & Rohrer, H. Scanning tunneling microscopy. *Helvetica Physica Acta* **55,** 726–435 (1982).

49. Lüth, H. *Solid Surfaces, Interfaces and Thin Films* DOI: 10.1007/978-3-642-13592-7 (Springer, Berlin, Heidelberg, 2010).

50. Stranski, I. N. & Krastanov, L. Abhandlungen der Mathematisch - Naturwissenschaftlichen Klasse IIb. *Akad. Wiss. Wien* **146,** 797 (1938).

51. Gerhold, S. *Surface reactivity and homoepitaxial growth of strontium titanate (110)* PhD thesis (TU Wien, 2016).

52. Eason, R. *Pulsed Laser Deposition Of Thin Films* (John Wiley and Sons, 2007).

53. Willmott, P. R. & Huber, J. R. Pulsed laser vaporization and deposition. *Rev. Mod. Phys.* **72,** 315–328. DOI: 10.1103/RevModPhys.72.315 (2000).

54. Schmid, M., Lenauer, C., Buchsbaum, A., Wimmer, F., Rauchbauer, G., Scheiber, P., Betz, G. & Varga, P. High Island Densities in Pulsed Laser Deposition: Causes and Implications. *Phys. Rev. Lett.* **103,** 076101. DOI: 10.1103/PhysRevLett.103.076101 (2009).

55. Klein, J. *Epitaktische Heterostrukturen aus dotierten Manganaten* PhD thesis (Universität zu Köln, 2001).

56. Imanishi, N. *Interaction of ions with matter* in *Focused Ion Beam Systems: Basics and Applications* (ed Yao, N.) 31–66 (Cambridge University Press, 2007). DOI: 10.1017/CBO9780511600302.003.

57. Schilling, W. & Ullmaier, H. *Physics of radiation damage in metals* in *Materials, Science, and Technology* (eds R.W. Cahn, P. H. & Kramer, K.) 179–241 (Chemie, Weinheim, 1993). DOI: 10.1002/9783527603978.mst0113.

58. Ziegler, J. F., Biersack, J. & Ziegler, M. TRIM, computer code to calculate the stopping and range of ions in matter. DOI: 10.1016/j.nimb.2010.02.091 (2008).

59. Ashida, K., Kajino, T., Kutsuma, Y., Ohtani, N. & Kaneko, T. Crystallographic orientation dependence of SEM contrast revealed by SiC polytypes. *Journal of Vacuum Science Technology B, Nanotechnology and Microelectronics: Materials, Processing, Measurement, and Phenomena* **33,** 04E104. DOI: 10.1116/1.4927136 (2015).

60. Nagl, C., Haller, O., Platzgummer, E., Schmid, M. & Varga, P. Submonolayer growth of Pb on Cu(111): surface alloying and de-alloying. *Surf. Sci.* **321,** 237–248. DOI: 10.1016/0039-6028(94)90189-9 (1994).

61. Eibl, C., Lackner, G. & Winkler, A. Quantitative characterization of a highly effective atomic hydrogen doser. *J. Vac. Sci. & Tech. A* **16,** 2979–2989. DOI: 10.1116/1.581449 (1998).

62. Bischler, U. & Bertel, E. Simple source of atomic hydrogen for ultrahigh vacuum applications. *J. Vac. Sci. & Tech. A* **11,** 458–460. DOI: 10.1116/1.578754 (1993).

63. Donnelly, C. M., McCullough, R. W. & Geddes, J. Etching of graphite and diamond by thermal energy hydrogen atoms. *Diamond and Related Materials* **6,** 787–790. DOI: 10.1016/S0925-9635(96)00606-1 (1997).

64. Oura, K., Lifshits, V. G., Saranin, A. A., Zotov, A. V. & Katayama, M. Hydrogen interaction with clean and modified silicon surfaces. *Surf. Sci. Rep.* **35,** 1–69. DOI: 10.1016/s0167-5729(99)00005-9 (1999).

65. Oura, K., Yamane, J., Umezawa, K., Naitoh, M., Shoji, F. & Hanawa, T. Hydrogen adsorption on Si(100)-2x1 surfaces studied by elastic recoil detection analysis. *Phys Rev B* **41,** 1200–1203. DOI: 10.1103/PhysRevB.41.1200 (1990).

66. Napetschnig, E. *Thin alumina films on NiAl(110) and CuAl(111): Structure, domain boundaries and nucleation and growth of metallic clusters* PhD thesis (TU Wien, 2008).

67. Krizakova, V. *Spin wave excitation and propagation in magnonic crystals prepared by focused ion beam direct writing* Master Thesis (Institute of Physical Engineering, Brno University of Technology, 2018).

68. Chang, C.-A. Formation of copper silicides from Cu(100)/ Si(100) and Cu(111)/ Si(111) structures. *J. Appl. Phys.* **67,** 566–569. DOI: 10.1063/1.345194 (1990).

69. Vaz, C. A. F., Steinmuller, S. J., Moutafis, C., Bland, J. A. C. & Babkevich, A. Y. Structural and morphological characterisation of hybrid Cu/Si(001) structures. *Surf. Sci.* **601,** 1377–1383. DOI: 10.1016/j.susc.2007.01.001 (2007).

70. Takahagi, T., Nagai, I., Ishitani, A., Kuroda, H. & Nagasawa, Y. The formation of hydrogen passivated silicon single-crystal surfaces using ultraviolet cleaning and HF etching. *J. Appl. Phys.* **64,** 3516–3521. DOI: 10.1063/1.341489 (1988).

71. Vaz, C. A. F. & Bland, J. A. C. Strain-induced magnetic anisotropy in Cu/Co/ Ni/Cu/Si(001) epitaxial structures. *Physical Review B* **61,** 3098–3102. DOI: 10.1103/PhysRevB.61.3098 (2000).

72. Steinmuller, S. J., Vaz, C. A. F., Stroem, V., Moutafis, C., Tse, D. H. Y., Guertler, C. M., Klaeui, M., Bland, J. A. C. & Cui, Z. Effect of substrate roughness on the magnetic properties of thin fcc Co films. *Physical Review B* **76.** DOI: 10.1103/PhysRevB.76.054429 (2007).

73. Vaz, C. A. F., Steinmuller, S. J. & Bland, J. A. C. Roughness-induced variation of magnetic anisotropy in ultrathin epitaxial films: The undulating limit. *Physical Review B* **75.** DOI: 10.1103/PhysRevB.75.132402 (2007).

74. Chang, C.-A., Liu, J. C. & Angilello, J. Epitaxy of (100) Cu on (100) Si by evaporation near room temperatures: In-plane epitaxial relation and channeling analysis. *Applied Physics Letters* **57,** 2239. DOI: 10.1063/1.103902 (1990).

75. Hashim, I., Park, B. & Atwater, H. A. Epitaxial growth of Cu (001) on Si (001): Mechanisms of orientation development and defect morphology. *Appl. Phys. Lett.* **63,** 2833. DOI: 10.1063/1.110302 (1993).

76. Demczyk, B. G., Naik, F., Auner, G., Kota, C. & Rao, U. Growth of Cu films on hydrogen terminated Si(100) and Si(111) surfaces. *J. Appl. Phys.* **75,** 1956–1961. DOI: 10.1063/1.356344 (1993).

77. Zhang, J., Liu, C., Shu, Y. & Fan, J. Growth and properties of Cu thin film deposited on Si(001) substrate: A molecular dynamics simulation study. *Applied Surface Science* **261,** 690–696. DOI: 10.1016/j.apsusc.2012.08.082 (2012).

78. Krastev, E. T., Voice, L. D. & Tobin, R. G. Surface morphology and electric conductivity of epitaxial Cu(100) films grown on H-terminated Si(100). *J. Appl. Phys.* **79,** 6885. DOI: 10.1063/1.361508 (1996).

79. Lukaszew, R. A., Sheng, Y., Uher, C. & Clarke, R. Smoothening of Cu films grown on Si(001). *Appl. Phys. Lett.* **76,** 724. DOI: 10.1063/1.125874 (2000).

80. Boland, J. J. Structure of the H-saturated Si(100) surface. *Phys. Rev. Lett.* **65,** 3325–3328. DOI: 10.1103/PhysRevLett.65.3325 (1990).

81. Horky, M. *Growth of Metastable fcc Fe thin films on Cu(100)/Si(100) substrates* Master Thesis (Institute of Physical Engineering, Brno University of Technology, 2016).

82. Baker, L. A., Laracuente, A. R. & Whitman, L. J. Hydrogen termination following Cu deposition on Si(001). *Phys Rev B* **71,** 153302. DOI: 10.1103/PhysRevB.71.153302 (2005).

83. Vaz, C. A. F., Lauhoff, G., Bland, J. A. C., Langridge, S., Bucknall, D. G., Penfold, J., Clarke, J., Halder, S. K. & Tanner, B. K. Interface dependent magnetic moments in Cu/Co, Ni/Cu/Si(001) epitaxial structures. *Journal of Magnetism and Magnetic Materials* **313,** 89–97. DOI: 10.1016/j.jmmm.2006.12.008 (2007).

84. K.E. Hermann (FHI Berlin) & M.A. Van Hove (Baptist University Hong Kong). *LEEDpat, Version 4.2* http://www.fhi-berlin.mpg.de/KHsoftware/LEEDpat/index.html.

85. Shirasawa, T., Mizuno, S. & Tochihara, H. Electron-beam-induced disordering of the Si(001)-c(4x2) surface structure. *Phys Rev Lett* **94,** 195502. DOI: 10.1103/PhysRevLett.94.195502 (2005).

86. Mansell, R., Petit, D. C. M. C., Fernández-Pacheco, A., Lavrijsen, R., Lee, J. H. & Cowburn, R. P. Magnetic properties and interlayer coupling of epitaxial Co/Cu films on Si. *J. Appl. Phys.* **116,** 063906. DOI: 10.1063/1.4893306 (2014).

87. Laracuente, A., Baker, L. & Whitman, L. Copper silicide nanocrystals on hydrogen - terminated Si(001). *Surface Science* **624,** 52–57. DOI: 10.1016/j.susc.2013.12.006 (2014).

88. Chakrabarti, D. & Laughlin, D. The Ca-Cu (Calcium-Copper) System. *B. Alloy Phase Diag.* **5,** 570. DOI: 10.1007/BF02868318 (1984).

89. Li, Q., Kartikowati, C. W., Horie, S., Ogi, T., Iwaki, T. & Okuyama, K. Correlation between particle size/domain structure and magnetic properties of highly crystalline Fe_3O_4 nanoparticles. *Sci. Rep.* **7,** 9894. DOI: 10.1038/s41598-017-09897-5 (2017).

90. Guo, L., Hua, G., Yang, B., Lu, H., Qiao, L., Yan, X. & Li, D. Electron work functions of ferrite and austenite phases in a duplex stainless steel and their adhesive forces with AFM silicon probe. *Sci Rep* **6,** 20660. DOI: 10.1038/srep20660 (2016).

91. Skriver, H. L. & Rosengaard, N. M. Surface energy and work function of elemental metals. *Physical Review B* **46,** 7157–7168. DOI: 10.1103/PhysRevB.46.7157 (1992).

92. Hugosson, H. W., Eriksson, O., Jansson, U., Ruban, A. V., Souvatis, P. & Abrikosov, I. A. Surface energies and work functions of the transition metal carbides. *Surface Science* **557,** 243–254. DOI: 10.1016/j.susc.2004.03.050 (2004).

93. Gildenblat, G. S., Grot, S. A. & Badzian, A. The electrical properties and device applications of homoepitaxial and polycrystalline diamond films. *Proceedings of the IEEE* **79,** 647–668. DOI: 10.1109/5.90130 (1991).

94. Baumann, P. K. & Nemanich, R. J. Electron emission from metal-diamond (100), (111) and (110) interfaces. *Diamond and Related Materials* **7,** 612–619. DOI: 10.1016/S0925-9635(97)00256-2 (1998).

95. Kohn, E. & Denisenko, A. Concepts for diamond electronics. *Thin Solid Films* **515,** 4333–4339. DOI: 10.1016/j.tsf.2006.07.179 (2007).

96. Pappas, D. P., Kämper, K. P., Miller, B. P., Hopster, H., Fowler, D. E., Luntz, A. C., Brundle, C. R. & Shen, Z. X. Magnetism of ultrathin films of Fe on Cu(100). *Journal of Applied Physics* **69,** 5209. DOI: 10.1063/1.348077 (1991).

97. Pappas, D. P., Glesener, J. W., Harris, V. G., Idzerda, Y. U., Krebs, J. J. & Prinz, G. A. Growth of Fcc Fe Films on Diamond. *Applied Physics Letters* **64,** 28–30. DOI: 10.1063/1.110910 (1994).

98. Hoff, H. A., Waytena, G. L., Glesener, J. W., Harris, V. G. & Pappas, D. P. Critical Thickness of Single-Crystal Fcc Iron on Diamond. *Surface Science* **326,** 252–266. DOI: 10.1016/0039-6028(94)00787-X (1995).

99. Swineford, R. S., Pappas, D. P. & Harris, V. G. Structure of C-stabilized fcc Fe on diamond: Epitaxial growth of austenite. *Phys Rev B Condens Matter* **52,** 7890–7893. DOI: 10.1103/PhysRevB.52.7890 (1995).

100. Sandweg, C. W., Kajiwara, Y., Chumak, A. V., Serga, A. A., Vasyuchka, V. I., Jungfleisch, M. B., Saitoh, E. & Hillebrands, B. Spin pumping by parametrically excited exchange magnons. *Phys Rev Lett* **106,** 216601. DOI: 10.1103/PhysRevLett.106.216601 (2011).

101. Li, D. Q., Keavney, D. J., Pearson, J., Bader, S. D., Pege, J. & Keune, W. Structural and magnetic phases of ultrathin Fe wedges and films grown on diamond (100). *Physical Review B* **57,** 10044–10048. DOI: 10.1103/PhysRevB.57.10044 (1998).

102. Ullmann, J., Heger, P., Pinkert, K. & Baba, K. Ions as a useful tool for carbon film deposition and modification. *Nuclear Instruments and Methods in Physics Research Section B-Beam Interactions with Materials and Atoms* **106,** 96–105. DOI: 10.1016/0168-583x(95)00685-0 (1995).

103. Dyachenko, O., Diek, N., Shapiro, Y., Tamang, R., Harneit, W., Reichling, M. & Borodin, A. A diamond (100) surface with perfect phase purity. *Chemical Physics Letters* **640,** 72–76. DOI: 10.1016/j.cplett.2015.10.015 (2015).

104. Ketteler, G., Weiss, W., Ranke, W. & Schlögl, R. Bulk and surface phases of iron oxides in an oxygen and water atmosphere at low pressure. *Physical Chemistry Chemical Physics* **3,** 1114–1122. DOI: 10.1039/b009288f (2001).

105. Mavroides, J. G., Kafalas, J. A. & Kolesar, D. F. Photoelectrolysis of water in cells with $SrTiO_3$ anodes. *Applied Physics Letters* **28,** 241–243. DOI: 10.1063/1.88723. eprint: https://doi.org/10.1063/1.88723 (1976).

106. Santander-Syro, A. F., Copie, O., Kondo, T., Fortuna, F., Pailhès, S., Weht, R., Qiu, X. G., Bertran, F., Nicolaou, A., Taleb-Ibrahimi, A., Le Fèvre, P., Herranz, G., Bibes, M., Reyren, N., Apertet, Y., Lecoeur, P., Barthélémy, A. & Rozenberg, M. J. Two-dimensional electron gas with universal subbands at the surface of $SrTiO_3$. *Nature* **469,** 189. DOI: 10.1038/nature09720 (2011).

107. Warusawithana, M. P., Cen, C., Sleasman, C. R., Woicik, J. C., Li, Y. L., Kourkoutis, L. F., Klug, J. A., Li, H., Ryan, P., Wang, L. P., Bedzyk, M., Muller, D. A., Chen,

L. Q., Levy, J. & Schlom, D. G. A Ferroelectric Oxide Made Directly on Silicon. *Science* **324,** 367–370. DOI: 10.1126/science.1169678 (2009).

108. Kawasaki, M., Takahashi, K., Maeda, T., Tsuchiya, R., Shinohara, M., Ishiyama, O., Yonezawa, T., Yoshimoto, M. & Koinuma, H. Atomic Control of the $SrTiO_3$ Crystal-Surface. *Science* **266,** 1540–1542. DOI: 10.1126/science.266.5190.1540 (1994).

109. Shimizu, R., Iwaya, K., Ohsawa, T., Shiraki, S., Hasegawa, T., Hashizume, T. & Hitosugi, T. Atomic-Scale Visualization of Initial Growth of Homoepitaxial $SrTiO_3$ Thin Film on an Atomically Ordered Substrate. *ACS Nano* **5,** 7967–7971. DOI: 10.1021/nn202477n (2011).

110. Herger, R., Willmott, P. R., Bunk, O., Schleputz, C. M., Patterson, B. D. & Delley, B. Surface of strontium titanate. *Phys Rev Lett* **98,** 076102. DOI: 10.1103/PhysRevLett.98.076102 (2007).

111. Campbell, C. T. Ultrathin metal films and particles on oxide surfaces: structural, electronic and chemisorptive properties. *Surface Science Reports* **27,** 1–111. DOI: 10.1016/S0167-5729(96)00011-8 (1997).

112. Chambers, S. A., Droubay, T. C., Capan, C. & Sun, G. Y. Unintentional F doping of $SrTiO_3$(100) etched in HF acid-structure and electronic properties. *Surface Science* **606,** 554–558. DOI: 10.1016/j.susc.2011.11.029 (2012).

113. Gerhold, S., Wang, Z., Schmid, M. & Diebold, U. Stoichiometry-driven switching between surface reconstructions on $SrTiO_3$(100). *Surface Science* **621,** L1–L4. DOI: 10.1016/j.susc.2013.10.015 (2014).

114. Vitos, L., Ruban, A. V., Skriver, H. L. & Kollar, J. The surface energy of metals. *Surface Science* **411,** 186–202. DOI: 10.1016/S0039-6028(98)00363-X (1998).

Appendix A

Lists of samples

A.1 Cu(100)

sample	experiment	AES data	analysis
1	8 nm Fe_xNi_{1-x}	multiple	Figure 1.3
2	8 nm Fe_xNi_{1-x}	multiple	Figures 1.3, 4.2
4	8 nm $Fe_{78}Ni_{22}$	aes150909p006	FIB transformation Chapter 4.3
4	8 nm $Fe_{78}Ni_{22}$	aes180205p004	FIB transformation Chapter 4.3
5	25 nm $Fe_{78}Ni_{22}$	aes151104p003	thickness of the metastable film Chapter 1
6	8 nm $Fe_{78}Ni_{22}$	aes161017p007	FIB transformation Chapter 4.3
6	8 nm $Fe_{78}Ni_{22}$	aes180327p001	FIB transformation Chapter 4.3
9	4 ML Fe	aes170529p002	effect of an Au capping layer on the FM properties
10	8 nm $Fe_{78}Ni_{22}$	aes170328p005	magnetic anisotropy tuned by FIB Chapter 4.3
11	8 nm $Fe_{78}Ni_{22}$	aes180315p002	magnetic anisotropy tuned by FIB Chapter 4.3
12	8 nm $Fe_{78}Ni_{22}$	aes180410p001	lithography, Au waveguides
13	8 nm $Fe_{78}Ni_{22}$	aes180410p001	AES measurement in Figure 4.1, lithography, Au waveguides
14-16	12 nm $Fe_{78}Ni_{22}$	aes180410p001	magnonic crystals, BLS measurement in Table 8.1
17	8 nm $Fe_{78}Ni_{22}$	aes190211p002	transformation with 4 keV Ar^+ ion beam, Figure 4.2

Table A.1 | Overview of Cu(100) samples used for the experiments in Chapter 4. Refer to Section 4.2 for further information on preparation.

A.2 $SrTiO_3(100)$

date	sample	experiment	substrate preparation	analysis
22-26.6.2015	1	40 nm Cu @ 300°C, post anneal	BHF + Shimizu	Figures 7.1 and 7.3
30.6.-2.7.2015	3	40 nm Cu @ 100°C	BHF + Shimizu	Figure 7.4
22-23.9.2015	6	4 nm @ 300°C, 36 nm @ 100°C	BHF + Shimizu	Figures 7.6 and 7.5
17-19.11.2015	9	8 nm $Fe_{78}Ni_{22}$	sputter/anneal	direct deposition, bcc $Fe_{78}Ni_{22}$ Chapter 7
29.1.-3.2.2016	12	preparation, calibration	sputter/anneal	Figure 7.2
3.2.-6.2.2016	13	40 nm Cu, PA @ 300°C + 100 nm Cu, PA @ 300°C	sputter/anneal	Figure 7.7
23.2.-25.2.2016	15	40 nm Cu, PA @ 300°C	sputter/anneal	no diffraction in LEED

Table A.2 | Overview of $SrTiO_3(100)$ samples used for the experiments in Chapter 7. PA corresponds to post anneal.

A.3 C(100)

sample	description of the experiment	substrate preparation	analysis* (# of experiment)
1	8 nm @ 400°C	aqua regia+piranha+ sputter+atomic H	exp#18 - sputtered+ atomic H
2	4 nm	anneal+atomic H	exp#5 - PA step by step PINUP
3	H-cleaning	sputtered+atomic H	exp#11 Figure 6.1
3	4+4 nm @ 450°C	sputtered+atomic H	exp#17 - two-step
4	4 nm	aqua regia+piranha+ anneal+atomic H	exp#8, exp#13 - PA step-by-step in RT-STM, Figure 6.2(a,c), Figure 6.3(a,b)
6	4 nm	anneal+ atomic H	exp#12 - RT, bcc, Figure 6.2(b)
6	8 nm at 400°C	anneal+ atomic H	exp#16 - Figure 6.3(c-d)
7	4 nm	anneal+ atomic H	exp#15 - PA step by step PINUP
9	8 nm at 450°C	anneal+atomic H	exp#20 - one-step deposition

Table A.3 | Overview of C(100) samples used for the experiments in Chapter 5. *All crystals except for C#3 in experiment #11 and C#6 in experiment #12 were used in Figure 6.4. PA corresponds to post anneal.

A.4 Si(100)

sample	treatment	AES files	notes and analysis (exp.)
Si HF1	HF-etching	20151015	deposition of the Cu buffer layer, Figures 5.4 and 5.7
Si HF2	HF-etching	aes161004p001	clean H-Si, Figure 5.2
Si HF3	HF-etching	20160303	clean H-Si, Figure 5.1
Si 1-7	flashing + H-termination	multiple files	calibration of substrate preparation
Si 8	125 nm Cu	aes170620p006	calibration of Cu deposition
Si 8	+8 nm FeNi	aes170620p008	calibration of $Fe_{78}Ni_{22}$deposition
Si 10	65 nm Cu	aes170719p002	thinner Cu film…
Si 10	+ 8nm FeNi	aes170719p003	…leads to a ferromagnetic signal
Si 12	flashing + H-termination	aes180115p001	AES measurement in Figure 5.2
Si 13	125nm Cu (Ca contam.)	180117p002	CuCa(100) buffer layer, Figure 5.4
Si 13	+ 8nm FeNi	aes180118p003	metastable film
Si 16	130nm Cu (Ca contam.)	aes180125p002	CuCa(100) buffer layer
Si 16	+ 8nm FeNi	aes180125p003	metastable film

Table A.4 | Overview of Si(100) samples used for the experiments in Chapter 5. Three relevant experiments on the HF-etched Si are included.

sample	treatment	AES files	notes and analysis (exp.)
Si 17	flashing + H-termination	20180129	multiple files, Figure 5.1
Si 17	40nm Cu (Ca contam.)	aes180129p003	CuCa(100) buffer layer
Si 17	40nm CuCa + 90nm Cu	aes180130p003	clean Cu(100) buffer layer
Si 17	+ 8nm FeNi	aes180131p002	metastable film, Figure 5.5; ion-beam transformation, Figure 5.9
Si 20	125nm Cu	aes180210p002	clean Cu(100) buffer layer
Si 20	+ 8nm FeNi	20180210	metastable film, Figure 5.7; FIB transformation, Figure 5.10
Si 21	40nm CuCa+90 nm Cu	aes180216p003	clean Cu(100) buffer layer
Si 21	+ 24nm FeNi	aes180217p003	metastable film
Si 22	100 nm CuCa	aes180301p001	Ca-contaminated film, Figure 5.5
Si 22	100 nm CuCa + 30 nm Cu	aes180302p003 multiple files	Post-anneal of 130 nm Cu, Figures 5.5 and 5.6
Si 23	outgassed	aes180405p001	AES measurement in Figure 5.2
Si 24-27	CuCa	multiple files	calibration of Ca content
Si 28	110 nm Cu+Ca	aes180706p002	CuCa(100) buffer layer
Si 28	110 nm Cu+Ca + 20 nm Cu	aes180706p004	clean Cu(100) buffer layer
Si 28	+ 10nm FeNi	aes180706p005	metastable film
Si 29	120nm CuCa + 10 nm Cu	aes180725p002	clean Cu(100) buffer layer
Si 29	+ 16nm FeNi	aes180725p003	metastable film

Table A.5 | Overview of Si(100) samples used for the experiments in Chapter 5 (continued).

Appendix B

The hydrogen cracker

The H-cracker served for both, H-termination of Si(100) after flashing and removing the graphite overlayer from C(100) (chapters 5 and 6). The hydrogen cracker was built according to the design of Bischler et al., where H_2 dissociates in a hot tungsten capillary [62]. Molecular H_2 is introduced by a variable leak valve into a tungsten capillary (0.6 mm inner diameter), which was heated by electron bombardment from a tungsten filament to approx. 1800 K. The diameter of the filament was approx. 6 mm. The usual working parameters were 2.6 A filament current, producing a 35 mA emission current at 1000 V on the H-capillary, H_2 pressure of 10^{-6} mbar.

B.1 Technical description

To decrease the evaporation of tungsten oxide into the chamber during outgassing and the radiative heating during atomic H deposition, the whole setup around the hot filament was encased in a liquid-nitrogen-cooled copper shielding for a good thermal conductivity. The H-cracker has been designed to fit onto a ConFlat (CF)43 flange, which has been attached to a CF63 port (CFA63/38D from Hositrad). The W capillary is seated in a molybdenum connector which tightly fits the capillary on the one side and a ceramic on the other. The ceramic is then attached to an adaptor made of stainless steel, which is spot-welded to the cooling base and therefore keeps

the whole capillary setup in place. The connection from the adapter to the H_2 line is facilitated by bellows. The high voltage (HV) is brought to the W capillary via the molybdenum connector, which is connected to a HV feedthrough via a thin tungsten wire. The HV connection carries only the emission current and therefore a thin wire suffices for the connection. The HV feedthrough is spot-welded to the cooling base and it is connected to the ambient by another CF16 HV feedthrough. The wire connecting the two feedthroughs is covered by ceramic beads and ceramic tubes. The filament is suspended on two tantalum wires, which are connected to power feedthroughs. The power feedthroughs are also spot-welded to the cooling base and connected by ceramic-insulated copper wires to a combined power-thermocouple feedthrough. The thermocouple is connected to the outside of the copper cooling shield and is isolated by a Kapton wire. The H-cracker can be closed by a shutter, which is operated by a rotational feedthrough. The momentum is translated by a cardan joint which provides approx. 90° rotation.

There are five CF16 feedthroughs on a cluster flange (CF35/5CF16 from Hositrad):

1. High voltage BNC low frequency, grounded, for supply of 1 kV to the W- capillary - 7593-02-CF, Hositrad

2. Power supply combined with a thermocouple (K-type) - 263-TCK-1-CU15-2-C16, Allectra

3. Liquid nitrogen (LN_2) feedthrough for cooling of the copper shield around the capillary and the filament. There is a Swagelok tee at the end of the feedthrough, which can be connected to a dewar supplying LN_2 and an exhaust. There is a stainless steel capillary inserted in the LN_2 line, which supplies the LN_2 and after heating at the end of the capillary, it escapes through the space between the LN_2 capillary and the wall of the LN_2 feedthrough. The feedthrough is custom-made at Hositrad and welded at the end at the IAP / TU WIEN.

4. Extension to another CF16 flange for a H_2 supply through a leak valve (custom made at the IAP workshop). Currently, it is connected to an Agilent variable

leak valve (9515106, Agilent). The leak valve is supported by a stainless steel stand to avoid bending of the weld.

5. Rotational feedthrough operating the cardan joint. The cardan joint consists of alternating stainless steel and copper parts which allow it to rotate in UHV. The rotational feedthrough is similar to 611-RD-C16, Allectra.

B.2 Technical drawings

The remaining items were built at the TU Wien according to the drawings, which follow. The overview 3D model includes a recent (winter 2018) addition of a thermocouple (chromel-alumel), which is attached by a screw to the bottom part of the cooling shroud.

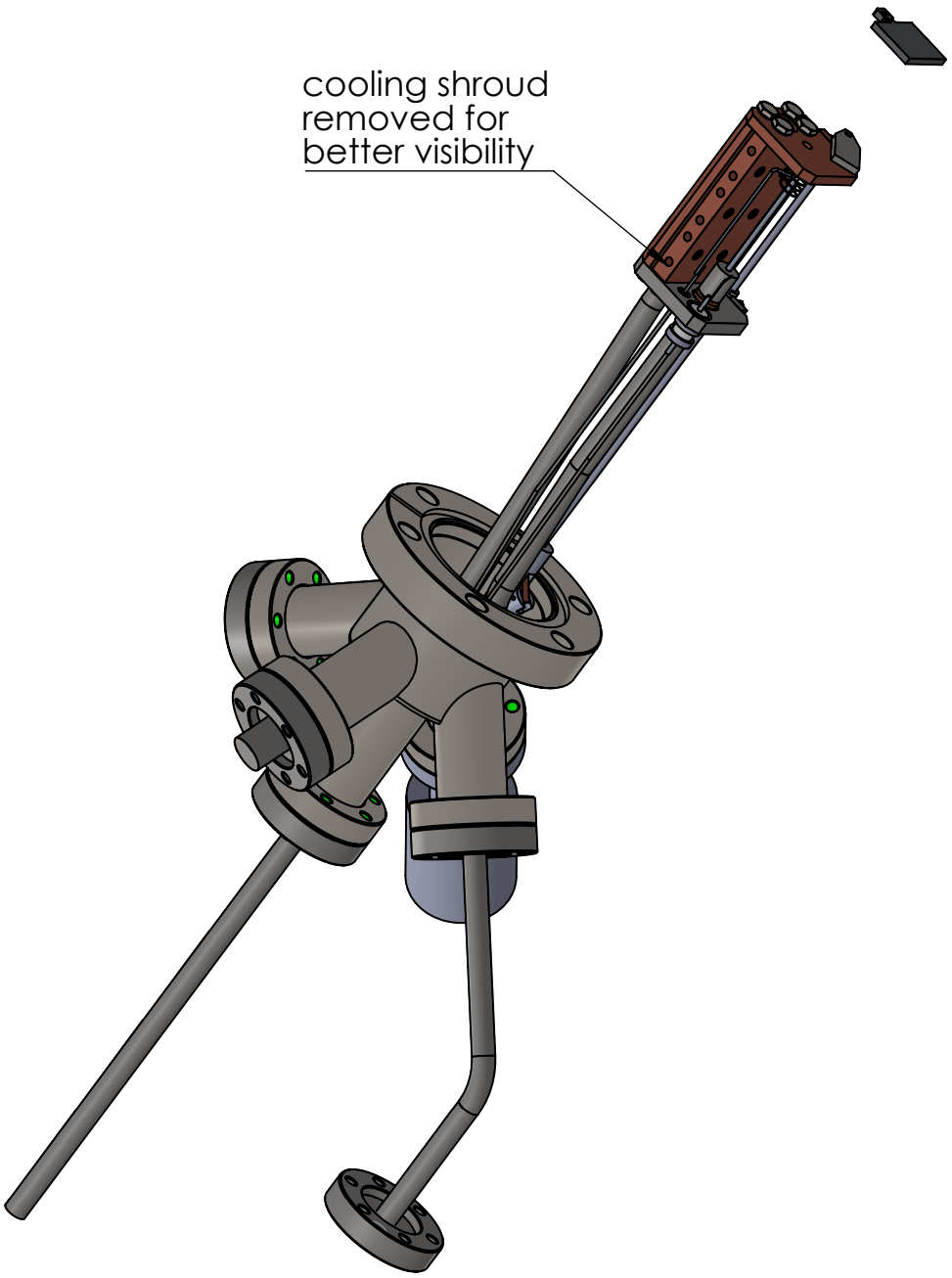

UNLESS OTHERWISE SPECIFIED: DIMENSIONS ARE IN MILLIMETERS DEBURR AND BREAK SHARP EDGES	A4	TITLE:	3D overview
DRAWN Jonas Gloss CHK'D Michael Schmid APPV'D Peter Varga MFG Workshop IAP TU Wien	Material Cu, Mo, W, Ta, SS, Chr/Alu WEIGHT:	DWG NO. H-cracker SCALE:1:5	SHEET 1 OF 13

SOLIDWORKS Educational Product. For Instructional Use Only.

POS-NR.	DESCRIPTION
1	Hositrad_CF35-5CF16
2	LN2 cooling^H-cracker complete assembly
3	Filament feedthrough
4	HV feedthrough
5	H inlet full
6	sample plate
7	shutter v2
8	cooling body
9	capillary assembly^H-cracker complete assembly
10	filament assembly^H-cracker complete assembly
11	cooling base^H-cracker complete assembly

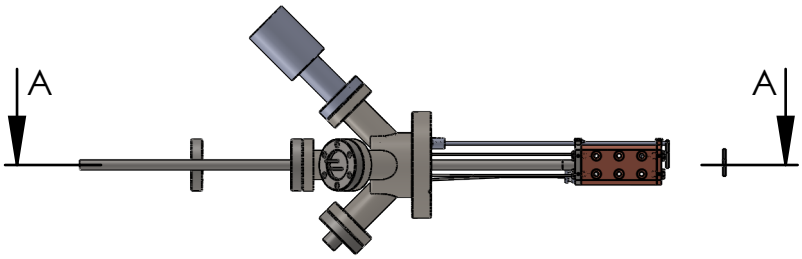

SECTIONA-A

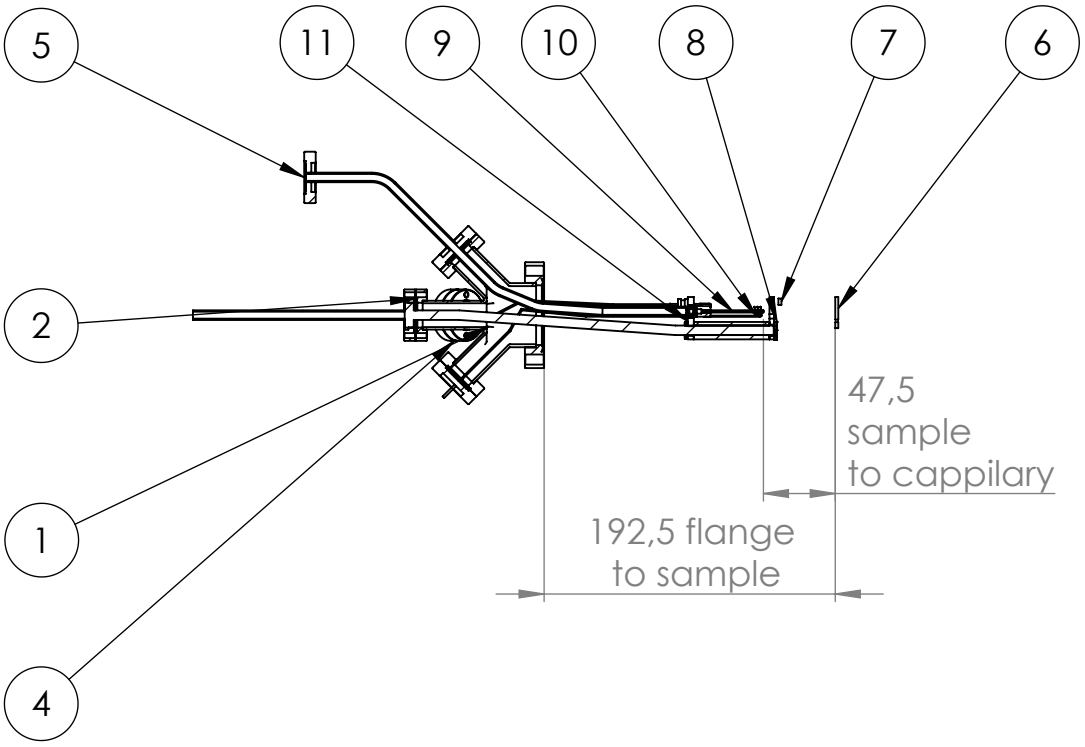

UNLESS OTHERWISE SPECIFIED: DIMENSIONS ARE IN MILLIMETERS DEBURR AND BREAK SHARP EDGES	A4	TITLE:	3D overview
DRAWN Jonas Gloss CHK'D Michael Schmid APPV'D Peter Varga MFG Workshop IAP TU Wien	Material: Cu, Mo, W, Ta, SS, Chr/Alu WEIGHT:	DWG NO.	H-cracker
		SCALE:1:5	SHEET 2 OF 13

SOLIDWORKS Educational Product. For Instructional Use Only.

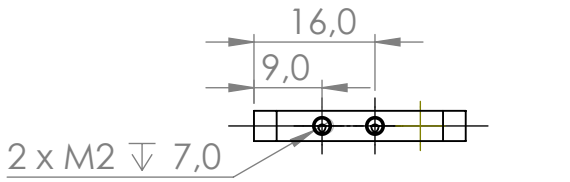

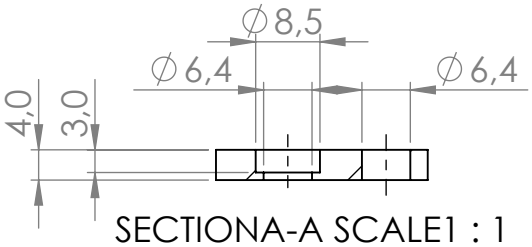

SECTIONA-A SCALE1 : 1

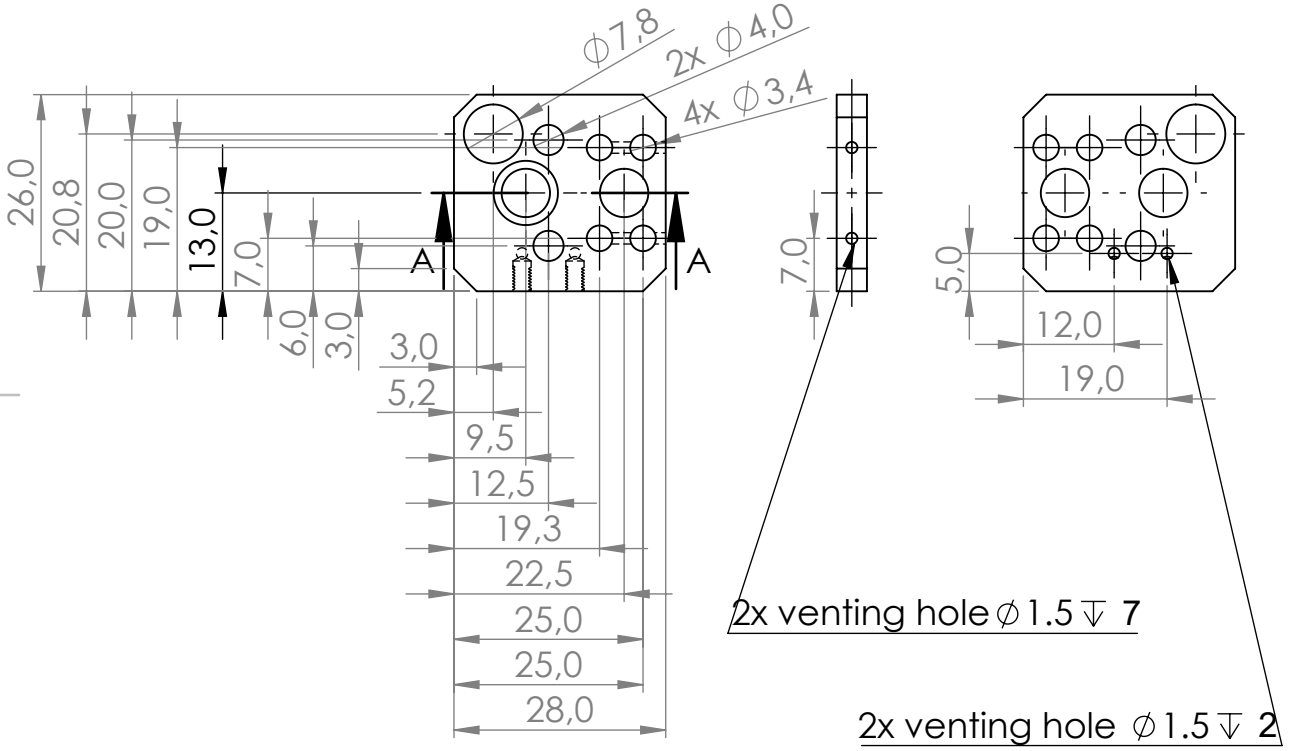

UNLESS OTHERWISE SPECIFIED: DIMENSIONS ARE IN MILLIMETERS DEBURR AND BREAK SHARP EDGES	A4	TITLE:	cooling base
DRAWN Jonas Gloss CHK'D Michael Schmid APPV'D Peter Varga MFG Workshop IAP TU Wien	Material: stainless steel WEIGHT:	DWG NO.	H-cracker SCALE:1:5 SHEET 3 OF 13

SOLIDWORKS Educational Product. For Instructional Use Only.

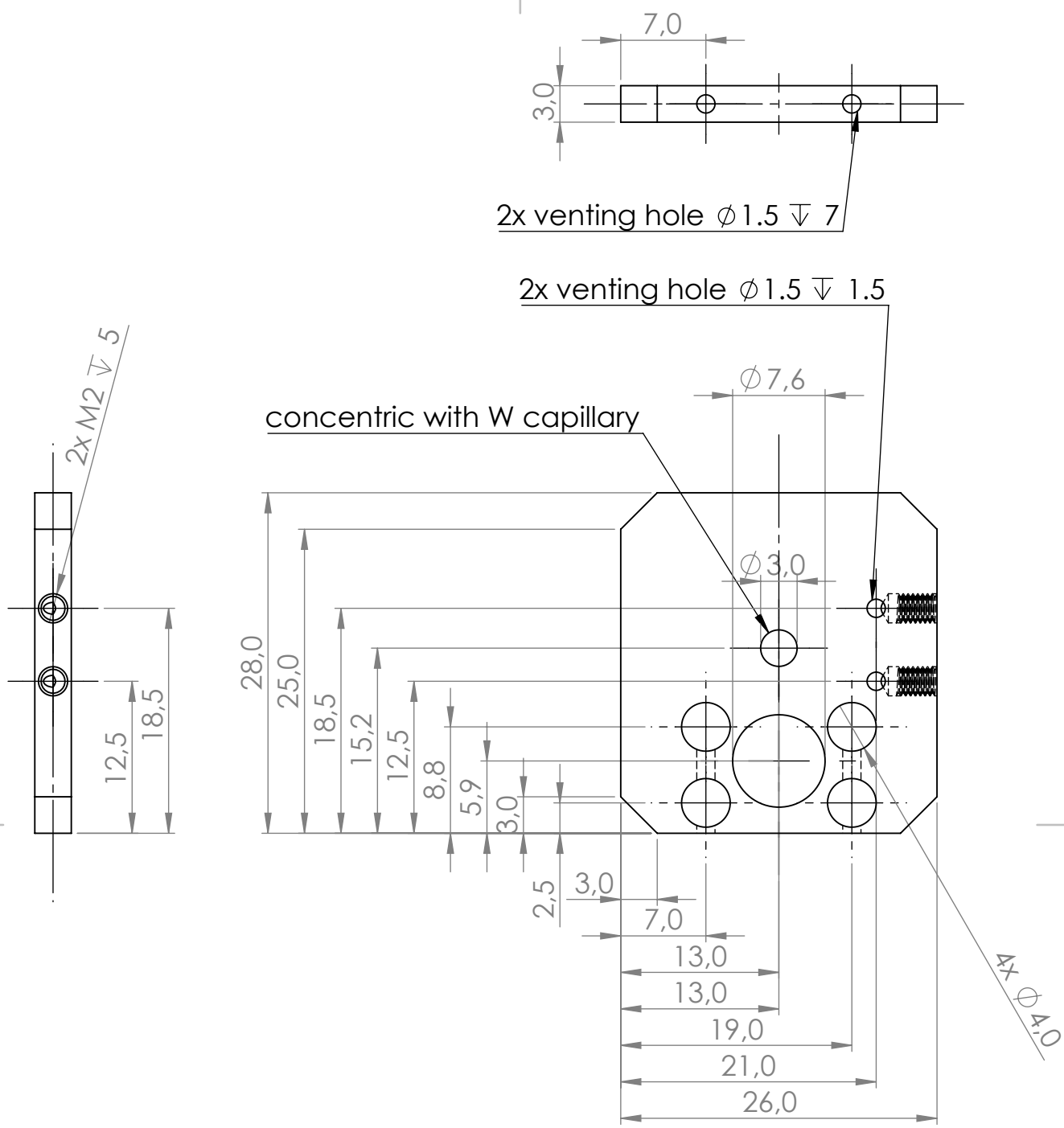

UNLESS OTHERWISE SPECIFIED: DIMENSIONS ARE IN MILLIMETERS DEBURR AND BREAK SHARP EDGES	A4		TITLE: cooling top
DRAWN Jonas Gloss CHK'D Michael Schmid APPV'D Peter Varga MFG Workshop IAP TU Wien	Material: Cu WEIGHT:		DWG NO. H-cracker SCALE:2:1 SHEET 4 OF 13

SOLIDWORKS Educational Product. For Instructional Use Only.

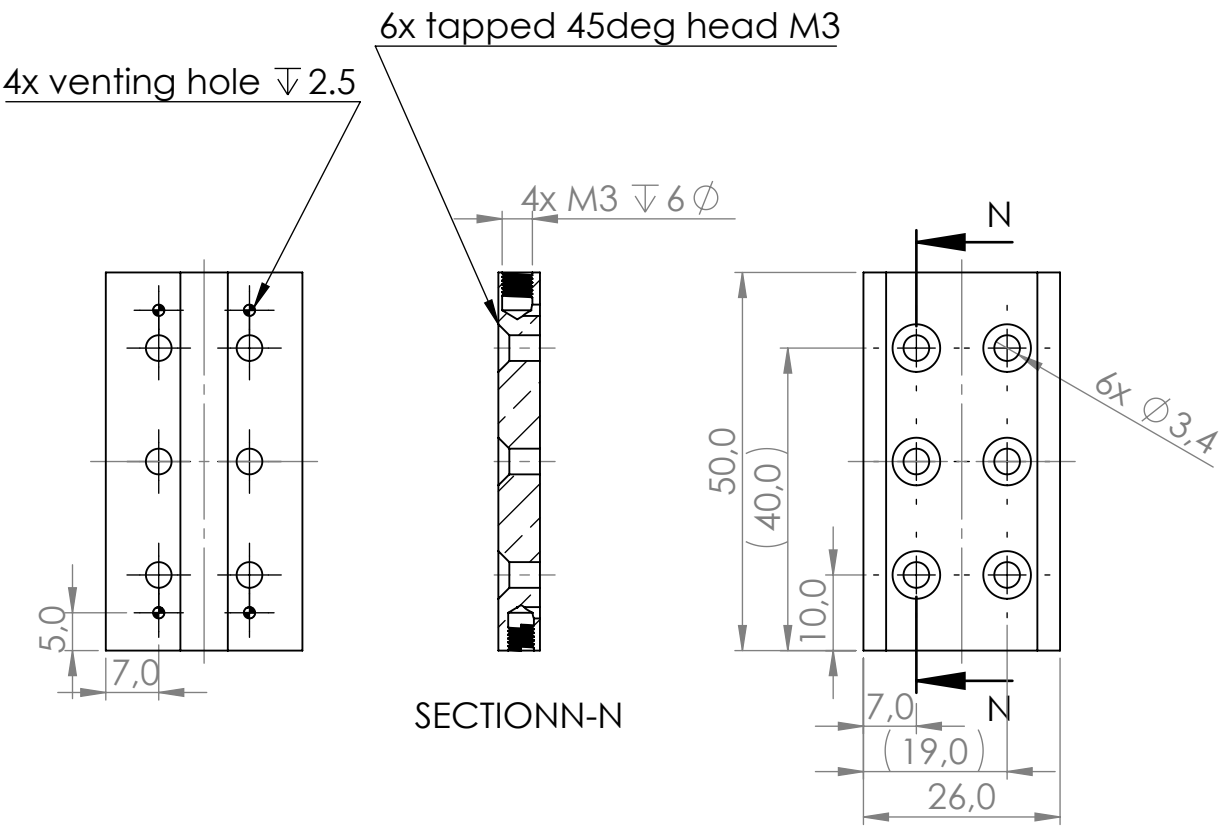

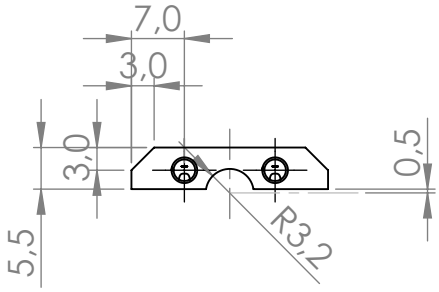

UNLESS OTHERWISE SPECIFIED: DIMENSIONS ARE IN MILLIMETERS DEBURR AND BREAK SHARP EDGES	A4	TITLE:	cooling body outside
DRAWN Jonas Gloss CHK'D Michael Schmid APPV'D Peter Varga MFG Workshop IAP TU Wien	Material: Cu WEIGHT:	DWG NO.	H-cracker SCALE:1:1 SHEET 5 OF 13

SOLIDWORKS Educational Product. For Instructional Use Only.

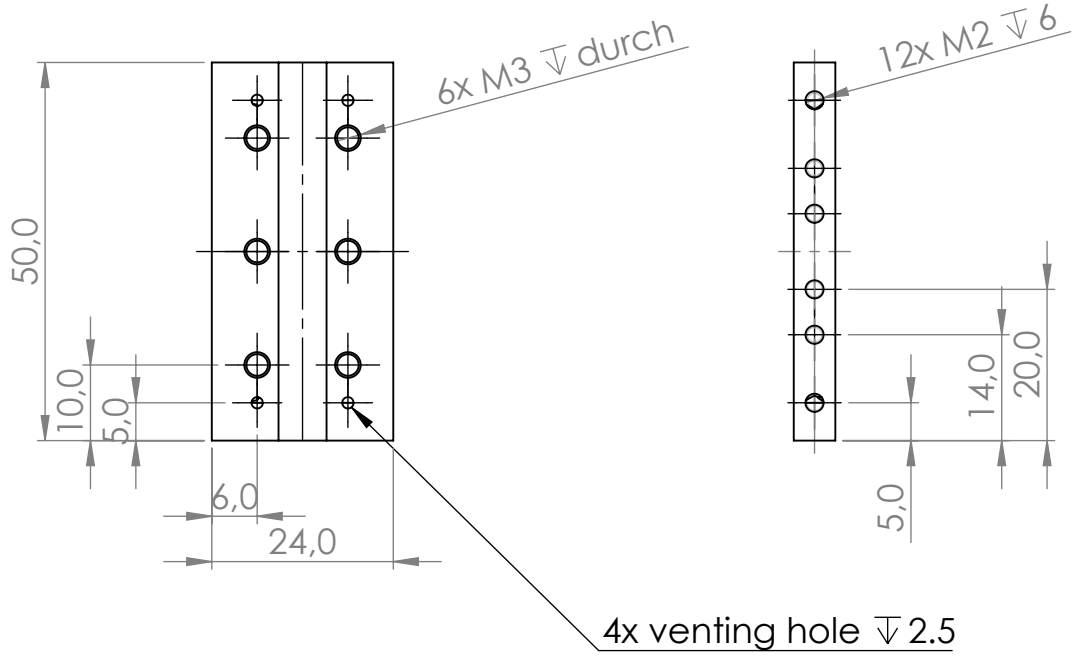

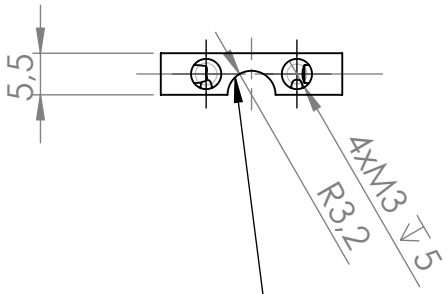

UNLESS OTHERWISE SPECIFIED: DIMENSIONS ARE IN MILLIMETERS DEBURR AND BREAK SHARP EDGES	A4	TITLE:	cooling body inside
DRAWN Jonas Gloss CHK'D Michael Schmid APPV'D Peter Varga MFG Workshop IAP TU Wien	Material: Cu WEIGHT:	DWG NO.	H-cracker SCALE:2:1 SHEET 6 OF 13

SOLIDWORKS Educational Product. For Instructional Use Only.

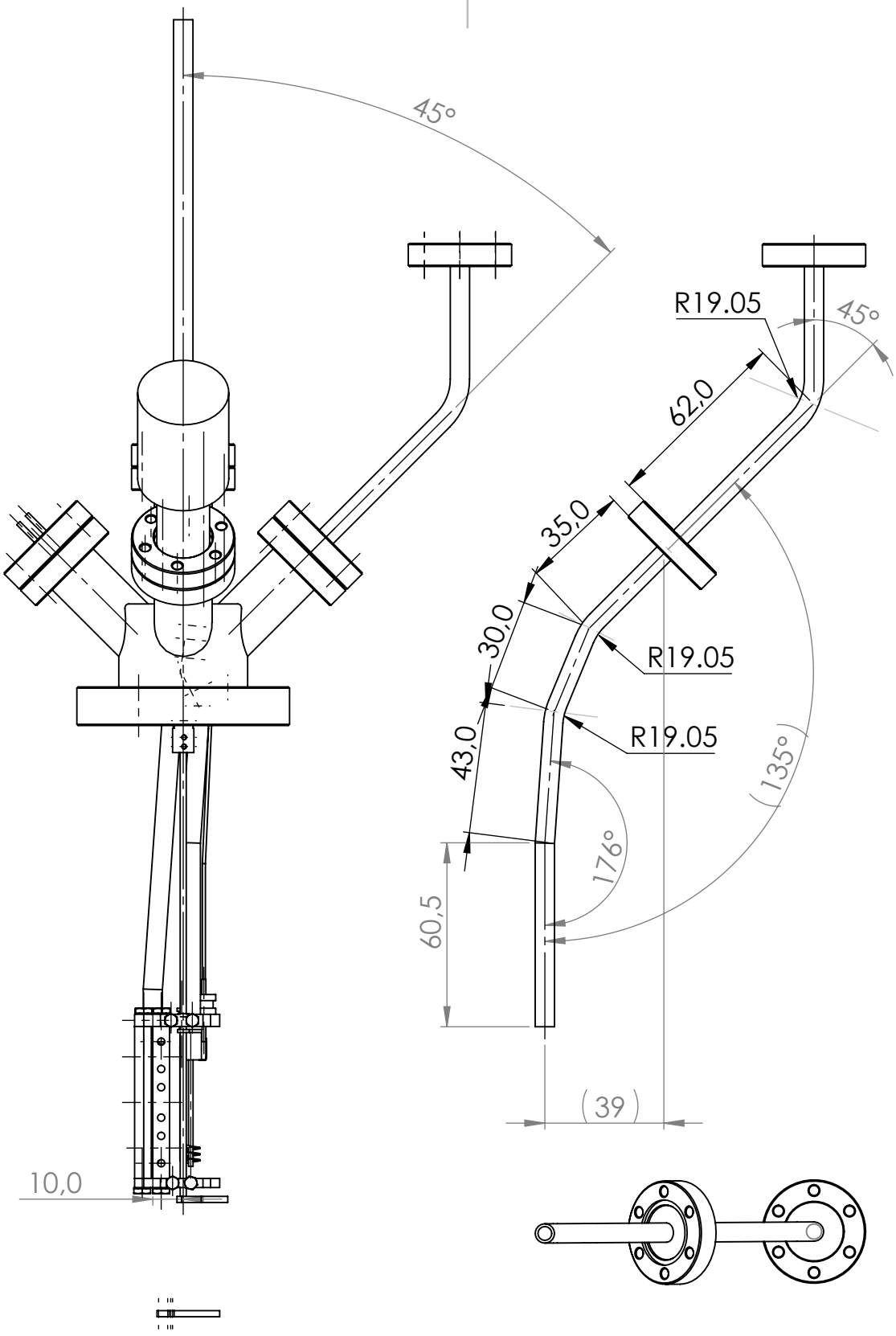

UNLESS OTHERWISE SPECIFIED: DIMENSIONS ARE IN MILLIMETERS DEBURR AND BREAK SHARP EDGES	A4		TITLE: 3D overview
DRAWN Jonas Gloss		Material	DWG NO. H-cracker
CHK'D Michael Schmid		XXXXXXX	
APPV'D Peter Varga			
MFG Workshop IAP TU Wien		WEIGHT:	SCALE:1:5 SHEET 7 OF 13

SOLIDWORKS Educational Product. For Instructional Use Only.

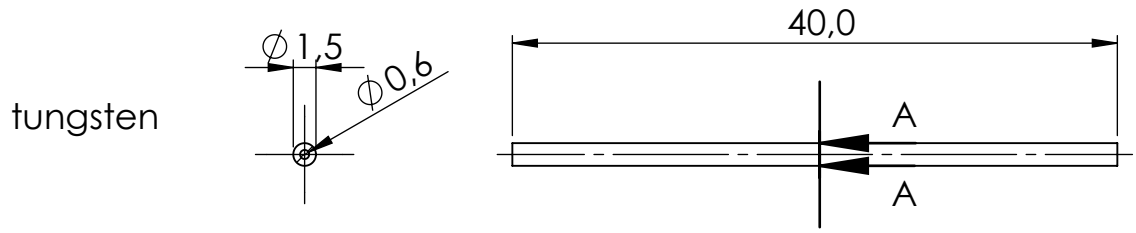

SECTION A-A
SCALE 2 : 1

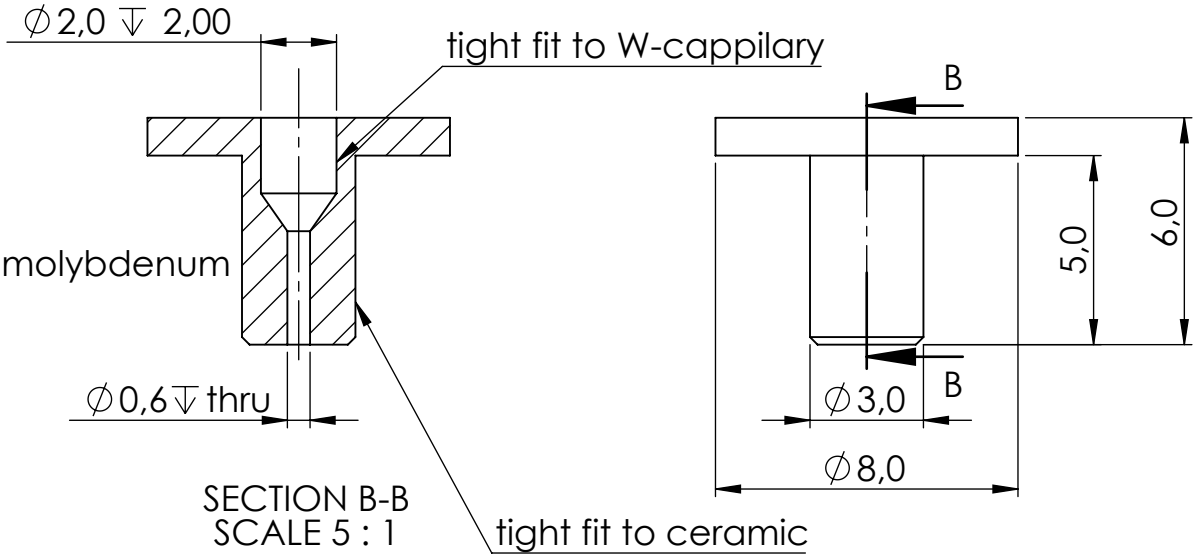

SECTION B-B
SCALE 5 : 1

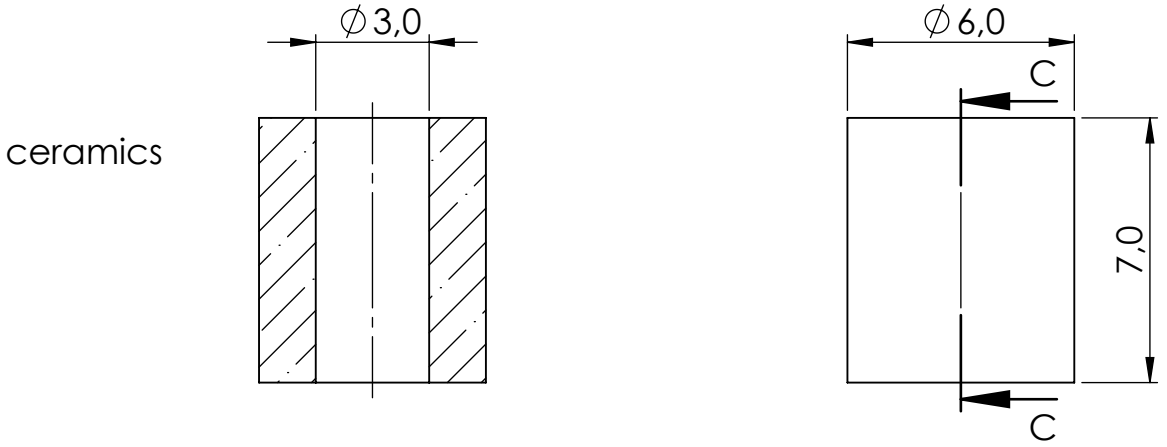

SECTION C-C
SCALE 5 : 1

UNLESS OTHERWISE SPECIFIED: DIMENSIONS ARE IN MILLIMETERS DEBURR AND BREAK SHARP EDGES	A4	TITLE:	H2 line to capillary
DRAWN Jonas Gloss CHK'D Michael Schmid APPV'D Peter Varga MFG Workshop IAP TU Wien	Material: stainless steel WEIGHT:	DWG NO.: H-cracker SCALE:10:1	SHEET 8 OF 13

SOLIDWORKS Educational Product. For Instructional Use Only.

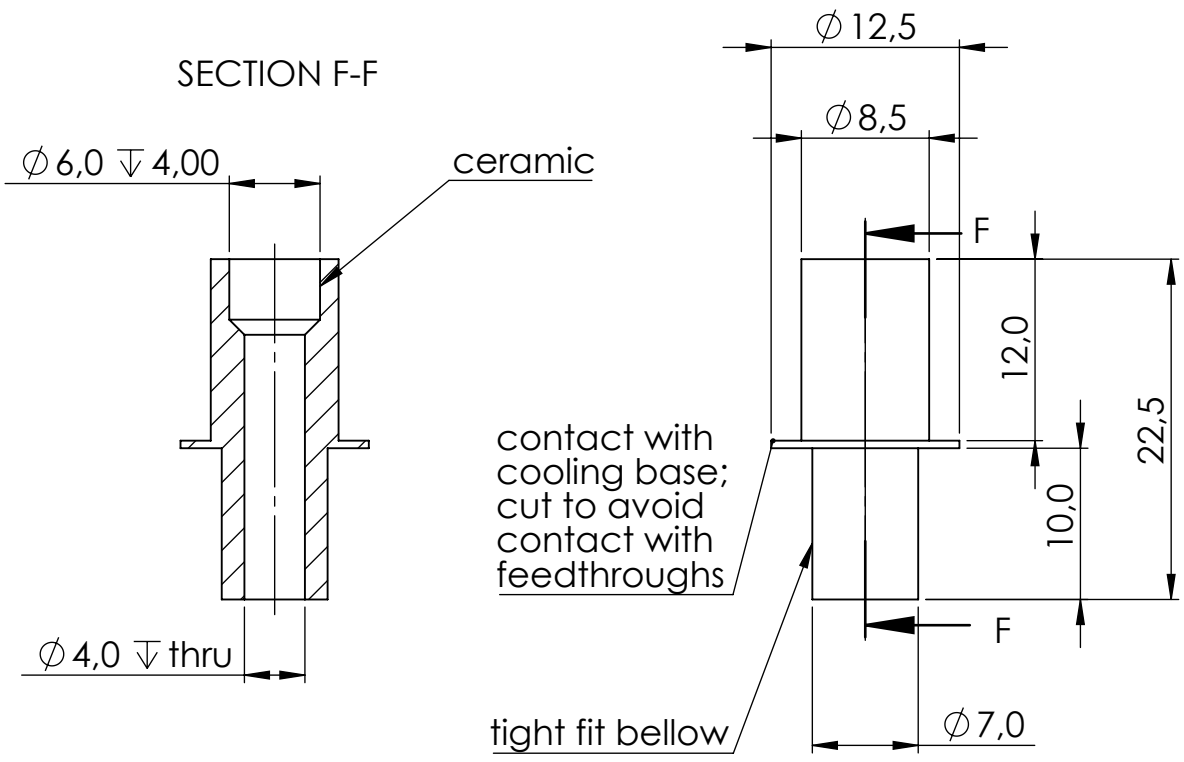

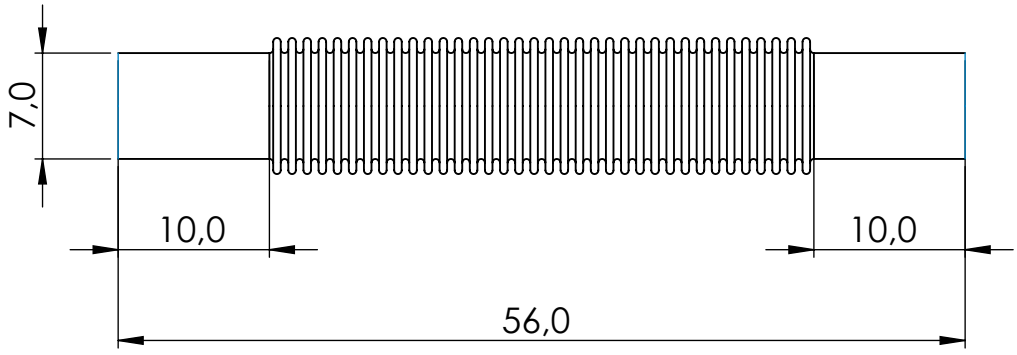

UNLESS OTHERWISE SPECIFIED: DIMENSIONS ARE IN MILLIMETERS DEBURR AND BREAK SHARP EDGES	A4		TITLE:	H2 line to capillary
DRAWN Jonas Gloss		Material	DWG NO.	H-cracker
CHK'D Michael Schmid		stainless steel		
APPV'D Peter Varga				
MFG Workshop IAP TU Wien		WEIGHT:	SCALE:2:1	SHEET 9 OF 13

SOLIDWORKS Educational Product. For Instructional Use Only.

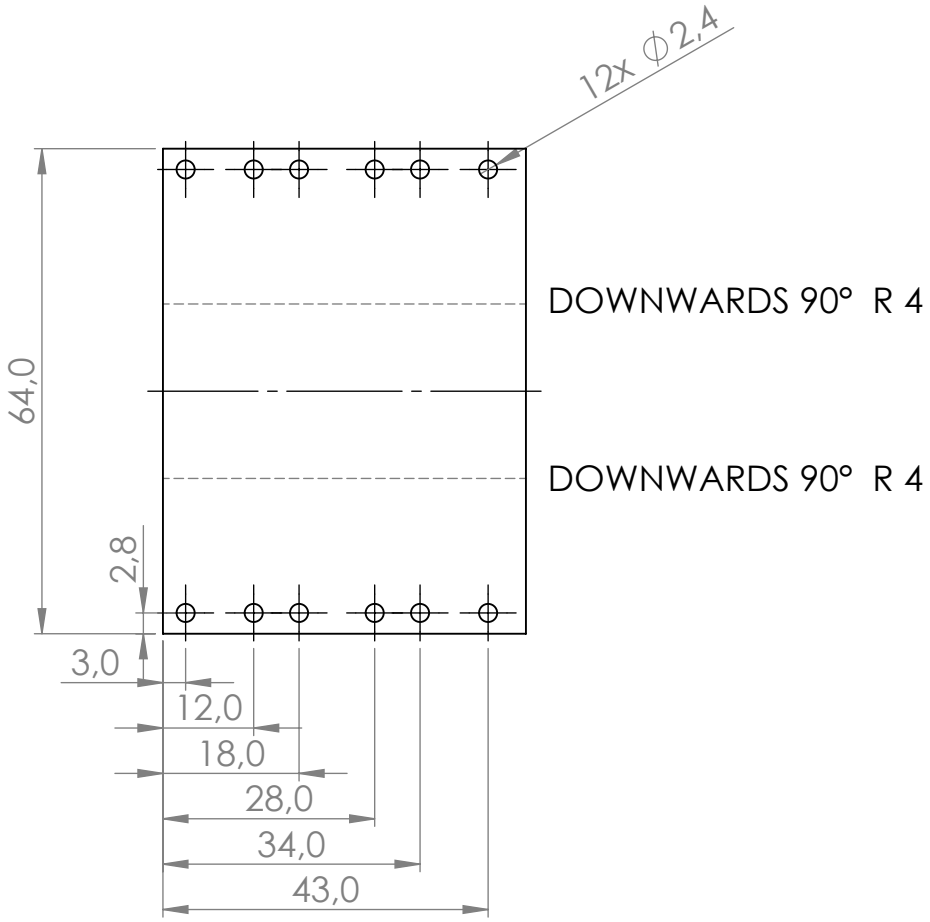

UNLESS OTHERWISE SPECIFIED: DIMENSIONS ARE IN MILLIMETERS DEBURR AND BREAK SHARP EDGES	A4	TITLE:	cooling shroud
DRAWN Jonas Gloss CHK'D Michael Schmid APPV'D Peter Varga MFG Workshop IAP TU Wien	Material Cu sheet metal 1 mm WEIGHT:	DWG NO. H-cracker SCALE:1:1	SHEET 10 OF 13

SOLIDWORKS Educational Product. For Instructional Use Only.

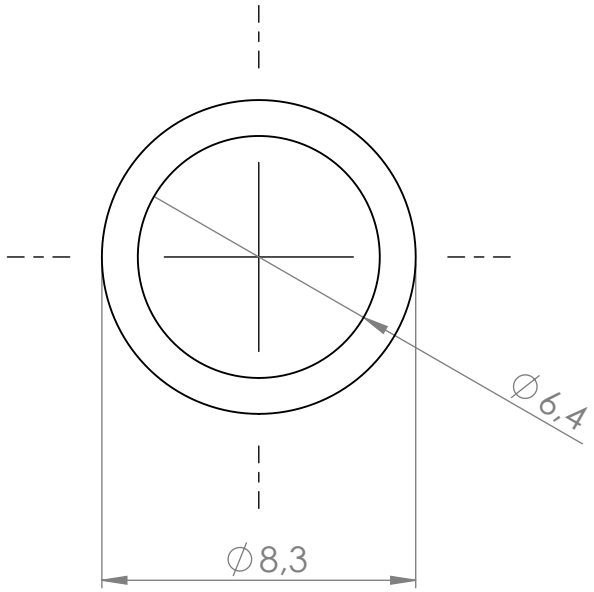

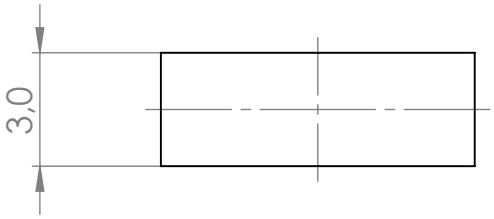

UNLESS OTHERWISE SPECIFIED: DIMENSIONS ARE IN MILLIMETERS DEBURR AND BREAK SHARP EDGES	A4		TITLE:	cooling ring
DRAWN Jonas Gloss		Material	DWG NO.	H-cracker
CHK'D Michael Schmid		Cu		
APPV'D Peter Varga				
MFG Workshop IAP TU Wien		WEIGHT:	SCALE:5:1	SHEET 11 OF 13

SOLIDWORKS Educational Product. For Instructional Use Only.

Tungsten filament

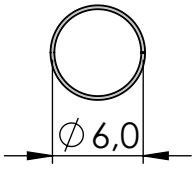

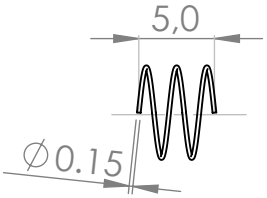

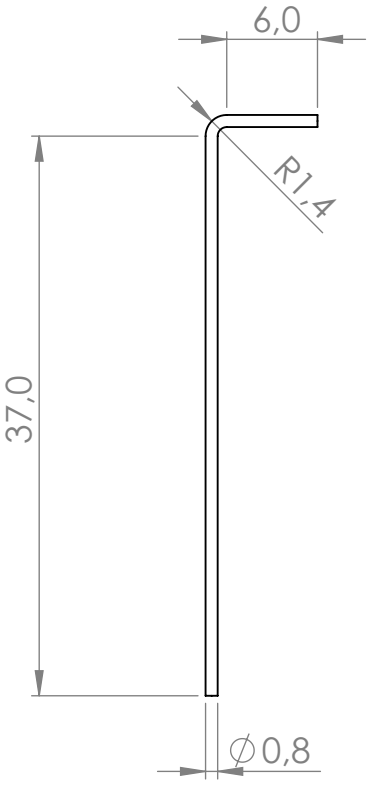

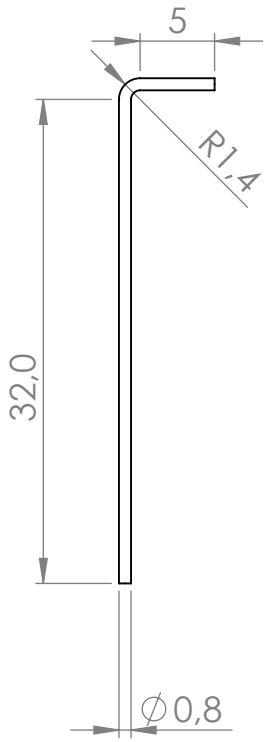

Tantalum

UNLESS OTHERWISE SPECIFIED: DIMENSIONS ARE IN MILLIMETERS DEBURR AND BREAK SHARP EDGES	A4	TITLE:	filament+holders
DRAWN Jonas Gloss CHK'D Michael Schmid APPV'D Peter Varga MFG Workshop IAP TU Wien	Material Ta, W WEIGHT:	DWG NO.	H-cracker SCALE:10:1 SHEET 12 OF 13

SOLIDWORKS Educational Product. For Instructional Use Only.

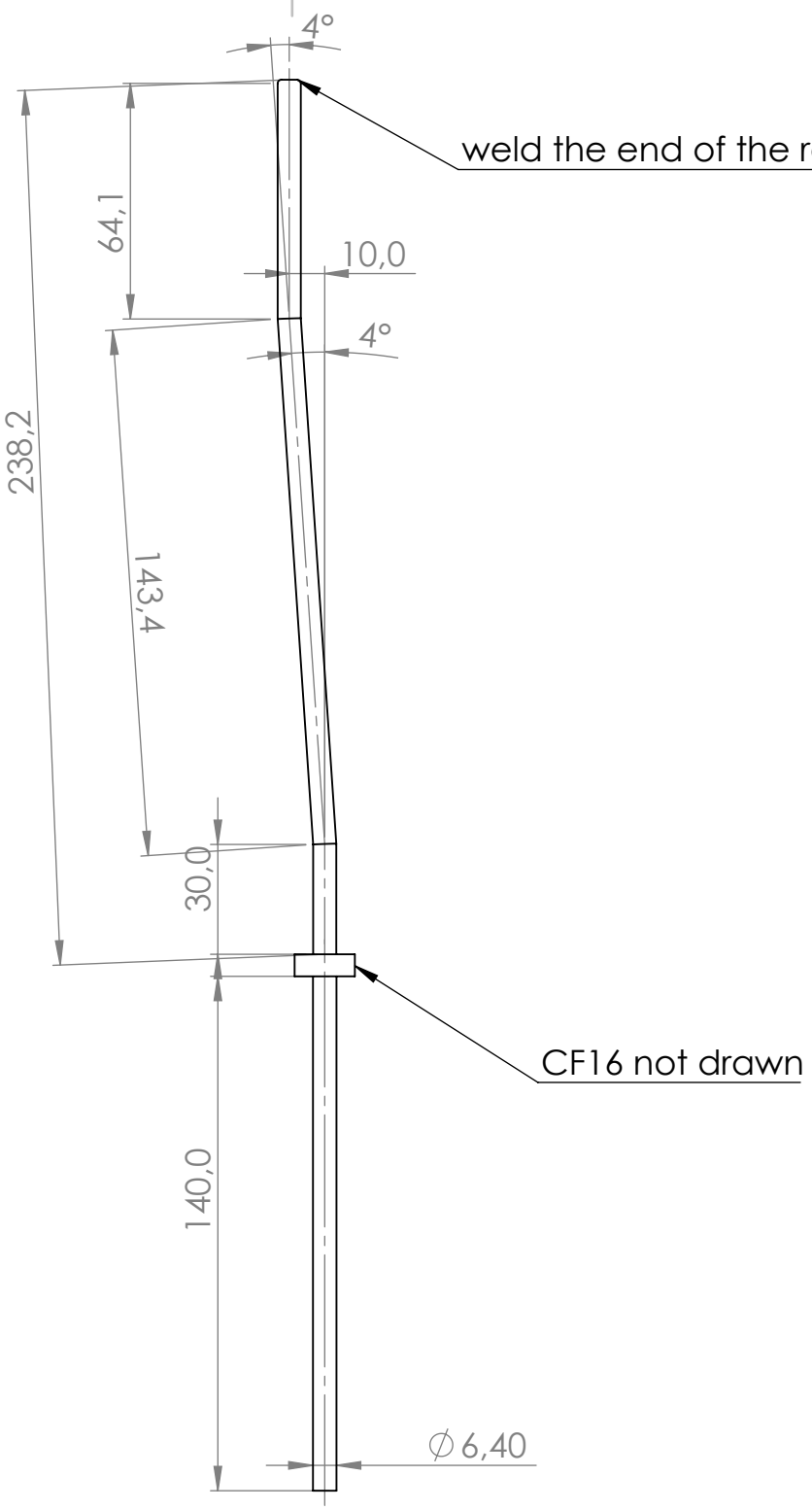

this part was ordered from
Hositrad and bent
at the IAP workshop.
It is recommended
to have it bent at the producer.

UNLESS OTHERWISE SPECIFIED: DIMENSIONS ARE IN MILLIMETERS DEBURR AND BREAK SHARP EDGES	A4		TITLE: simplified LN2 feedth.
DRAWN Jonas Gloss CHK'D Michael Schmid APPV'D Peter Varga MFG Workshop IAP TU Wien	Material: stainless steel WEIGHT:		DWG NO. H-cracker SCALE:1:5 SHEET 13 OF 13

SOLIDWORKS Educational Product. For Instructional Use Only.

spot-welded stainless steel parts
to keep the length of the shutter const.

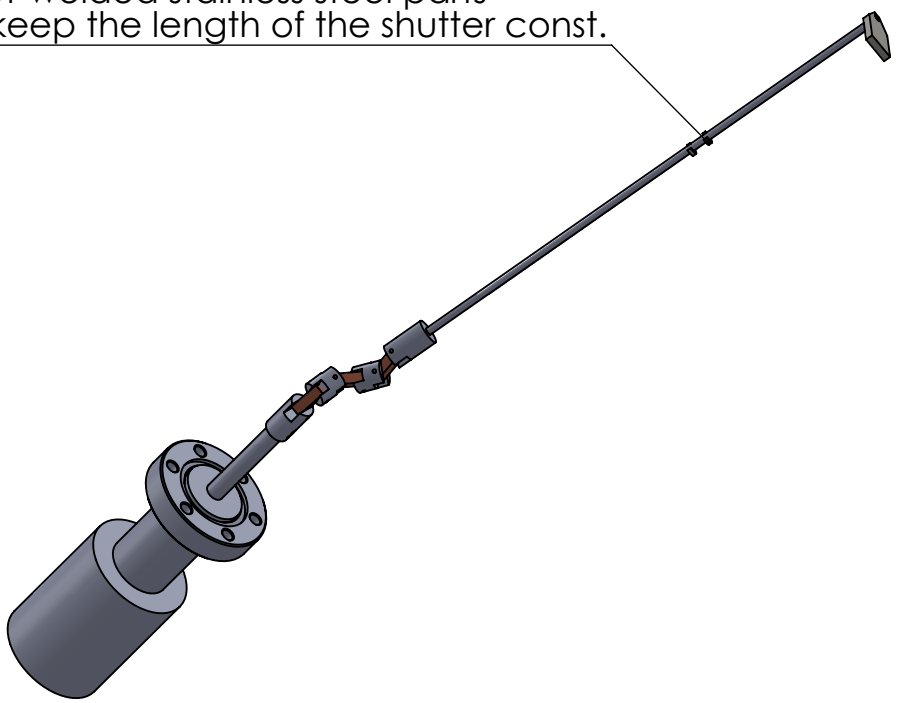

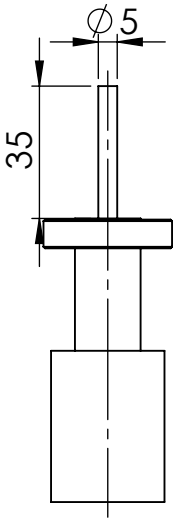

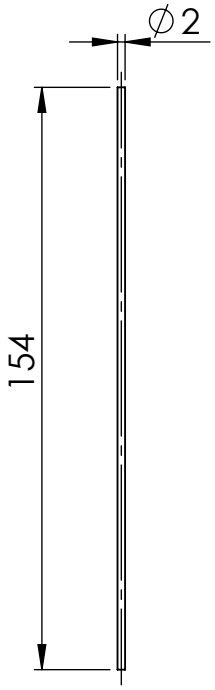

UNLESS OTHERWISE SPECIFIED: DIMENSIONS ARE IN MILLIMETERS DEBURR AND BREAK SHARP EDGES	A4		TITLE:	shutter - assembly
DRAWN Jonas Gloss CHK'D Michael Schmid APPV'D Peter Varga MFG Workshop IAP TU Wien		Material stainless steel Cu WEIGHT:	DWG NO.	H-cracker
			SCALE:1:2	SHEET 1 OF 5

SOLIDWORKS Educational Product. For Instructional Use Only.

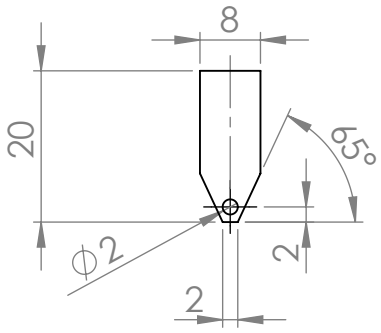

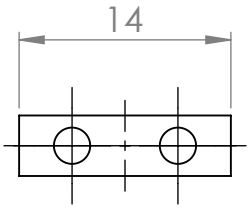

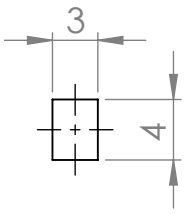

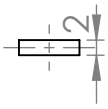

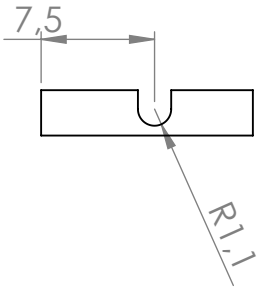

Copper

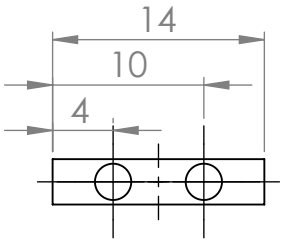

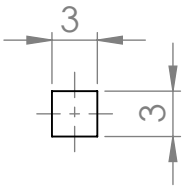

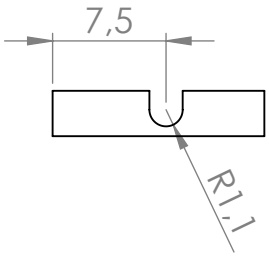

UNLESS OTHERWISE SPECIFIED: DIMENSIONS ARE IN MILLIMETERS DEBURR AND BREAK SHARP EDGES	A4		TITLE:	shutter parts A
DRAWN Jonas Gloss		Material	DWG NO.	H-cracker
CHK'D Michael Schmid		stainless steel Cu		
APPV'D Peter Varga				
MFG Workshop IAP TU Wien		WEIGHT:	SCALE:1:2	SHEET 2 OF 5

SOLIDWORKS Educational Product. For Instructional Use Only.

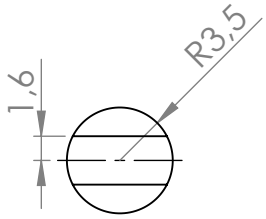

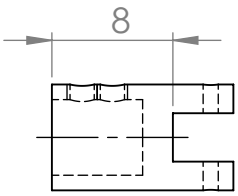

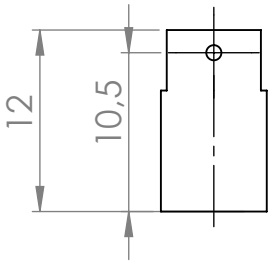

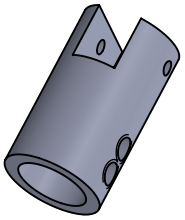

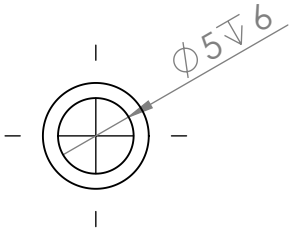

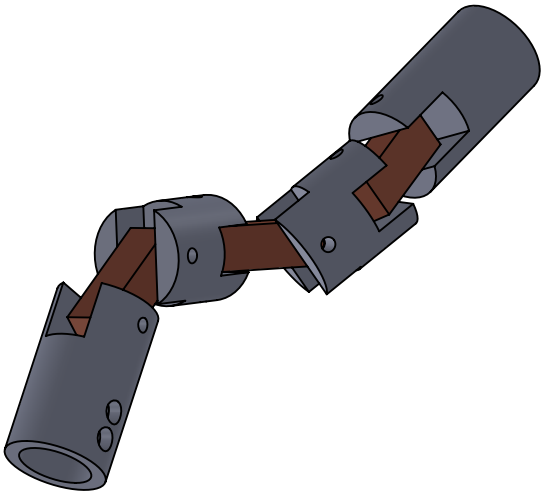

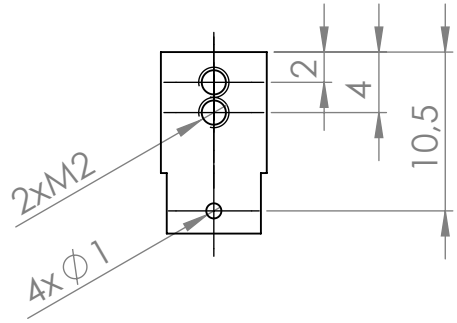

UNLESS OTHERWISE SPECIFIED: DIMENSIONS ARE IN MILLIMETERS DEBURR AND BREAK SHARP EDGES	A4		TITLE:	Kardangelenk A
DRAWN Jonas Gloss		Material	DWG NO.	H-cracker
CHK'D Michael Schmid		stainless steel		
APPV'D Peter Varga				
MFG Workshop IAP TU Wien		WEIGHT:	SCALE:1:2	SHEET 3 OF 5

SOLIDWORKS Educational Product. For Instructional Use Only.

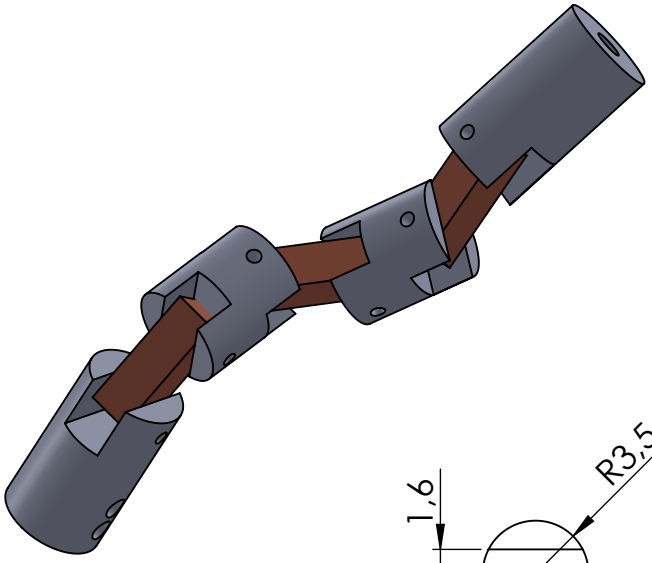

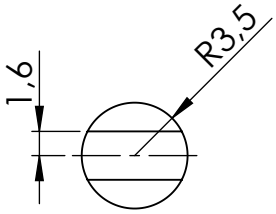

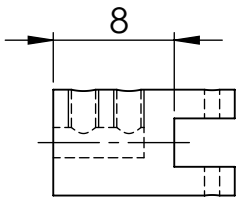

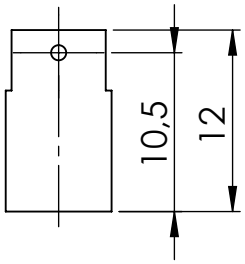

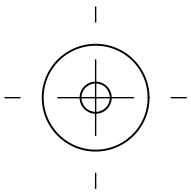

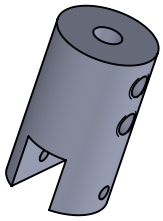

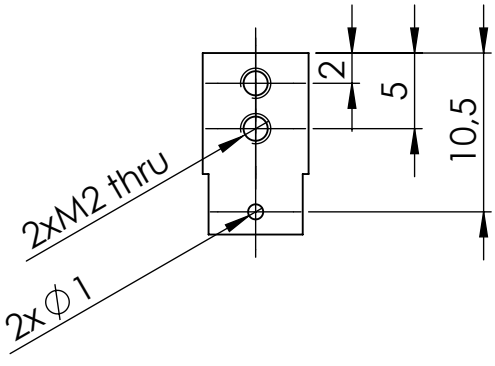

UNLESS OTHERWISE SPECIFIED: DIMENSIONS ARE IN MILLIMETERS DEBURR AND BREAK SHARP EDGES	A4		TITLE:	Kardangelenk B
DRAWN Jonas Gloss CHK'D Michael Schmid APPV'D Peter Varga MFG Workshop IAP TU Wien		Material: stainless steel WEIGHT:	DWG NO.	H-cracker
			SCALE:1:2	SHEET 4 OF 5

SOLIDWORKS Educational Product. For Instructional Use Only.

copper

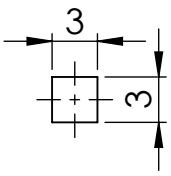

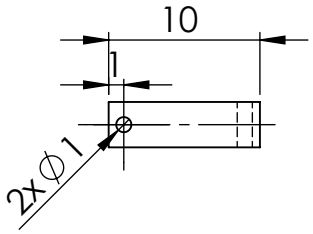

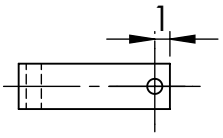

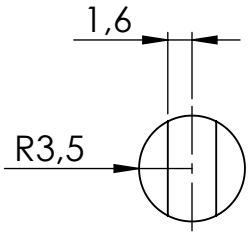

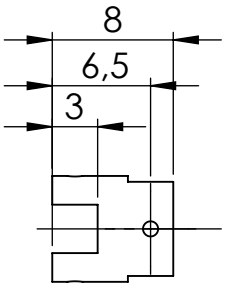

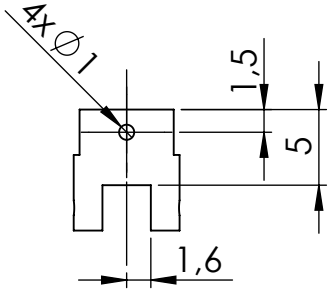

copper

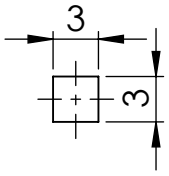

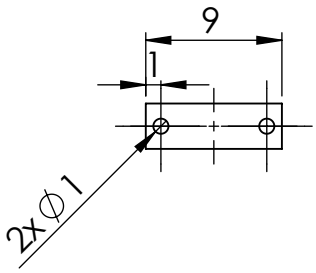

UNLESS OTHERWISE SPECIFIED: DIMENSIONS ARE IN MILLIMETERS DEBURR AND BREAK SHARP EDGES	A4	TITLE:	Kardangelenk C
DRAWN Jonas Gloss	Material	DWG NO.	H-cracker
CHK'D Michael Schmid	Stainless steel Cu		
APPV'D Peter Varga			
MFG Workshop IAP TU Wien	WEIGHT:	SCALE:1:2	SHEET 5 OF 5

SOLIDWORKS Educational Product. For Instructional Use Only.

Appendix C

Si heating stage

The Si heating stage was built to perform direct current (DC) heating of the Si samples attached to the Si sample plate for DC heating. The heating stage consists of an electrical feedthrough with four Cu rods (7 mm diameter, originally a TSP feedthrough) onto which a stainless steel head is connected. The head carries a molybdenum sample holder for the DC-heating sample plates. One Cu rod (feedthrough) carries the DC into the UHV. There, a tantalum wire connects the Cu rod to a Mo spring, which facilitates the contact to the sample plate for DC heating, shown in Figure C.1(a,b). The Ta wire and the Mo spring are separated from the stainless steel head by ceramics. The remaining three Cu rods are the support of the stainless steel head and therefore provide the second contact for the DC heating.

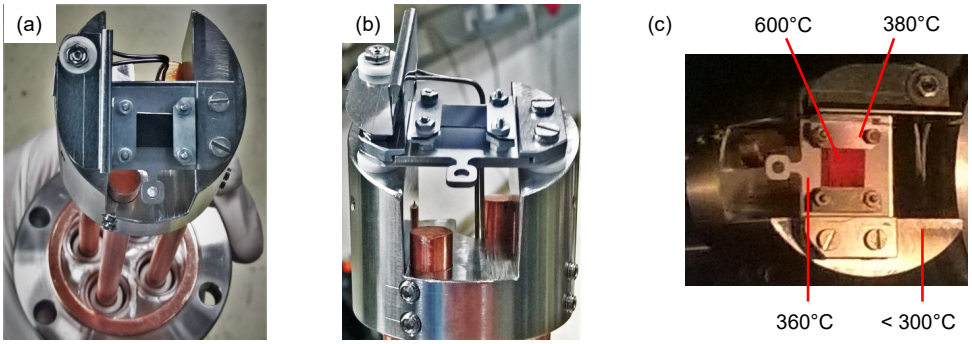

Figure C.1 | The Si heating stage. (a) top-view of the heating stage with a sample plate for DC heating and a Si sample. (b) side-view shows the contact of the Mo spring with the sample plate (c) temperature measurement after an overnight heating of the Si sample to 600°C.

ITEM NO.	PART NUMBER	
1	Si heating stage CF40 power feedthrough	
2	large support round v3	
3	sample plate Si	
4	ceramic Cu connector insulation	
6	Mo spring	
7	Mo sheet metal holder	
8	Mo sheet metal holder cpiece	
9	sample plate holder v3	

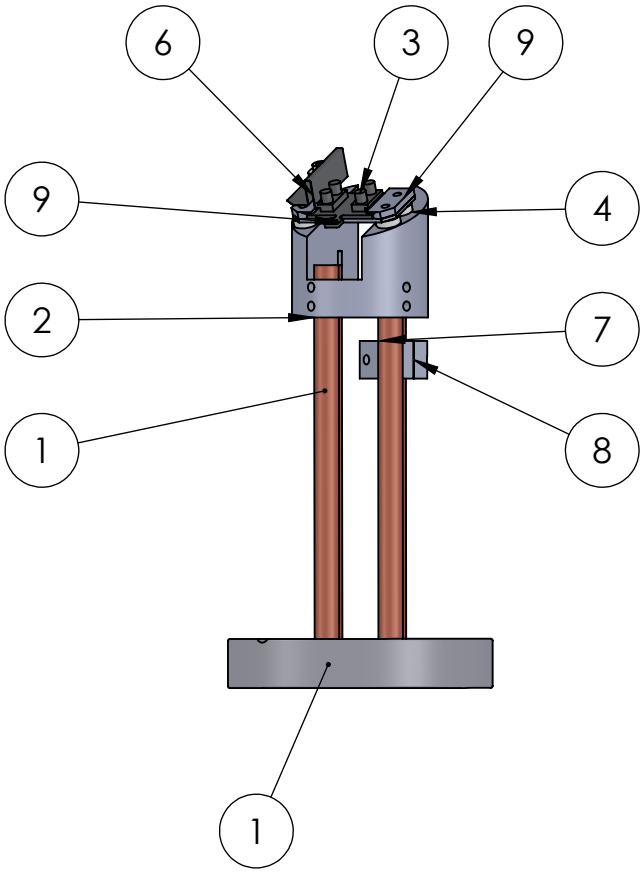

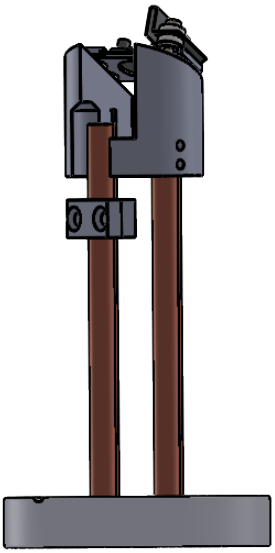

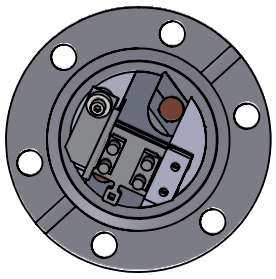

UNLESS OTHERWISE SPECIFIED:
DIMENSIONS ARE IN MILLIMETERS

DEBURR AND BREAK SHARP EDGES

A4

TITLE: overview

DRAWN	Jonas Gloss	Material: stainless steel, copper, molybdenum	DWG NO. Si_heating_stage
CHK'D	Michael Schmid		
APPV'D	Peter Varga		
MFG	Workshop IAP TU Wien	WEIGHT:	SCALE:1:1 SHEET 1 OF 5

SOLIDWORKS Educational Product. For Instructional Use Only.

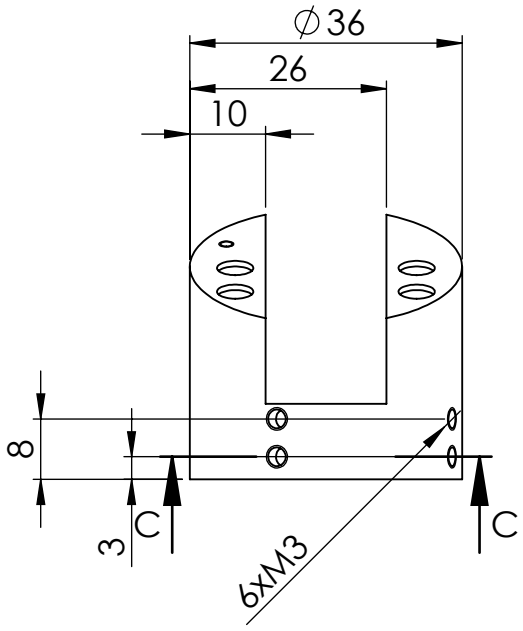

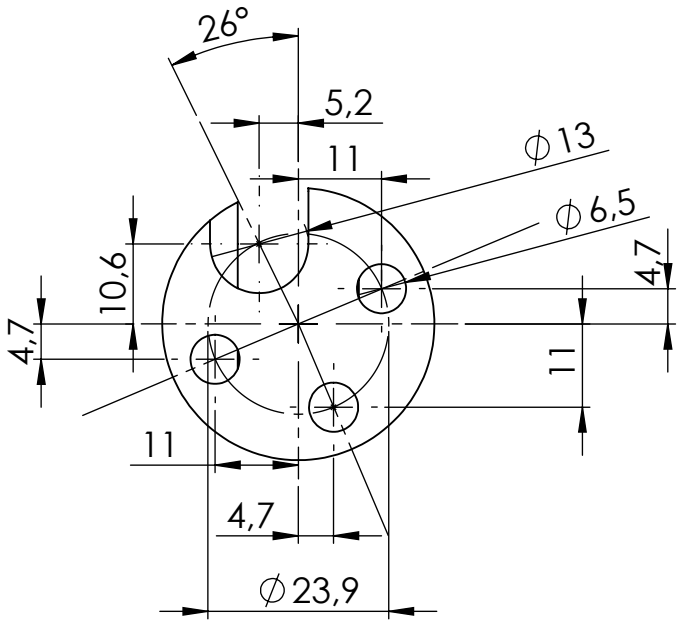

view rotated by 23 degrees

5xM2 6xM3 6xM3 ↧5.2
add a venting hole

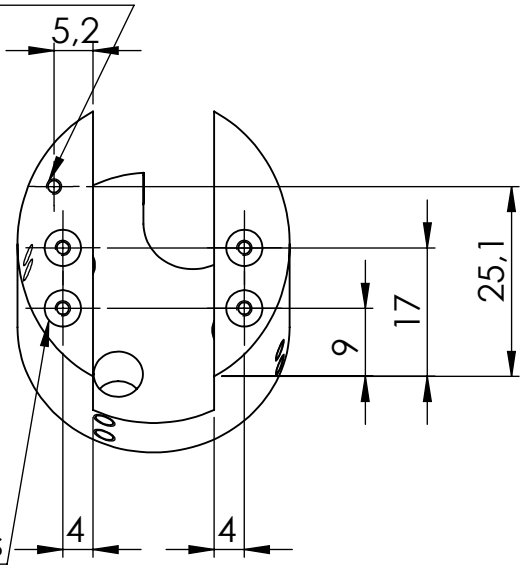

4x4.8 mm
↧1 mm
hole for ceramics

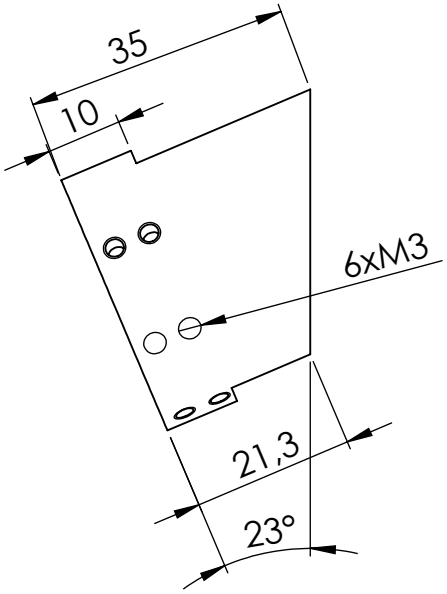

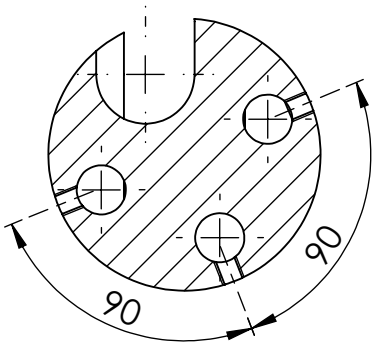

SECTION C-C
view rotated by -23 degrees

UNLESS OTHERWISE SPECIFIED: DIMENSIONS ARE IN MILLIMETERS DEBURR AND BREAK SHARP EDGES	A4	TITLE:	adaptor - base
DRAWN Jonas Gloss CHK'D Michael Schmid APPV'D Peter Varga MFG Workshop IAP TU Wien	Material: stainless steel WEIGHT:	DWG NO.: Si_heating_stage SCALE:2:1	SHEET 2 OF 5

SOLIDWORKS Educational Product. For Instructional Use Only.

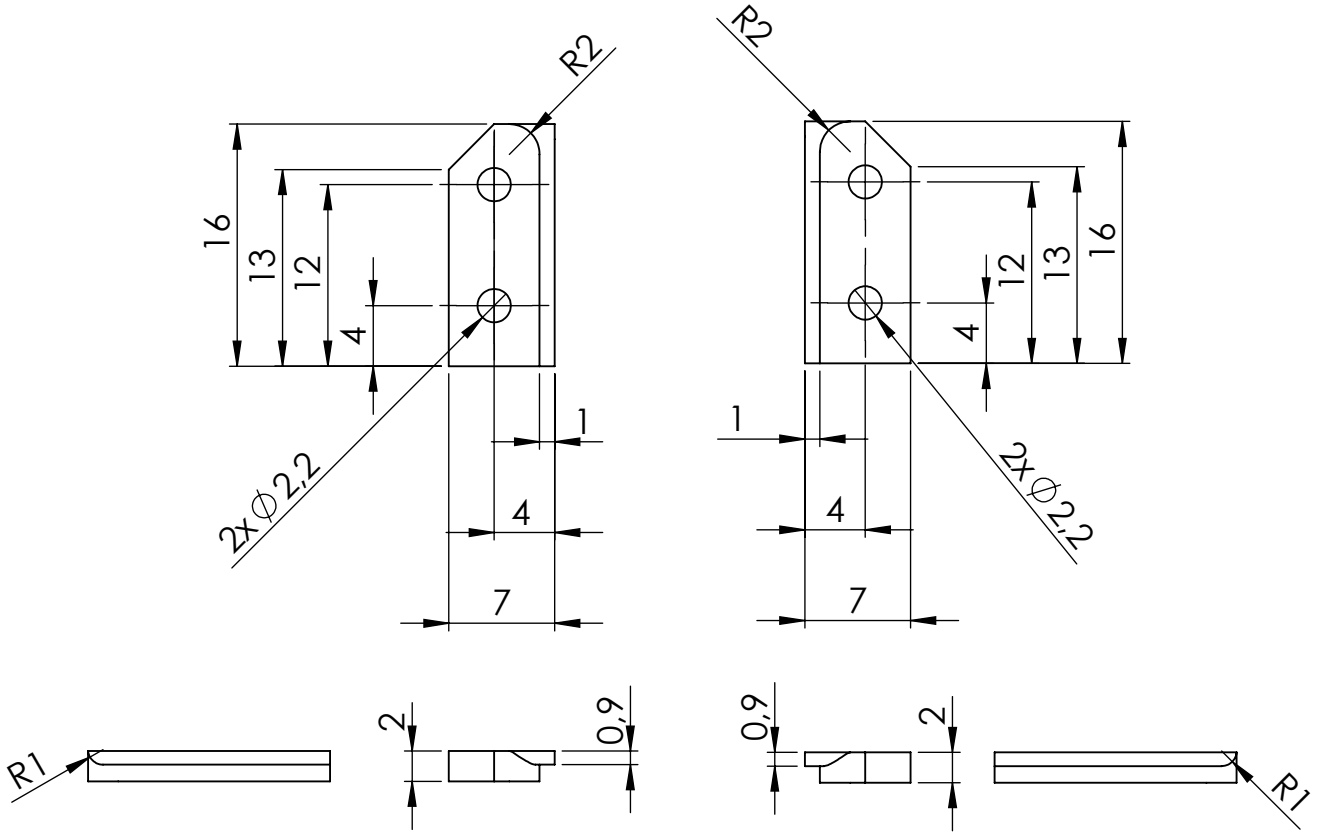

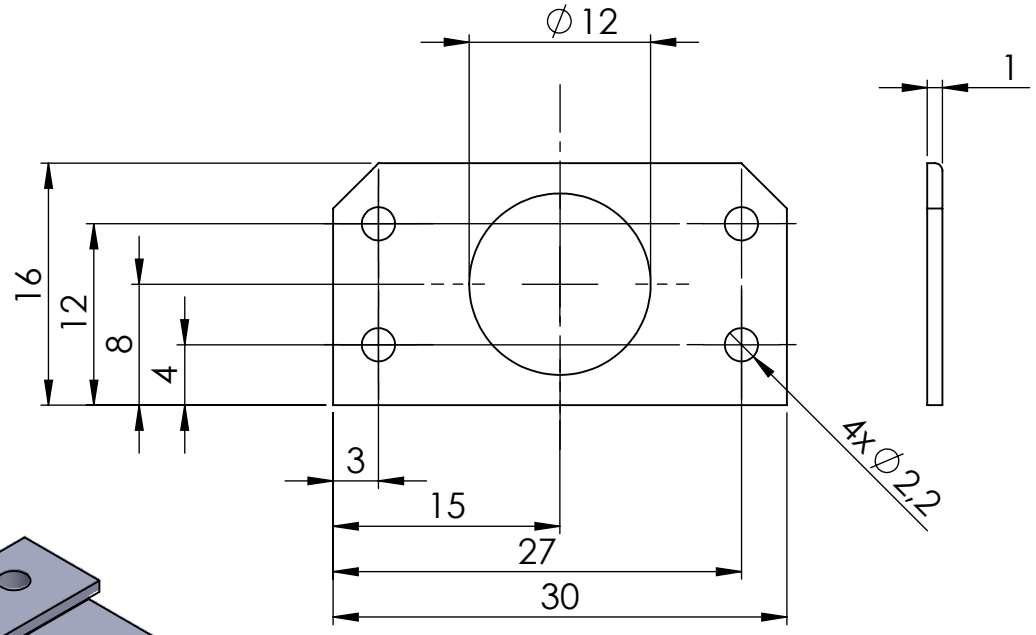

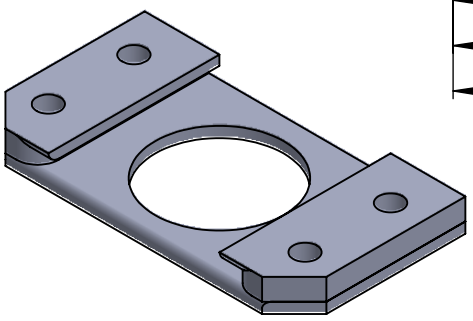

UNLESS OTHERWISE SPECIFIED: DIMENSIONS ARE IN MILLIMETERS DEBURR AND BREAK SHARP EDGES	A4		TITLE:	Sample Holder
DRAWN Jonas Gloss		Material	DWG NO.	Si_heating_stage
CHK'D Michael Schmid		Molybdenum		
APPV'D Peter Varga				
MFG Workshop IAP TU Wien		WEIGHT:	SCALE:2:1	SHEET 3 OF 5

SOLIDWORKS Educational Product. For Instructional Use Only.

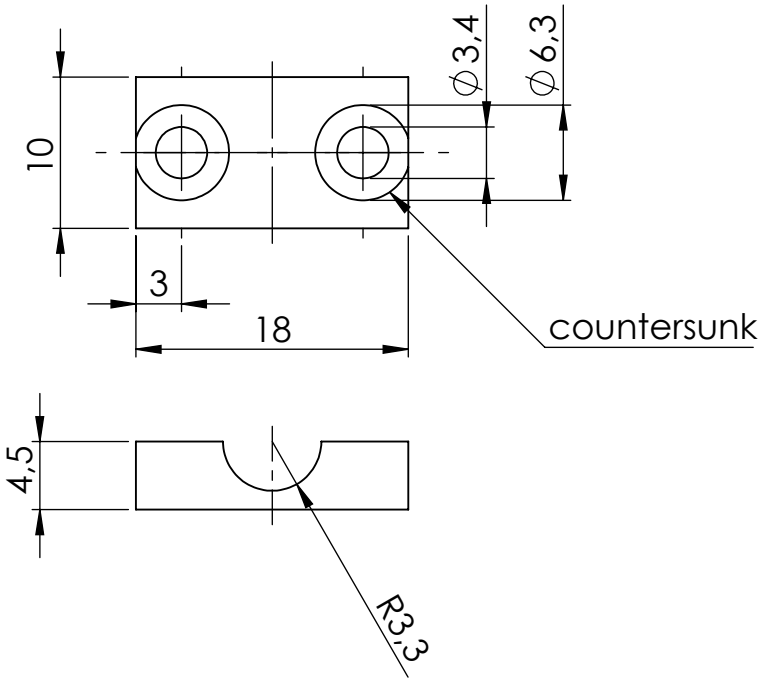

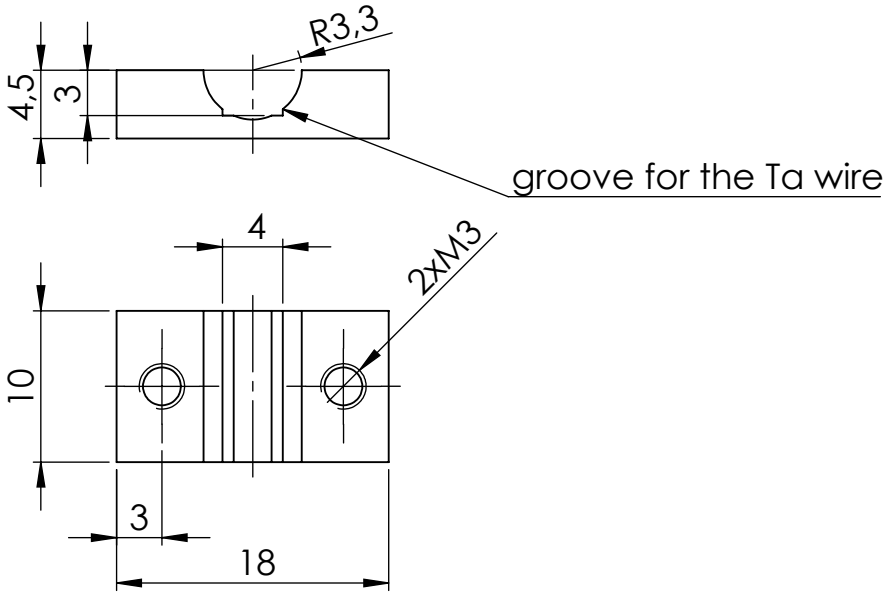

UNLESS OTHERWISE SPECIFIED: DIMENSIONS ARE IN MILLIMETERS DEBURR AND BREAK SHARP EDGES	A4	TITLE:	Ta wire holder
DRAWN Jonas Gloss CHK'D Michael Schmid APPV'D Peter Varga MFG Workshop IAP TU Wien	Material: stainless steel WEIGHT:	DWG NO.	Si_heating_stage
		SCALE:5:1	SHEET 4 OF 5

SOLIDWORKS Educational Product. For Instructional Use Only.

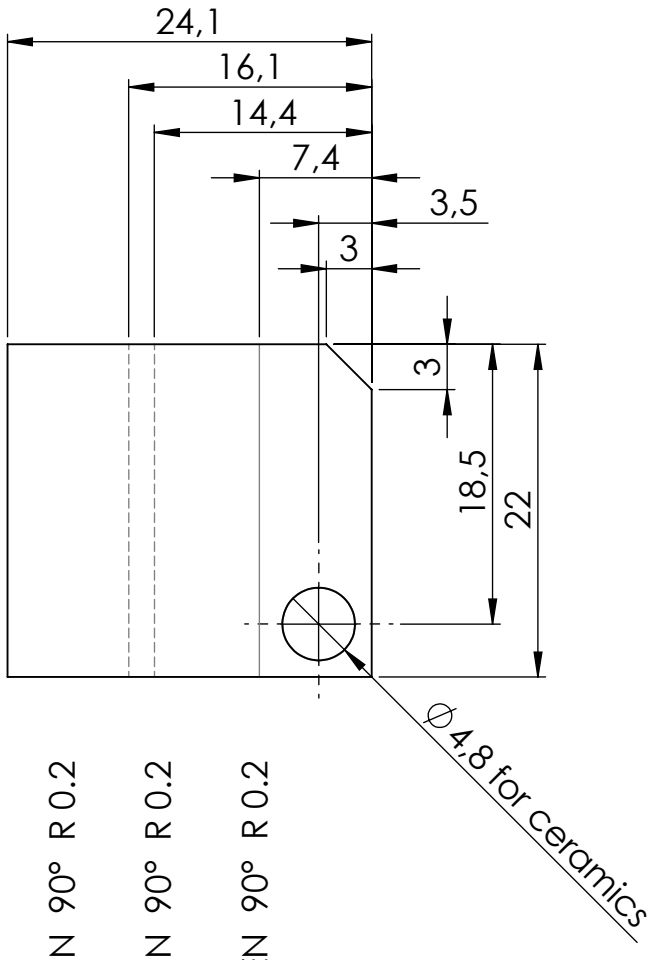

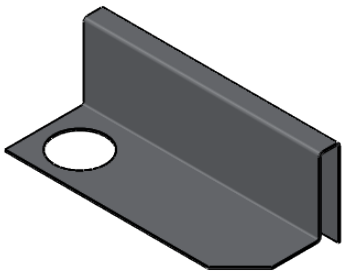

UNLESS OTHERWISE SPECIFIED: DIMENSIONS ARE IN MILLIMETERS DEBURR AND BREAK SHARP EDGES	A4		TITLE:	Mo spring
DRAWN Jonas Gloss		Material	DWG NO.	Si_heating_stage
CHK'D Michael Schmid		Molybdenum		
APPV'D Peter Varga				
MFG Workshop IAP TU Wien		WEIGHT:	SCALE:2:1	SHEET 5 OF 5

SOLIDWORKS Educational Product. For Instructional Use Only.

Appendix D

Si sample plate for direct current heating

The target holders for the direct current heating of Si(100) were made from molybdenum and their design was similar to that of commercially available (Omicron) sample plates. The contact to the sample is on one side from the body of the Si heating stage and on the other from a molybdenum spring shown in Figure C.1(a,b).

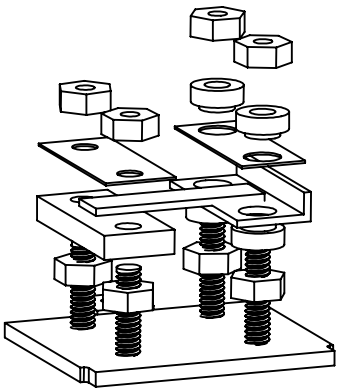

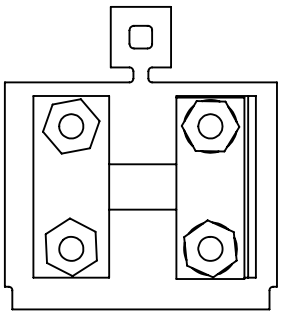

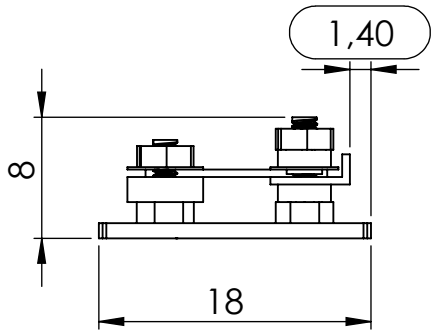

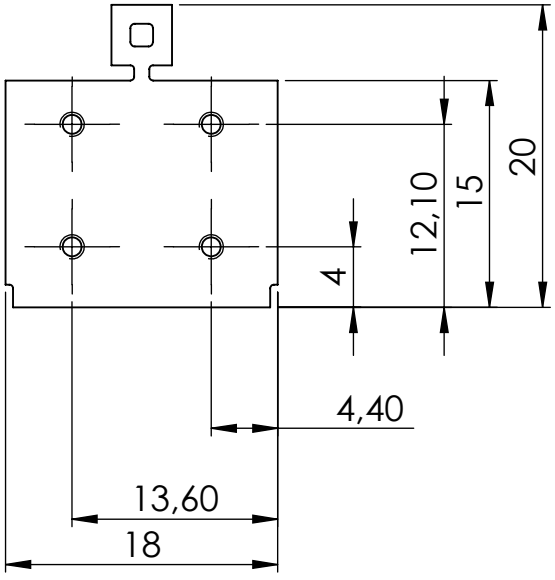

UNLESS OTHERWISE SPECIFIED: DIMENSIONS ARE IN MILLIMETERS DEBURR AND BREAK SHARP EDGES	A4		TITLE: Assembly
DRAWN Jonas Gloss		Material	DWG NO.
CHK'D Michael Schmid		Molybdenum Ceramics	Si DCSP PINUP
APPV'D Peter Varga			
MFG Workshop IAP TU Wien		WEIGHT:	SCALE:5:1 SHEET 1 OF 2

SOLIDWORKS Educational Product. For Instructional Use Only.

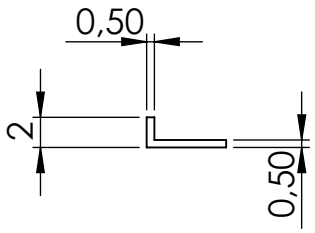

4 pcs

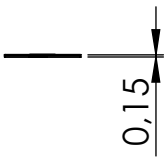

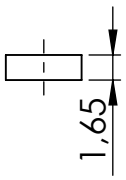

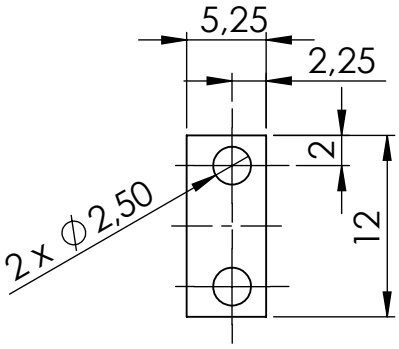

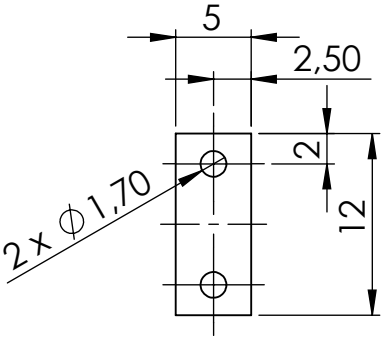

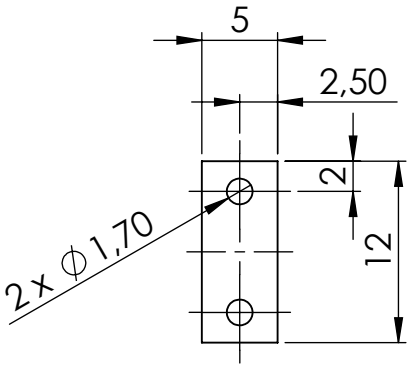

8 pcs M 1.6 nut

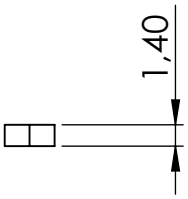

2 pcs M 1.6 x 8

4 pcs ceramics

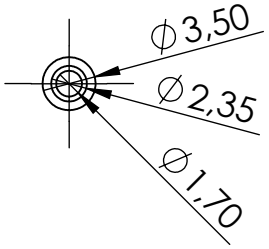

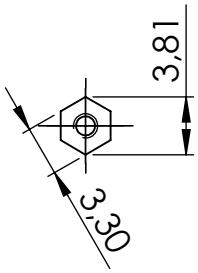

2 pcs M 1.6 x 6.5

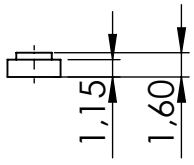

UNLESS OTHERWISE SPECIFIED: DIMENSIONS ARE IN MILLIMETERS DEBURR AND BREAK SHARP EDGES	A4	TITLE:	Parts
DRAWN Jonas Gloss CHK'D Michael Schmid APPV'D Peter Varga MFG Workshop IAP TU Wien	Material Molybdenum Ceramics WEIGHT:	DWG NO. Si DCSP PINUP SCALE:2:1	SHEET 2 OF 2

SOLIDWORKS Educational Product. For Instructional Use Only.

List of Figures

1.1 Fe growth regimes on Cu(100) exhibit three main structural and magnetic properties. 6

1.2 Scanning tunneling microscopy of an epitaxial 7-ML (1.3 nm) Fe/Cu(100) film. 6

1.3 (a) Curie temperature and magnetic moment as a function of the Ni concentration in an Fe-Ni alloy. (b) Experimentally determined phase diagram showing the dependence of the structural and magnetic properties of a Fe-Ni alloy on the residual gas pressure and the Ni concentration. 9

1.4 Ion-beam-induced transformation of the metastable fcc films. 10

2.1 Schematic view of energy levels inside an atom, the creation of a core hole by an incoming electron and of the Auger electron's emission process. 14

2.2 Ewald sphere construction. 16

2.3 Schematic view of the angle of rotation θ and the ellipticity ϵ, which define the complex number Φ of the Kerr effect. 18

2.4 The main growth modes during MBE. 20

2.5 Schematic view of the PLD setup with *in-situ* RHEED analysis and the connected UHV chambers. 22

2.6 Schematic description of RHEED, adapted from [55]. 23

3.1 Scheme of the PINUP chamber, which consists of two UHV vessels. . 28

3.2 A 3D view of the home-built H-cracker. 30

3.3 (a) The temperature of the tungsten capillary for different emissions at the middle (orange) and end (black) of the capillary. (b)The dependence of the amount of atomic H reaching the QMS on emission current of the filament, measured by percentual increase in the signal of atomic H on the QMS. 31
3.4 The dependence of the coverage of Si(100) by atomic H on the H_2 dose. 34
3.5 Schematic view of the RT-STM setup, which consist of two UHV vessels. Adapted from [66]. 36
3.6 Schematic view of the SPECS setup. 37

4.1 AES before and after $Fe_{78}Ni_{22}$ deposition on Cu(100)#13. 42
4.2 Analysis of as-deposited and irradiated $Fe_{78}Ni_{22}$/Cu(100). 43
4.3 Vapour pressure of Fe and Ni. 44
4.4 MOKE and SEM analysis of 8 nm $Fe_{78}Ni_{22}$/Cu(100)#10 upon irradiation by 30 keV Ga^+ ions. 46
4.5 Easy-axis direction change of completely transformed 8 nm $Fe_{78}Ni_{22}$/Cu(100) by FIB. 47
4.6 SRIM calculations of ion penetration depth (number of ions) and energy deposition into 8 nm $Fe_{78}Ni_{22}$/Cu. 49
4.7 SRIM calculations of the number and type of atoms in the molten volume (y-axis on the left) and the radius of the molten volume (y-axis on the right) in 8 nm $Fe_{78}Ni_{22}$/Cu. 50

5.1 LEED of Si(100) at 120 eV treated chemically and in UHV. 59
5.2 AES analysis of the steps in the preparation of the H-Si(100). 60
5.3 Analysis of LEED of Si after flashing 60
5.4 LEED of 130 nm Cu/Si(100). 62
5.5 Overview AES after the consecutive deposition of Cu/Si(100)#17. . . . 63
5.6 Change of the AES signal of a low energy Si peak during post-annealing of a 130 nm Cu/Si#22. 64

5.7 LEED at 120 eV of a H-Si(100) and an 8 nm $Fe_{78}Ni_{22}$/130 nm Cu/Si(100). 66
5.8 Summary of the LEED images in Figures 5.1, 5.4, and 5.7. 67
5.9 Longitudinal UHV SMOKE *in-situ* measurements of an 8 nm $Fe_{78}Ni_{22}$ film/ 130 nm Cu/ Si(100)#17. 68
5.10 SEM and Kerr microscope analysis of $3 \times 3\,\mu m^2$ squares in a 8-nm $Fe_{78}Ni_{22}$/130 nm Cu/Si(100)#20 films irradiated by a 30 keV Ga^+ FIB for different ion doses. 69

6.1 AES of C#3 treated by ion beam irradiation and by atomic hydrogen. 77
6.2 LEED of C(100)#4 and deposition of $Fe_{78}Ni_{22}$/C(100)#4. 79
6.3 Structural analysis of $Fe_{78}Ni_{22}$/C(100). 80
6.4 AES analysis of steps in the deposition of the $Fe_{78}Ni_{22}$/Cu(100). 81
6.5 Dependence of the magnetic saturation (M_S) and coercivity (H_C) on the 4 keV Ar^+ ion dose for 8 nm $Fe_{78}Ni_{22}$/C(100)#9 measured in-situ by longitudinal SMOKE. 85
6.6 µMOKE measurement of 3 μm circles produced by 30 keV Ga^+ FIB in $Fe_{78}Ni_{22}$/C(100)#4 86

7.1 Structural analysis of an etched and annealed $SrTiO_3$(100) #1. 93
7.2 UHV-preparation of $SrTiO_3$(100) by 2 sputter-anneal cycles. (a) LEED at 100 eV shows a (6×2) reconstruction. 94
7.3 RHEED and AFM analysis of 40 nm Cu deposited on $SrTiO_3$(100) #1 at 100 °C. 96
7.4 RHEED, LEED and AFM analysis of 40 nm Cu/$SrTiO_3$(100) #3 deposited at 300 °C. 97
7.5 Analysis of 40 nm Cu on $SrTiO_3$(100) #6 deposited in the three-step approach. 97
7.6 XPS on $SrTiO_3$(100) #1 of the first experiment, in which we deposited 40 nm Cu at 100 °C and post-annealed at 300 °C (Figure 7.3). 99
7.7 Cu on sputter-anneal prepared $SrTiO_3$(100) #13. 100

C.1 The Si heating stage. 149

List of Tables

4.1 Comparison of ion dose, type and energy used for the complete transformation of the metastable films on Cu(100). 50

7.1 Comparison of the PLD parameters used in the depositions by Francis [35] and presented in this chapter. 95

8.1 Broadband FMR and BLS measurements of the transformed metastable films and permalloy. 105

A.1 Overview of Cu(100) samples used for the experiments in Chapter 4. Refer to Section 4.2 for further information on preparation. 121

A.2 Overview of $SrTiO_3$(100) samples used for the experiments in Chapter 7. PA corresponds to post anneal. 122

A.3 Overview of C(100) samples used for the experiments in Chapter 5. . 123

A.4 Overview of Si(100) samples used for the experiments in Chapter 5. Three relevant experiments on the HF-etched Si are included. 124

A.5 Overview of Si(100) samples used for the experiments in Chapter 5 (continued). 125

Acknowledgment

I would like to thank Peter Varga and Michal Urbánek for entrusting me the preparation of the metastable films and leading this project. It is sad that I am Peter's last Ph.D. student; he helped me to understand physics and life a bit more. Thanks to Michael Schmid for his advices, patience and his deep understanding of physics; I thank him also for taking the project over after Peter has passed away. The research in this thesis was carried out in the group of Ulrike Diebold, whom I thank for sharing her experience as an excellent leader and researcher. I would like to express my gratitude to Austrian Science Fund (FWF) for financial support.

My thanks belongs to Michele Riva for support in the investigations on the $SrTiO_3(100)$ in Chapter 7 and to the colleagues from Ulrike Diebold's group who contributed to having a wonderful workplace at the Institute of Applied Physics. I thank the colleagues from Central European Institute of Technology (CEITEC); especially to Lukáš Flajšman, Viola Križáková and Jakub Holobrádek. I would also like to thank to my teachers and professors, who allowed my passion for physics to grow. From these, I would like to point out Marek Šefčík. This work came to a successful end thanks to the continuous support from my family, Community Emmanuel and my dear Kaci.

> [3] I look at the heavens you made with your hands. I see the moon and the stars you created. [4] And I wonder, "Why are people so important to you? Why do you even think about them? Why do you care so much about humans? Why do you even notice them?" [5] But you made them almost like gods and crowned them with glory and honor. [6] You put them in charge of everything you made. You put everything under their control.
>
> [9] Lord our Lord, your name is the most wonderful name in all the earth!
>
> Psalm **8**, 3-6, 9

Curriculim Vitae

Personal information

Name:	Jonas Gloss
Address:	Schenkenstraße 2, 1010 Wien, Austria
Nationality:	Slovak
Contact:	+43 670 206 2265
	jonas.gloss@gmail.com

Education

June 2015 – April 2019	Doctoral programme in applied physics Austria, TU Wien Supervisors: Prof. Peter Varga (+27.10.2018) and prof. Michael Schmid *Metastable Iron-Nickel Thin Films*
Sept. 2009 – June 2014	Master of Physical Engineering and Nanotechnology Czechia, Brno University of Technology Diploma thesis: *Magnetic Transformation of Metastable fcc Fe/Cu(100) Films by Focused Ion Beam* Graduated with distinction, academic scholarship (2009-14)
Sept. 2007 – June 2009	International Baccalaureate (IB) Diploma United Kingdom, Whitgift School Private school, full scholarship
Sept. 2005 – June 2007	Secondary school, Slovakia, Gymnasium of John Bosco

Internships

Aug 2017 – Dec 2017 — Knowledge transfer
Czechia, Central European Institute of Technology (CEITEC)

- Responsibility for sharing the research results and solutions with our scientific collaborators
- Successful adaptation of experiments performed at the TU Wien in the course of the dissertation

2012 - 2013 — Internship and Erasmus at the Institute of Applied Physics,
TU Wien,

- Technical support of on-going projects
- Start of the research for the diploma thesis
- Scholarship for young researchers

Employment

2015-18 TU Wien,
- full-time work as a researcher in an FWF project
- independent problem-solving in both planning and researching
- supervision of several project students

Jan 2013 – June 2014 CEITEC, part-time research assistant
- support throughout the work on the diploma thesis

Publications

2019 Urbanek, M., et al*., Focused ion beam direct writing of magnetic patterns with controlled structural and magnetic properties, APL Mat* ***6***, 060701

2018 Gloss, J., et al., *The growth of metastable fcc $Fe_{78}Ni_{22}$ thin films on H-Si(100) substrates suitable for focused ion beam direct magnetic patterning*, ASS, **469** 747-752

2013 Gloss J., et al., *Ion-beam-induced magnetic and structural phase transformation of Ni-stabilized face-centered-cubic Fe films on Cu(100),* APL **103**, 262405

(Selected) Presentations at conferences

2018 Annual meeting of the German Physical Society
Talk: *Magnetic nanostructures in metastable fcc Fe thin films on Cu(100) and Si(100)*

2017 Annual meeting of the German Physical Society
Talk: *Ion-beam-induced magnetic and structural phase transformation of fcc Fe thin films on different substrates*

2016 European Conference on Surface Science
Talk: *Ferromagnetic nanostructures produced on metastable fcc Fe film on H-Si(100) and diamond by focused ion beam*

2015 65th annual meeting of the Austrian Physical Society (ÖPG)
Poster: *Ion-beam-induced magnetic and structural phase transformation of fcc Fe thin films*